A SEARCH FOR QUARK COMPOSITENESS WITH THE CDF DETECTOR AT THE FERMILAB COLLIDER

A Dissertation

by

TIMOTHY LEE HESSING

Submitted to the Office of Graduate Studies of
Texas A&M University
in partial fulfillment of the requirements for the degree of

DOCTOR OF PHILOSOPHY

December 1990

Major Subject: Physics

AAB2026

A SEARCH FOR QUARK COMPOSITENESS WITH THE CDF DETECTOR AT THE FERMILAB COLLIDER

A Dissertation

by

TIMOTHY LEE HESSING

Approved as to style and content by:

Robert C. Webb
(Chair of Committee)

John C. Hiebert
(Member)

Peter M. McIntyre
(Member)

Kevin C. Wolf
(Member)

Richard L. Arnowitt
(Head of Department)

December 1990

ABSTRACT

A Search for Quark Compositeness with the CDF

Detector at the Fermilab Collider. (December 1990)

Timothy Lee Hessing, A.B., Augustana College, Rock Island, Illinois

Chair of Advisory Committee: Dr. Robert C. Webb

The inclusive jet cross section in $p\bar{p}$ collisions at $\sqrt{s} = 1.8$ TeV has been measured using jet clustering cone sizes of 0.4, 0.7 and 1.0. The cone size, R, is defined to be, $R = \sqrt{\Delta\eta^2 + \Delta\phi^2}$, where $\eta = -\ln\tan\theta/2$, θ represents the polar angle and ϕ represents the azimuthal angle. A lower limit on the value of the composite scale parameter, Λ_c, was determined to be 1100 GeV at the 95% confidence level using the cone size 1.0. Comparisons to both leading order Quantum Chromo Dynamics (QCD) and next-to-leading order QCD calculations have been made and no significant deviations from QCD observed. The dependence of the inclusive jet cross section on cone size has also been compared to next-to-leading order QCD. The measured cross section was found to grow larger with increasing cone size, more quickly than next-to-leading order QCD predicts.

DEDICATION

This dissertation is dedicated to

my mother and father,

who have supported my brothers and me

in all our endeavors.

ACKNOWLEDGEMENTS

There are so many people I would like to thank including all those people listed in Appendix B, who help build and run CDF. In particular, I would like to thank Muzaffer Atac and Richard Kadel for hiring me when I was an undergraduate and introducing me to high energy physics and the CDF experiment. Also, I thank Rick St. Denis who showed me around and oriented me during my first summer as a graduate student working on CDF.

I thank Robert Webb for supporting me in my studies at Texas A&M and his patience in putting up with me. I also greatly appreciate the work of Ann David and Nick Diaczenko who built most of the forward hadron calorimeter before I became involved in the project. I also would like to thank Peter McIntyre, John Hiebert, and Kevin Wolf for agreeing to be on my committee, and thus taking on the task of reading this dissertation and giving me guidance in this regard.

I thank Teruki Kamon and more recently Themis Bowcock, for sharing with me their knowledge of high energy physics and giving me guidance in writing and working on this dissertation. I also thank Steve Behrends, John Huth, Rob Plunkett and Marjorie Shapiro for their immense help in increasing my understanding of high energy physics, and in particular, teaching me about jets and the CDF detector.

At a personal level, I thank my fellow graduate students on CDF and at Texas A&M, from the guys at CDF (Les, Brian, and the other guy) who went to observe the future site of the SSC with me in Texas, to my friend Phil Bowman who suffered the pains of graduate student life at Texas A&M along with me.

I also appreciate the patience and support of my aunt, Helen Lindsay, who helped support my undergraduate education. I thank Pat and Tracie Summerville who allowed me to stay with them in Collinsville on my many trips back and forth from College Station to Batavia, and still remained my friends after all the things I have broken at their house. I also thank Kevin Summerville and John Penchoff for their friendship, even though we didn't catch any big fish in Texas when they came to visit me.

Finally, I would like to thank Lynn Rinker for correcting most of my punctuation and spelling errors in this dissertation and teaching me that there is more to life than physics and football.

TABLE OF CONTENTS

Page

ABSTRACT iii

DEDICATION iv

ACKNOWLEDGEMENTS v

TABLE OF CONTENTS vii

LIST OF TABLES x

LIST OF FIGURES xiv

CHAPTER

I INTRODUCTION 1

A. Historical Review 1
B. Experimental Status 4
C. Theoretical Motivation 8

1. Quantum Chromodynamics 8
2. Compositeness 13

II THE CDF DETECTOR 16

A. Tracking 18

1. Vertex Time Projection Chamber 19
2. Central Tracking Chamber 20
3. Central Drift Tubes 21
4. Forward Tracking Chamber 22

B. Solenoid Magnet Coil 22
C. Calorimeters 23

1. Central Electromagnetic Calorimeter 23
2. Hadronic Central and Endwall Calorimeter 24
3. Plug Electromagnetic Calorimeter 25
4. Plug Hadronic Calorimeter 26
5. Forward Electromagnetic Calorimeter 26

CHAPTER Page

6. Forward Hadronic Calorimeter 26

D. Muon Detection 27

1. Central Muon Chambers 27
2. Forward Muon Chambers 28

E. Data Acquisition System 29

1. Front End Electronics 29
2. Data Acquisition 30
3. Beam-Beam Counters 31
4. Triggering 32

III MEASUREMENT OF JETS AT CDF 34

A. Jet Definition 34
B. Data Collection and Triggering 41
C. Event Reconstruction 42
D. Background Cuts 43
E. Acceptance Region 53
F. Measuring the Raw Cross Section 56

IV JET CORRECTIONS 68

A. Simulation 68
B. Jet E_t and Resolution 79

V SYSTEMATIC UNCERTAINTIES 101

A. E_t Scale Systematic Uncertainties 101

1. Calorimeter Response 102
2. Fragmentation Tuning 103
3. Underlying Event 104
4. 1990 Test Beam Results 105
5. Resulting Jet E_t Scale Uncertainty 106

B. Systematic Uncertainty on the Jet Resolution 117
C. Luminosity Uncertainty 118
D. Systematic Uncertainty on the Jet Cross Section 120

VI COMPARISONS WITH QCD AND A COMPOSITE MODEL 131

CHAPTER Page

A. Fitting Procedure 131
B. Comparisons to Leading Order 135

1. QCD 138
2. A Composite Model 142

C. Comparisons to Next-to-Leading Order 167

VII RESULTS AND CONCLUSIONS 175

REFERENCES 186

APPENDIX

A DIJET BALANCING 193

A. Dijet $\vec{k}_t$ 193
B. Jet Resolution 195

B THE CDF COLLABORATION 198

VITA 201

LIST OF TABLES

Table — Page

I. A list of the Standard Model quark and lepton families and their properties. 7

II. Elementary cross sections for leading order α_s^2 QCD subprocesses, given in the form $(\hat{s}/\pi)d\hat{\sigma}/d\hat{t}$. 11

III. List of next-to-leading order α_s^3 QCD subprocesses. 12

IV. This is the event classification scheme for determining backgrounds in jet events. 50

V. Number of events per Class, found in the data sample used in this study. 54

VI. Results from event scanning. 54

VII. Efficiency thresholds for jet triggers as a function of cone size. . . . 61

VIII. Raw jet cross section and related quantities for a jet clustering cone size of 0.4, number of jets has been scaled accordingly. 62

IX. Raw jet cross section and related quantities for a jet clustering cone size of 0.7, number of jets has been scaled accordingly. 64

X. Raw jet cross section and related quantities for a jet clustering cone size of 1.0, number of jets has been scaled accordingly. 66

XI. Values of the tuned parameters in SETPRT. 74

XII. The values of the parameters obtained for the parameterization of the *Mean*, for each cone size. 84

XIII. The values of the parameters obtained for the parameterization of the *Sigma*, for each cone size. 84

XIV. The values of the parameters obtained for the parameterization of the *Slope*, for each cone size. 85

XV. Fits to parameterized curve used in unsmearing procedure. 90

Table — Page

XVI. Corrections to the raw jet cross section and related quantities for a jet clustering cone size of 0.4. 92

XVII. Corrections to the raw jet cross section and related quantities for a jet clustering cone size of 0.7. 94

XVIII. Corrections to the raw jet cross section and related quantities for a jet clustering cone size of 1.0. 96

XIX. Calorimeter response fractional systematic uncertainty on the corrected jet E_t scale. 109

XX. Fragmentation fractional systematic uncertainties on the corrected jet E_t scale. 111

XXI. Underlying event E_t density fractional systematic uncertainty on the corrected jet E_t scale. 113

XXII. Fractional uncertainty associated with the difference in the 1990 test beam results and previous test beam results. 115

XXIII. Total fractional systematic uncertainty on the corrected jet E_t scale for each cone size. 115

XXIV. Percent systematic uncertainty on the inclusive jet cross section for a jet clustering cone size of 0.4. 125

XXV. Percent systematic uncertainty on the inclusive jet cross section for a jet clustering cone size of 0.7. 127

XXVI. Percent systematic uncertainty on the inclusive jet cross section for a jet clustering cone size of 1.0. 129

XXVII. List of the lower and upper limits defining the fitting region used for each cone size. 137

XXVIII. The χ^2 and number of bins found in the various regions examined in the fitting procedure for a cone size of 0.4 using the various structure functions. 139

XXIX. The χ^2 and number of bins found in the various regions examined in the fitting procedure for a cone size of 0.7 using the various structure functions. 140

Table | Page

XXX. The χ^2 and number of bins found in the various regions examined in the fitting procedure for a cone size of 1.0 using the various structure functions. 141

XXXI. Combined χ^2 (fit region combined with upper region), number of bins (including the empty bin) and the confidence level obtained using the various structure functions for a cone size of 0.4. 143

XXXII. Combined χ^2 (fit region combined with upper region), number of bins (including the empty bin) and the confidence level obtained using the various structure functions for a cone size of 0.7. 144

XXXIII. Combined χ^2 (fit region combined with upper region), number of bins (including the empty bin) and the confidence level obtained using the various structure functions for a cone size of 1.0. 145

XXXIV. Confidence Levels (%) in the fit region and upper region for a cone size of 0.4 using the various structure functions. 153

XXXV. Confidence Levels (%) in the fit region and upper region for a cone size of 0.7 using the various structure functions. 154

XXXVI. Confidence Levels (%) in the fit region and upper region for a cone size of 1.0 using the various structure functions. 155

XXXVII. Number of jets found in the E_t range from 266.0 to 429.6 GeV, number of jets predicted by theory and the significance of this excess for a cone size of 0.4. 163

XXXVIII. Number of jets found in the E_t range from 271.9 to 440.0 GeV, number of jets predicted by theory and the significance of this excess for a cone size of 0.7. 164

XXXIX. Number of jets found in the E_t range from 273.2 to 445.6 GeV, number of jets predicted by theory and the significance of this excess for a cone size of 1.0. 165

XL. Number of jets over the number of events per bin found in the last six bins of the data. 166

XLI. Results of the comparison of next-to-leading order QCD calculations (using the structure function MRS B) of the inclusive jet cross section to the measured cross section. 170

Table | Page

XLII. Corrected jet cross section for a jet clustering cone size of 0.4. . . . 177

XLIII. Corrected jet cross section for a jet clustering cone size of 0.7. . . . 179

XLIV. Corrected jet cross section for a jet clustering cone size of 1.0. . . . 181

LIST OF FIGURES

Figure — Page

1. An example of a two jet event, in the CDF detector, which illustrates a 2-2 body QCD process. . . . 10
2. An example of a three jet event, in the CDF detector, which illustrates a 2-3 body QCD process. . . . 13
3. Perspective view of the CDF detector showing the central detector and the forward/backward detectors. . . . 17
4. Cut-away view of one-half of the CDF detector showing the individual detector sub-systems making up the central and forward/backward detectors. . . . 18
5. An example of the η-ϕ segmentation in one quadrant of the CDF hadronic calorimeter. . . . 35
6. An illustration of a particle transversing a projective tower. . . . 36
7. Flow chart of the fixed cone algorithm used by CDF, starting after candidate tower, seed tower and precluster lists have been formed. . . . 39
8. Flow chart illustrating the reconstruction path used for the jet data. . . . 44
9. EMF of highest E_t central jet in each event. . . . 46
10. E_t weighted EMF for each event (EMF). . . . 47
11. Average P_t/E_t for all central jets in each event (CHF). . . . 48
12. Missing E_t significance for each event (MET). . . . 49
13. CHF versus EMF. . . . 51
14. CHF versus MET. . . . 52
15. MET versus EMF. . . . 53
16. Effective cross section for jet backgrounds; Class 5, 6 and 11. . . . 55
17. Fraction of jet backgrounds; Class 5, 6 and 11. . . . 56

Figure — Page

18. Expected cosmic ray event rates. . . . 57
19. Event vertex distribution. . . . 58
20. Comparisons of the raw trigger cross sections for jets with a cone size of 0.7. . . . 60
21. The distribution of $Z(T)$ in jets with a cone size of 0.7 as defined in Equation 19. . . . 75
22. The jet track multiplicity in jets with a cone size of 0.7. . . . 76
23. The underlying event track multiplicity in jets with a cone size of 0.7. . . . 77
24. The distribution of $P_\perp$ in jets with a cone size of 0.7. . . . 78
25. Fraction of energy loss in jets with a cone size of 0.7, due to hadronic non-linearity. . . . 80
26. The simulated response of the detector at several E_t's for jets. . . . 83
27. An illustration of the unsmearing procedure. . . . 86
28. Unsmearing plots for cross sections of the various cone sizes. . . . 89
29. Unsmeared and corrected cross section for jets with a cone size of 0.7, the lines indicate direction of corrections. . . . 91
30. The 1987 cross section for jets with a cone size of 0.6 compared to 1988–1989 cross section for jets with a cone size of 0.7. . . . 98
31. The 1987 E_t corrections compared to the 1988–1989 E_t corrections. . . . 99
32. Comparison of the rms resolution for data, simulation and the parameterized response for jets with a cone size of 0.7. . . . 100
33. Loss plots as a function of measured jet E_t for the data. . . . 108
34. Loss plots from the simulation as a function of measured jet E_t. . . . 110
35. The fractional uncertainty of the corrected jet E_t scale due to the difference in the 1990 test beam with previous test beam results. . . . 114

Figure Page

36. The breakdown of the various components of the total fractional systematic uncertainty on the corrected jet E_t scale for each cone size. 116

37. Difference in the rms jet resolution between data and simulation. 119

38. The fraction of uncertainty on the jet cross section, from the uncertainty on the E_t scale. 122

39. The fraction of uncertainty on the jet cross section, from the uncertainty on the jet resolution. 123

40. The total fraction of systematic uncertainty on the jet cross section. . . . 124

41. Leading order QCD calculation of the inclusive jet cross section compared to a Composite Model calculation using the structure function DFLM set 1, with $\Lambda_c = 950$ GeV and $Q^2 = 0.5\ E_t^2$. 136

42. Measured cross section compared to leading order QCD using the structure function MRS set B and a cone size of 0.4. 146

43. Measured cross section compared to leading order QCD using the structure function MRS set 3 and a cone size of 0.4. 147

44. Measured cross section compared to leading order QCD using the structure function MRS set B and a cone size of 0.7. 148

45. Measured cross section compared to leading order QCD using the structure function MRS set 3 and a cone size of 0.7. 149

46. Measured cross section compared to leading order QCD using the structure function MRS set B and a cone size of 1.0. 150

47. Measured cross section compared to leading order QCD using the structure function MRS set 3 and a cone size of 1.0. 151

48. Composite calculation ($\Lambda_c = 980$ GeV) of the inclusive jet cross section compare to the measure cross section using the structure function MRS set 2 and a cone size of 0.4. 156

49. Composite calculation ($\Lambda_c = 1010$ GeV) of the inclusive jet cross section compare to the measure cross section using the structure function MRS set 2 and a cone size of 0.4. 157

Figure Page

50. Composite calculation ($\Lambda_c = 1050$ GeV) of the inclusive jet cross section compare to the measure cross section using the structure function EHLQ set 2 and a cone size of 0.7. 158

51. Composite calculation ($\Lambda_c = 1090$ GeV) of the inclusive jet cross section compare to the measure cross section using the structure function EHLQ set 2 and a cone size of 0.7. 159

52. Composite calculation ($\Lambda_c = 1100$ GeV) of the inclusive jet cross section compare to the measure cross section using the structure function EHLQ set 2 and a cone size of 1.0. 160

53. Composite calculation ($\Lambda_c = 1130$ GeV) of the inclusive jet cross section compare to the measure cross section using the structure function DFLM set 3 and a cone size of 1.0. 161

54. Comparison of next-to-leading order QCD and leading order QCD, using structure function MRS set B. 169

55. Next-to-leading order QCD calculation of the inclusive jet cross section compare to the measure cross section using the structure function MRS B for a cone size of 0.4. 171

56. Next-to-leading order QCD calculation of the inclusive jet cross section compare to the measure cross section using the structure function MRS B for a cone size of 0.7. 172

57. Next-to-leading order QCD calculation of the inclusive jet cross section compare to the measure cross section using the structure function MRS B for a cone size of 1.0. 173

58. Next-to-leading order QCD calculation of the inclusive jet cross section compare to the measure cross section using the structure function MRS B for $E_t = 100$ GeV. 174

59. Inclusive jet cross section for a cone size of 0.4, normalization uncertainty is the E_t independent systematic uncertainty and the error bars represent the statistical uncertainty added in quadrature with the E_t dependent part of the systematic uncertainty. 183

Figure Page

60. Inclusive jet cross section for a cone size of 0.7, normalization uncertainty is the E_t independent systematic uncertainty and the error bars represent the statistical uncertainty added in quadrature with the E_t dependent part of the systematic uncertainty. 184

61. Inclusive jet cross section for a cone size of 1.0, normalization uncertainty is the E_t independent systematic uncertainty and the error bars represent the statistical uncertainty added in quadrature with the E_t dependent part of the systematic uncertainty. 185

62. Illustration of dijet $\vec{k}_t$ coordinate system. 194

63. Dijet $\vec{k}_t$ distributions. 197

CHAPTER I

INTRODUCTION

The search for substructure in matter has led to the simplification of the physical theories describing the world. At the same time it has raised more questions concerning the nature of matter. Quark substructure, or quark compositeness, is one of the next steps in this search. In this chapter, the history of this search is discussed and the current experimental state reviewed. The measurement of the inclusive jet cross section is one method of searching for quark compositeness. The theoretical justification for this measurement and its interpretation will therefore be described.

Following the theoretical motivation, the apparatus used for the measurement of jets is described in Chapter II. The measurement of the jets, the physical properties of the jets, and the determination of the inclusive jet cross section are then described in Chapter III. Chapter IV describes the calculation and use of corrections in order to compare the measured jet cross section with theory. The systematic uncertainties for this measurement are discussed in Chapter V. The cross section is compared to theory in Chapter VI, which is followed by a discussion of the results and conclusions in Chapter VII.

A. Historical Review

One of the great questions in science today is the same question that philosophers asked themselves thousands of years ago, "What is the world made of ?" In

This dissertation follows the style of Physical Review D.

particular, "what are the basic building blocks of matter?" Around 500 B.C., Leucippus and Democritus proposed that if one was able to break matter apart into smaller and smaller pieces, eventually one would not be able to break matter apart any further. These smallest, identical, indivisible particles were called atoms. In the early 19th century John Dalton composed a list of some twenty elements which he called atoms.[1] This eventually led to development of the Periodic Table of Elements, containing all the elements which are now called atoms.

In 1897 Sir J. J. Thompson discovered the electron, which was followed by Lord Rutherford's discovery of the proton in the early 1900's and, in 1932, by Sir J. Chadwick's discovery of the neutron. The atom was found to consist of these new particles and this demonstrated that the atom was not the smallest, identical, indivisible particle. In the 1960's a theory was put forth which suggested that protons and neutrons could be interpreted as composite structures. This theory, called the Gell-Mann & Zweig Quark Model, was verified in the mid-60's by observations made at both SLAC (Stanford Linear Accelerator Center) and CERN (Conseil Européen pour la Recherche Nucléaire), which proved conclusively that the proton was made of quarks.[2]

Our current knowledge of the universe suggests that it is ruled by four forces: gravitational, electromagnetic, weak and strong. The electromagnetic and weak forces are described by the Standard Model of Electroweak Interactions. This model is based on the gauge group $SU(2) \times U(1)$. Quantum Chromodynamics (QCD) is the theory which describes the strong force and is based on the gauge group $SU(3)$. QCD, combined with the Standard Model of Electroweak Interactions, is known as the

Standard Model. The Standard Model is the best theory currently available which describes the electromagnetic, weak, and strong forces. Gravity, the weakest of the four forces, is partially described by the Theory of General Relativity. This last force has not yet been fully unified with the other three forces. Various attempts have been made to incorporate gravity, including Grand Unified Theories (GUT) and Supersymmetric Theories (SUSY), but none of these theories have been confirmed experimentally.[3]

The Standard Model contains at least 24 different particles. There are 12 fermions: 6 leptons, (e, ν_e), (μ, ν_μ) and (τ, ν_τ) and 6 quarks, (u, d), (c, s) and (t, b). There are also 12 bosons, 8 gluons (g) which carry the strong force, the photon (γ) which mediates the electromagnetic force, the $W^{\pm}$ and Z which carry the weak force, plus the Higgs boson (H). Renormalizable gauge theories like the Standard Model allow for the presence of spin 0 particles. The usual formulation of the Standard Model requires at least one spin 0 particle. The Higgs boson is this spin 0 particle, which arises from the spontaneous symmetry breaking of $SU(2) \times U(1)$ and gives mass to the weak gauge bosons and fermions. All the fermions mentioned above have been observed except the t-quark (note, the ν_τ has been inferred from τ decay). Of the 12 Standard Model bosons, all have been observed except the Higgs boson. The discovery of the Higgs boson would be great success for the Standard Model.[4]

The search for ever smaller particles means probing ever smaller distance scales. In order to study these distances, wavelengths that are comparable to the scale being probed must be used. This implies higher and higher energies are needed in order to probe smaller and smaller distances. Accelerators, which provide beams of high

energy particles, are used to probe these distance scales. One of the reasons for building the Superconducting Super Collider (SSC) in Texas is to search these small distance scales for the Higgs boson and help confirm the Standard Model.[5]

B. Experimental Status

Most matter appears to be composed of quarks and leptons. Interactions among these particles, except for the gravitational interactions, are described by the Standard Model. Yet the Standard Model has over twenty free parameters[5] and this large number of parameters makes it hard to believe that this is a fundamental theory. The precise measurement of the Z mass can be used to define only one of these parameters. The mass of the Higgs boson and fermions, and the elements of the Kobayashi-Maskawa (KM) mixing matrix are some of the other parameters in the Standard Model.

In August of 1989, papers from both CDF and MARK II (an e^+e^- experiment at the Stanford Linear Accelerator Center) appeared in Physical Review Letters[6, 7]; these papers presented the first precision measurements of the Z mass and width. In July of 1989, LEP stored it's first beam and already experiments at LEP have improved the precision of the measurement of both the Z mass and width. [8, 9, 10, 11] The masses of the t-quark and the Higgs boson are also parameters of the Standard Model that can be measured experimentally, and direct evidence for these two particles has yet to be found. Preliminary measurements, made at CDF, place the mass of the t-quark above 89 GeV.[12, 13, 14] The discovery of the Higgs boson is a major goal of particle physics. Present limits on the mass of the Higgs boson

place the H^0 mass > 3.9 GeV and the $H^{\pm}$ mass > 19 GeV.[3] The neutral Higgs (H^0) is based on the minimal Standard Model and the charged Higgs ($H^{\pm}$) is based on supersymmetric extensions to the Standard Model. The successes of the Standard Model suggest that these particles should exist; however, if they don't, the Standard Model will be on very shaky ground.

CP-violation has been observed weakly in K^0-decays.[15] However, the magnitude of this violation is small and has only been observed through very precise measurements of the $K^0\,\overline{K}^0$-system. The origin of CP-violation (or T-violation) is a question the Standard Model doesn't address. [16] General principles of relativistic field theories, like the Standard Model, require CPT-invariance. If there is CPT-invariance, then CP-violation and T-violation are permitted. The KM-matrix can easily accommodate CP-violation through the inclusion of a complex phase factor. If this phase factor is non-zero, then CP-violation is allowed[17], however, this doesn't explain the origin of CP-violation.

Searches for free quarks have been undertaken ever since the advent of the Gell-Mann & Zweig Quark Model in the mid-60's. Yet all experiments since 1977 have presented negative results.[3, 18] This has led to the postulate of quark confinement, implying that quarks are trapped inside hadrons. This idea of quark confinement is a key ingredient of QCD. Essentially, in QCD, quarks carry color, and experiments suggest only colorless particles can be observed. Questions of why quarks are confined and why no free quarks can be observed are two more questions the Standard Model doesn't address.

Quarks and leptons in the Standard Model can be grouped into generations, much like the Periodic Table of Elements can be grouped into rows and columns. There are currently three known generations or families in the Standard Model. These families are listed in Table 1. The first generation contains the e, ν_e leptons and the u, d quarks. The next two generations are just heavier versions of the first generation.[17] Why is there more than one generation? This is one of the major unanswered questions of the Standard Model. How many generations are there? Are there more than three? If there are not more than three generations, then why are there three? These are similar questions that may be asked. The number of light neutrino species can be found by measuring the width of the mass distribution for the Z boson. This is because each species of neutrino with mass less than one-half the Z boson mass contributes 180 MeV to the width of the Z boson via the decay mode $Z \rightarrow \nu\,\overline{\nu}$ and hence; the width of the Z boson mass distribution can be used to estimate the number of quark and lepton generations if all neutrinos are less than one-half the mass of the Z boson. Results from the four LEP experiments, at CERN, have ruled out a fourth light neutrino generation at the 98% confidence level.[8, 9, 10, 11]

The large number of quarks and leptons has led to speculations that they are composite structures.[19] Most tests of QCD have only been comparisons to leading-order calculations, next-to-leading-order QCD calculations are now available.[20, 21, 22] These new calculations should allow experimentalists to more precisely test QCD. These precision tests will either be able to verify predictions of QCD and the Standard

Table I. A list of the Standard Model quark and lepton families and their properties.

	Particle			
	Name	Symbol (type)	Charge	Mass (GeV)
	up	u (quark)	$\frac{2}{3}$	4×10^{-3}
First	down	d (quark)	$-\frac{1}{3}$	7×10^{-3}
Generation	electron-neutrino	ν_e (lepton)	0	$< 1.8 \times 10^{-8}$
	electron	e (lepton)	-1	5.1×10^{-4}
	charm	c (quark)	$\frac{2}{3}$	1.5×10^{0}
Second	strange	s (quark)	$-\frac{1}{3}$	0.2×10^{0}
Generation	muon-neutrino	ν_μ (lepton)	0	$< 2.5 \times 10^{-4}$
	muon	μ (lepton)	-1	1.06×10^{-1}
	truth	t (quark)	$\frac{2}{3}$	unknown
Third	beauty	b (quark)	$-\frac{1}{3}$	5×10^{0}
Generation	tau-neutrino	ν_τ (lepton)	0	$< 7 \times 10^{-2}$
	tau	τ (lepton)	-1	1.78×10^{0}

Model, or show deviations from the predicted results. If QCD passes these tests, then all these unanswered questions will remain unanswered; however if deviations from QCD and experiment exist, then the question arises, is there something more? If there is an underlying structure to quarks and/or leptons, then history has shown that theories can usually be simplified when underlying structure is found.

Experiments at both CERN and Fermilab have measured the inclusive jet cross section. [23, 24, 25, 26] The higher energies available at the Fermilab Collider allows for a deeper search into the structure of quarks for compositeness. The current

lower limit for the composite scale of quarks involving a contact interaction (Λ_c), is $\Lambda_c > 700$ GeV.[26] This current limit is from data collected by CDF in 1987 and is based on $\sim 26\ nb^{-1}$ at $\sqrt{s} = 1.8$ TeV. The 1988–1989 CDF run collected more than 100 times this integrated luminosity at the same energy and should be capable of setting a limit of $\Lambda_c > 1$ TeV. The Standard Model successes indicate that if fermions are composite structures, this would happen on a size scale of less than $\sim 10^{-17}$ cm which implies an composite scale of $\Lambda_c \geq 1$ TeV.[5]

C. Theoretical Motivation

The Standard Model is the best theory available. Yet, as outlined above, there are still many unanswered questions such as: why are there three generations? The large number of fermions naturally leads to the question, are fermions elementary or is there something more? By measuring the inclusive jet cross section, the results of this measurement can be compared to QCD and check that the Standard Model is still valid. In the 1988–1989 CDF data run, CDF collected $\sim 4.2\ pb^{-1}$ of data at $\sqrt{s} = 1800$ GeV. A measurement of the inclusive jet cross section from this data set should allow a search for the composite structure of quarks in the TeV range.

1. Quantum Chromodynamics

Jet are believed to originate from the scattering of the quarks (q) and gluons (g) that constitute hadrons.[21] The measurement of the jet cross section for the inclusive production of jets (inclusive jet cross section) is a basic measurement of the scattering from the interactions of these elementary particles. This measurement is therefore a quantitative test of the strong interaction theory (QCD).

Using the parton model ideas as discussed by E. Eichten *et al.* in *Supercollider Physics* [27], the leading order (α_s^2) QCD processes are all 2 body to 2 body processes. Figure 1 is an example of a two jet event which illustrates what the result of a 2-2 body QCD process would look like in the CDF detector. These elementary 2-2 body subprocesses ($\hat{\sigma}_{ij}$), listed in Table II, are combined with the parton probability distributions ($f_i^{(a)}(x_a, Q^2)$), to calculate the leading order QCD inclusive jet cross section. Equation 1 displays the form of the leading order QCD jet cross section used in this analysis and described by E. Eichten *et al.*[27].

$$\frac{d\sigma}{dP_t} = \int dy_1 \int dy_2 \{ \frac{2\pi\tau P_t}{\hat{s}} \sum_{ij} [f_i^{(a)}(x_a, Q^2) f_j^{(b)}(x_b, Q^2) \hat{\sigma}_{ij}(\hat{s}, \hat{t}, \hat{u}) + f_j^{(a)}(x_a, Q^2) f_i^{(b)}(x_b, Q^2) \hat{\sigma}_{ij}(\hat{s}, \hat{u}, \hat{t})] / (1 + \delta_{ij}) \}, \quad (1)$$

where y_1 and y_2 represent the rapidity of jets 1 and 2 respectively, P_t is the common transverse momentum of the two jets, $\hat{s} = s\tau$ is the square of the parton-parton subenergy,

$$\tau = \frac{4P_t^2}{s} \cosh^2 \frac{y_1 - y_2}{2}, \quad (2)$$

$$x_a = \sqrt{\tau} e^{\frac{y_1+y_2}{2}}, \quad (3)$$

$$x_b = \sqrt{\tau} e^{-\frac{y_1+y_2}{2}}, \quad (4)$$

$$\hat{t} = -\frac{\hat{s}}{2}(1 - \cos\theta), \quad (5)$$

$$\hat{u} = -\frac{\hat{s}}{2}(1 + \cos\theta) \quad (6)$$

and Q^2 is the appropriate scale of the hard scattering process.

The choice of Q^2 in Equation 1 is ambiguous since any shift in Q^2 introduces terms in σ_{ij} of order α_s^3 which are neglected in order α_s^2 calculations. However,

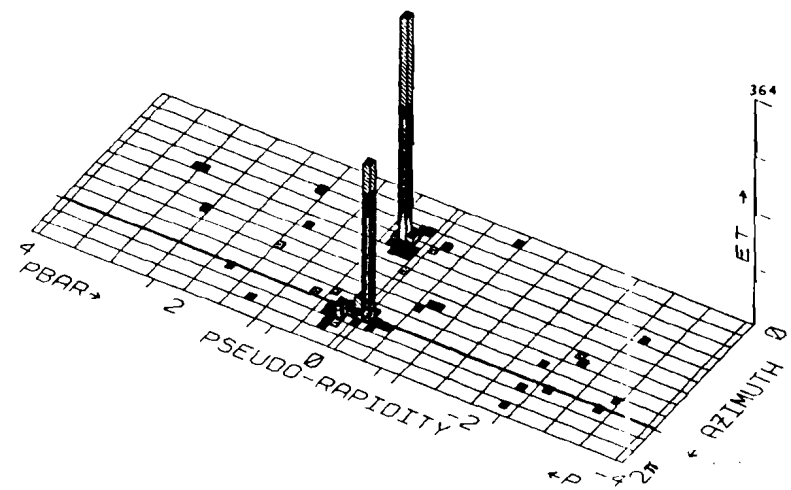

Figure 1. An example of a two jet event, in the CDF detector, which illustrates a 2-2 body QCD process. In η-ϕ space this figure illustrates the location of clusters of energy, jets, in the CDF detector.

according to QCD perturbation theory, the choice of Q^2 should be characteristic of the scale of the hard scattering process. Therefore, Q^2 was chosen to be equal to $P_t^2/2$ in all the leading order QCD calculations used in this analysis and $P_t^2/4$ for the next-to-leading order QCD calculations.

Detailed quantitative studies of the inclusive jet cross section are limited by the ambiguities in the calculation of the cross section. The theoretical ambiguities include the uncertainty in the choice of Q^2 as mentioned above and the uncertainties in the parton distribution functions. Both theoretically and experimentally the precise definition of a jet is also ambiguous. Different experiments are free to define jets in slightly different ways, theoretically at order α_s^2 the jet that is measured in the detector

Table II. Elementary cross sections for leading order α_s^2 QCD subprocesses, given in the form $(\hat{s}/\pi)d\hat{\sigma}/d\hat{t}$.

Subprocess	Elementary Cross Section
$q_iq_j \to q_iq_j$	$\frac{4\alpha_s^2}{9\hat{s}}\frac{\hat{s}^2+\hat{u}^2}{\hat{t}^2}$
$q_i\bar{q}_j \to q_i\bar{q}_j$	$\frac{4\alpha_s^2}{9\hat{s}}\frac{\hat{s}^2+\hat{u}^2}{\hat{t}^2}$
$q_i\bar{q}_i \to q_j\bar{q}_j$	$\frac{4\alpha_s^2}{9\hat{s}}\frac{\hat{t}^2+\hat{u}^2}{\hat{s}^2}$
$q_iq_i \to q_iq_i$	$\frac{4\alpha_s^2}{9\hat{s}}[\frac{\hat{s}^2+\hat{t}^2}{\hat{u}^2}+\frac{\hat{s}^2+\hat{u}^2}{\hat{t}^2}-\frac{2\hat{s}^2}{3\hat{u}\hat{t}}]$
$q_i\bar{q}_i \to q_i\bar{q}_i$	$\frac{4\alpha_s^2}{9\hat{s}}[\frac{\hat{t}^2+\hat{u}^2}{\hat{s}^2}+\frac{\hat{s}^2+\hat{u}^2}{\hat{t}^2}-\frac{2\hat{u}^2}{3\hat{s}\hat{t}}]$
$q_i\bar{q}_i \to gg$	$\frac{8\alpha_s^2(\hat{t}^2+\hat{u}^2)}{3\hat{s}}[\frac{4}{9\hat{t}\hat{u}}-\frac{1}{\hat{s}^2}]$
$gg \to q_i\bar{q}_i$	$\frac{3\alpha_s^2(\hat{t}^2+\hat{u}^2)}{8\hat{s}}[\frac{4}{9\hat{t}\hat{u}}-\frac{1}{\hat{s}^2}]$
$gq_i \to gq_i$	$\frac{\alpha_s^2(\hat{s}^2+\hat{u}^2)}{\hat{s}}[\frac{1}{\hat{t}^2}-\frac{4}{9\hat{s}\hat{u}}]$
$gg \to gg$	$\frac{9\alpha_s^2}{2\hat{s}}[3-\frac{\hat{t}\hat{u}}{\hat{s}^2}-\frac{\hat{s}\hat{u}}{\hat{t}^2}-\frac{\hat{s}\hat{t}}{\hat{u}^2}]$

is associated with the parton, and therefore the jet properties are corrected in order to associate the various quantities with the corresponding partonic quantities. This assumes the parton associated with each jet is detected as a narrow jet of particles and at order α_s^3 this assumption is no longer valid.

The 2-3 body parton scattering subprocesses are listed in Table III. Figure 2 is an example of a three jet event in the CDF detector which illustrates a 2-3 body QCD process. The matrix elements squared for all 2-2 and 2-3 parton scattering subprocesses have been calculated.[28] An immediate consequence of this fact is the ability to calculate the next-to-leading order QCD inclusive jet cross section. [20, 21, 22] At this level a jet can consist of more than a single parton, and therefore the definition of a jet at the theoretical and experimental level become intertwined.

Table III. List of next-to-leading order α_s^3 QCD subprocesses.

Subprocess
$q_iq_j \to q_iq_jg$
$q_ig \to q_iq_j\bar{q}_j$
$q_i\bar{q}_j \to q_i\bar{q}_jg$
$q_i\bar{q}_i \to q_j\bar{q}_jg$
$q_iq_i \to q_iq_ig$
$q_ig \to q_iq_i\bar{q}_i$
$q_i\bar{q}_i \to q_i\bar{q}_ig$
$q_i\bar{q}_i \to ggg$
$q_ig \to q_igg$
$gg \to q_i\bar{q}_ig$
$gg \to ggg$

This is because a decision must be made as to when to count two partons as one jet and when to count them as two jets. In the next-to-leading order calculation of the inclusive jet cross section, the jet definition was chosen in order to agree with the experimental definition as much as possible, thus eliminating possible ambiguities associated with this definition.[21]

A prediction that arises from the definition of the jet in these calculations is the dependence of the cross section on the jet definition. A fixed cone algorithm was used both theoretically and experimentally to define the jet; the clustering cone size was an adjustable parameter in this definition. The inclusive jet cross section at order α_s^3 is dependent on the cone size used in measuring these jets. The dependence of the

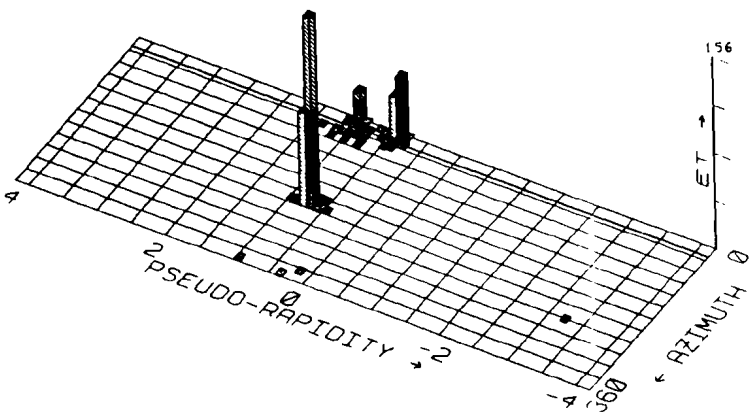

Figure 2. An example of a three jet event, in the CDF detector, which illustrates a 2-3 body QCD process. In η-ϕ space this figure illustrates the location of clusters of energy, jets, in the CDF detector.

cross section on the cone size is an intrinsic feature of QCD and it is important that this be tested experimentally.[21] Due to the fact that the jet is no longer associated with a parton, the jet and its properties as measured in the detector are no longer corrected back to the parton level. Jet corrections must only account for detector effects and not theoretical effects. In this analysis, this implies that corrections for energy lost outside the clustering cone associated with the parton should no longer be applied.

2. Compositeness

In the search for possible breakdown in the Standard Model, it is essential to explore the scattering of the elementary constituents of matter at the highest E_t's

possible. The composite structure of quarks and gluons is one possible source of breakdown in the Standard Model. The measurement of the inclusive jet cross section using the CDF detector allows compositeness to be searched for at the highest E_t's currently available in the world.

The basic assumption underlying most composite models is that the constituent particles interact by means of a new strong gauge interaction.[27] This new strong interaction binds the constituent particles into singlet states at energies below some characteristic scale Λ_c. At energies of a few times the composite scale Λ_c, multiple production processes should dominate over the familiar 2-2 body parton scattering processes. Which processes will occur is model dependent, but in general, the cross section for allowed inelastic processes will be of order $4\pi/\Lambda_c$ and will completely dominate over the standard processes for which the cross section is of order $\pi\alpha_s^2/\hat{s}$. At energies less than Λ_c the comparison with the Standard Model is quantitative.

Compositeness (quark structure) can be approximated by the effect of a contact term added to the QCD lagrangian. In $p\bar{p}$ collisions the production of high-transverse momentum jets is most sensitive to the presence of a flavor-diagonal contact term L_{qq}.

$$L_{qq} = \frac{\pm g^2}{2\Lambda_c}\bar{q}_L\gamma^\mu q_L\bar{q}_L\gamma_\mu q_L, \tag{7}$$

is the form of the contact term for the coupling of left-handed quarks, there are, however, other possible terms. The contact term modifies the cross section and the effects are most apparent at the large values of P_t for which the valence quark interactions dominate the jet cross section.

Comparisons of the measured inclusive jet cross section to composite model predictions based on the presence of a flavor-diagonal contact term will be made in this analysis. By normalizing, the theoretical predictions to the data at small values of E_t where the composite effects are not significant, then the cross section at the higher values of E_t can be examined in order to search for a possible composite signal. The following chapters will examine how this was accomplished using the most recent data collected by CDF.

CHAPTER II

THE CDF DETECTOR

The Collider Detector at Fermilab (CDF) is a general purpose spectrometer designed to explore the details of physics processes at the Fermilab Tevatron center of mass energy, $\sqrt{s} = 1.8$ TeV. In order to measure and identify particles produced at the Tevatron Collider, charged particle tracking, magnetic momentum analysis and fine grained calorimetry are combined to measure the energy, momentum, and where possible, identify the particles. The detector has three main components as shown in Figure 3. These components are a movable central detector and two identical forward/backward detectors situated on either side of the central detector. Figure 4 shows a cut-away view of one half of the complete CDF detector system, the detector is forward/backward symmetric about the interaction point.

The coordinate system for CDF is right-handed and defined to have the origin in the center of the central detector. The x-axis points radially outward in the plane of the Tevatron (the Tevatron is a circular colliding beam machine) forming a line that intersects both the center of the CDF detector and the center of the Tevatron. The y-axis is perpendicular to the x-axis and points upward from the center of the detector. The z-axis points in the direction that the protons are transported, tangent to the Tevatron, originating at the center of the central detector. The radius (R), azimuthal angle (ϕ), polar angle (θ) and z coordinate in the detector system are defined according to standard definitions using this coordinate system.

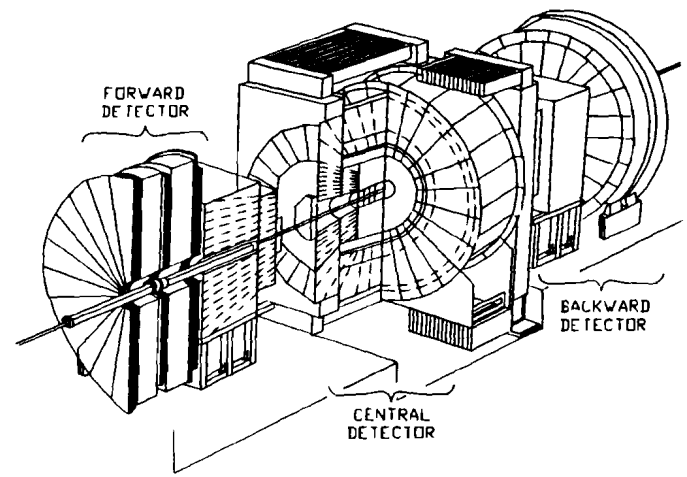

Figure 3. Perspective view of the CDF detector showing the central detector and the forward/backward detectors.

The central detector consists of a solenoid magnet, tracking chambers, electromagnetic shower counters, hadronic calorimeters and muon chambers. The forward/backward detectors consist of segmented time-of-flight counters, electromagnetic shower counters, hadronic calorimeters, and muon toroidal spectrometers. The individual detector components for the central and forward/backward detector systems will be described briefly here. The detector is described in detail elsewhere.[29] Particular attention will be given to the various individual detector systems used in this analysis.

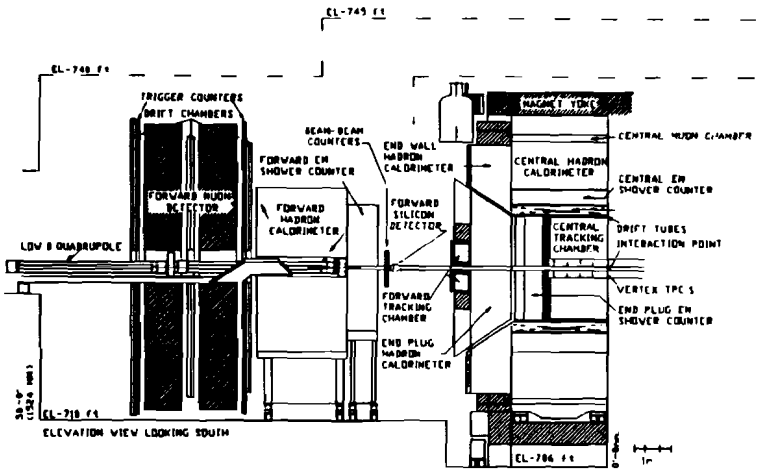

Figure 4. Cut-away view of one-half of the CDF detector showing the individual detector sub-systems making up the central and forward/backward detectors.

A. Tracking

The tracking system used in conjunction with the magnetic field supplied from the solenoid is used to reconstruct particle trajectories and momenta. Particles scattered in the transverse plane of the beam, which originate from proton-antiproton ($p\bar{p}$) collisions near the center of the detector, can be observed in the tracking chambers that surround the region. The vertex time projection chamber (VTPC) is used to find the position of the initial collision and track the charged particles produced at polar angles of greater than 3.5 degrees. The forward/backward tracking chamber (FTC) can reconstruct particles produced in the angular region from 2–10 degrees/170–178 degrees and the central tracking chamber (CTC) combined with the central drift

tubes (CDT) provides a correlated R-ϕ-z measurement of the charged particle tracks in the region from 15 165 degrees.

The data from the VTPC supplied information about the z position of the vertex for the event, which was used to obtain the corrected jet pseudorapidity (η, where $\eta = -\ln(\tan(\frac{\theta}{2}))$) and reject jet backgrounds (see Chapter III). Tracking information in the central detector region was used to measure the jet fragmentation properties (see Chapter IV) and to calculate the charged hadron fraction used in rejecting jet backgrounds (see Chapter III).

1. Vertex Time Projection Chamber

The VTPC covers $\sim$ 7 units of η and was optimized to have good pattern recognition in R-z in order to locate the event vertex and to compliment the R-ϕ tracking of the CTC.[30] The VTPC was designed to find the z vertex of the event, determine the overall event topology, perform charged particle measurements for polar angles of 3.5 176.5 degrees, identify multiple interactions, provide intermediate tracking in the angular region of 10–30 degrees and forward tracking from 3.5–10 degrees. This was required to be done in such a way as to minimize the effects of secondary interactions and multiple scattering, which can degrade electron identification and adversely affect the CTC momentum resolution.

The VTPC consists of eight time projection chambers (TPC) surrounding the beam pipe mounted end to end along the beam direction (z-axis). Each of the eight octagonal modules has a central high voltage grid that divides the module into two

15.25 cm long drift regions. Electrons drift away from this grid and enter the proportional chamber endcaps. The endcaps are divided into octants, where each octant contains 24 sense wires and 24 cathode pads.

The arrival times of the electrons provide the detector information on the R-z shape of the event. Flash analog to digital convertors (FADCs) connected to the sense wires and pads in some endcaps provide dE/dX and ϕ information for particles with a polar angle of 5–25 degrees. Adjacent modules have a relative rotation angle of ϕ_0 = arctan(0.2) about the beam axis, this eliminates inefficiency for particles transversing 2 modules near octant boundaries and provides ϕ information from a small angle stereo measurement.

The resulting performance for the VTPC is described in the following way. For tracks at 90 degrees, the z resolution is 420 μm and at 11 degrees the z resolution is 1100 μm. The impact parameter (b) for tracks with a primary vertex was found to have a rms of 0.3 cm and the overall chamber precision in ϕ is on the order of 100 μm. The 2-track resolution in z is a function of the polar angle, in R the resolution is 6 mm and in ϕ the resolution is 3 cm.

2. Central Tracking Chamber

The CTC was designed for operation in the high magnetic fields and the high density track environment of hadron colliders. It was designed to compliment the calorimeters by providing single particle information. The most important feature of the CTC is its ability to measure high transverse momentum (P_t) isolated tracks which are critical to measurements of high P_t leptons.[31]

The CTC is a large cylindrical drift chamber consisting of 84 layers of sense wires arranged in 9 superlayers. Five superlayers have the sense wires arranged parallel to the beam axis, each superlayer containing 12 sense wire layers. Four superlayers are stereo layers which have their sense wires at an angle of $\pm$ 3 degrees to the beam axis. There are 6 sense wire layers in each stereo superlayer, and the four stereo superlayers are interweaved with the five axial superlayers. The superlayers are divided into cells such that the maximum drift distance is less than 40 mm (800 ns drift time). The chamber surrounds the VTPC and has an inner radial distance of 277 mm, an outer radial distance of 1380 mm, and a length of 3201.3 mm.

The CTC was found to have a 2-track resolution of 3.5 mm, and a spatial resolution of less than 200 μm in R-ϕ and less than 6 mm in z. The momentum resolution of the detector is coupled to the VTPC and the polar angle of the tracks relative to either the proton or antiproton direction. In the angular region of 40-140 degrees, the momentum resolution is better than $\delta p_T/p_T^2 \leq 0.002$ (GeV/c)$^{-1}$.

3. Central Drift Tubes

The CDT was designed to provide high accuracy R-ϕ-z information at a radius of 1.4 m for charged particles in the central region of CDF. Operating in the limited streamer mode (in order to maximize the z resolution), charge division along anode wires provides R-z information, and drift time measurements in the three layers on the CDT array provides R-ϕ information.

Located on the outer surface of the CTC and inside the solenoid, the CDT consists of 2016, 12.7 mm diameter tubes, 3 m in length arranged in three layers of 672 tubes each.[32] The information from the CDT was used in conjunction with the

VTPC and CTC to provide charged tracking information in the η range of $\pm$ 1. The CDT has a typical resolution of 2.5 mm in z and 200 μm in ϕ.

4. Forward Tracking Chamber

The FTC is a radial drift chamber designed to measure and track charged particles in the polar angle range of 2–10 degrees and 170–178 degrees, while operating in a high rate, high track multiplicity environment. It was capable of multi-track resolution of 2–3 mm and had tracking accuracy of 140 μm per wire.[33]

The chambers consisted of 72 wedge shaped cells with planes of anode and field shaping wires that alternate with cathode strips. The wire and cathode planes of each 5 degree cell are slanted at 2 degrees relative to the beam axis so left right ambiguities can be resolved. The anode plane as 21 active 50 μm diameter sense wires and 26 field shaping wires 150 μm in diameter strung normal to the beam axis. The drift space covered from 5.4 mm at the inner radius to 28.2 mm at the outer radius. A total of 3024 active sense wires in both the forward and backward directions provide a R-ϕ-z measurement for each track.

B. Solenoid Magnet Coil

The precise momentum for each charged particle in the CTC was determined using the CTC information while operating in a uniform 1.4 T magnetic field oriented along the beam direction. This field was provided by a 3 m diameter 5 m long superconducting solenoidal coil. The coil was made of 1164 turns of aluminum stabilized NbTi/Cu superconductor, with an overall radiation thickness of 0.85 radiation lengths.[29]

C. Calorimeters

The calorimeters at CDF use a tower geometry because of the importance of jets in high energy $p\bar{p}$ collisions. This type of geometry allows jets to be easily identified. The CDF calorimetry spans an η range of $\pm$ 4.2 and has full azimuthal coverage. The calorimeters are segmented by 0.1 in η and 15 degrees in ϕ for the central and 5 degrees in ϕ for the forward and plug regions. All calorimeter towers have both electromagnetic and hadronic segmentation to allow a detailed comparison of the electromagnetic and hadronic energy composition in the events. In the central region the electromagnetic calorimeters consists of alternating layers of lead absorber and an active medium of scintillator, and in the plug and forward regions the active medium are proportional tubes with pad readout. The hadronic calorimeters consist of the same active mediums, but use steel for the absorber.

In this analysis the central electromagnetic and hadronic calorimeters (CEM and CHA) were used to measure the properties of the jets used in the cross section. Jets measured in the plug electromagnetic and hadronic calorimeters (PEM and PHA) and forward electromagnetic and hadronic calorimeters (FEM and FHA) were used to reject background in the events.

1. Central Electromagnetic Calorimeter

The CEM was designed to incorporate good energy resolution with fine segmentation. This was accomplished by using scintillator and wavelength shifter to measure the energy and an embedded strip chamber for a position determination and longitudinal shower development. The average energy resolution, $\sigma(E)/E$, of $13.5\%/\sqrt{E\sin(\theta)}$ and a position resolution of $\pm$ 2 mm at 50 GeV was measured.[34]

The CEM consists of 48 modules each of length 98 in spanning 15 degrees in azimuthal angle. Four arches of 12 modules each surround the central interaction region on the outside of the solenoid. A total of 31 layers of 5 mm thick SCSN-38 polystyrene scintillator wrapped in 2 layers of 0.0015 in vellum drawing paper were assembled to form 10 projective towers. Interleaved with the scintillator are 30 layers of 1/8 in lead clad with 0.015 in of aluminum. The strip chamber was inserted between the 8th and 9th layers of the scintillator, at a depth corresponding to the maximum average transverse shower development. One wedge was notched with a gap to allow cryogenic service access to the solenoid.

2. Hadronic Central and Endwall Calorimeter

Covering the full 2π azimuthal range and a polar angle from 30–150 degrees, the CHA and endwall hadronic (WHA) calorimeters consist of 48 steel scintillator modules each. Designed to have good energy resolution and uniformity, the calorimeters were initially designed to have an energy resolution of $\sigma(E)/E = 0.50/\sqrt{E}$. Due to other constraints, the total thickness of 80 cm of steel at normal incidence resulted in only 95% containment at 50 GeV, therefore the energy resolution degrades at high energy and muon identification is more difficult.[35]

In the central calorimeter the sampling length is 2.5 cm; in the endwall the sampling is 5.0 cm. Each module is divided into projective towers as in the CEM. This segmentation is fine enough that the quark and gluon jets will normally spread over more than one tower. For each 15 degree slice there are 24 towers, 12 completely in the central, 6 completely in the endwall, and 6 shared between the endwall and central region. The central region covers 45–135 degrees in polar angle and is 32 layers

deep. The endwall covers 30–45 degrees and 135–150 degrees in polar angle, serves as part of the flux return path for the solenoid, and is 15 layers deep. The active medium is 1 cm thick PMMA scintillating plastic doped with 8% naphthalene, 1% butyl-PBD and 0.01% POPOP. The light is collected by wavelength shifters mounted on the sides of the modules.

3. Plug Electromagnetic Calorimeter

The PEM is 2.8 m in diameter, 50 cm deep and uses a lead proportional tube sandwich combined with cathode pad and strip readout to measure energy in the plug regions of the CDF detector. Designed to close the solenoid volume at both ends of the central detector, it is required to operate in a 15 kG field, have fine segmentation, good hermeticity, and good energy resolution.[36] This fine segmentation was essential for isolating electrons and identifying jets.

The PEM covers both ends of the 3 m diameter 5 m long solenoid and occupies a cylindrical hole with an outer radius of 280 cm and a depth of 53 cm, covering a polar angle of 10–36 degrees with full depth coverage up to 32 degrees. It consists of 4 quadrants on each end, each quadrant consisting of 34 layers of proportional chambers interwoven with 2.7 mm lead. Pads are etched on one side of the proportional chambers to form a projective readout geometry. The layers are grouped into three depths. The first and last depth consist of 5 layers, the second depth uses 24 layers. Strips are etched on the other side of the chambers in layers 6–15, these strips alternate between two orthogonal directions layers 6, 8, 10, 12, and 14 have strips in the azimuthal direction and layers 7, 9, 11, 13, and 15 have strips in the radial direction.

4. Plug Hadronic Calorimeter

The PHA has an angular coverage from 10–30 degrees and 150–170 degrees in polar angle and complete azimuthal coverage. It is segmented into 12, 30 degree sectors on either side of the interaction region. Each sector consists of 20 proportional chambers with cathode pad readout sandwiched between 21, 5.1 cm thick steel plates.[37] Each proportional chamber consists of proportional tubes made of 50 micron diameter gold plated tungsten wire centered in a resistive plastic tube, sandwiched by a copper ground plane and copper cathode plane. Each chamber consists of 72 pads arranged to form projective towers in η and ϕ.

5. Forward Electromagnetic Calorimeter

The FEM was designed to be radiation resistant and used in the small angle region in the CDF detector system. Each calorimeter consists of four quadrants containing 30 layers of proportional tube chambers with cathode pad readout sandwiched in between lead sheets.[38] The pads are ganged longitudinally to form a two tower depth segmentation of 15 layers each. There are a total of 1440 pads per layer for a total 5760 tower segments for both the forward and backward calorimeters. Anode wires are strung vertically and are ganged into 5 sectors to provide information on the longitudinal development of the events.

6. Forward Hadronic Calorimeter

Texas A&M University was responsible for the design and construction of the Forward/Backward Hadron Calorimeter (FHA) for the CDF Detector. The FHA was designed to detect and measure the energies and positions of hadrons in the

pseudorapidity range of $2.2 \leq |\eta| \leq 4.2$ with full azimuthal coverage with respect to the beam axis.[39] The FHA consists of both a forward and a backward calorimeter; each calorimeter is divided into four quadrants. The quadrants are made of 27 (204 cm × 196 cm × 2.5 cm) gas proportional tube chambers sandwiched in between 27 (213 cm × 213 cm × 5 cm) steel plates. The chambers are constructed with a cathode pad segmented, in pseudorapidity ($\Delta\eta = 0.1$) and in azimuth ($\Delta\phi = 5$ degrees), into smaller pads. Signals from each of the smaller pads ($\Delta\eta = 0.1$, $\Delta\phi = 5$ degrees) at fixed η and ϕ are summed and form a projective tower in η and ϕ, pointing back to the interaction region of the CDF Detector. Each chamber also contains anode wires segmented into six regions which can be read out separately or summed, thus allowing the measurement of a longitudinal shower distribution for each event.

D. Muon Detection

There are two detector systems to detect and measure muons at CDF. In the central region, each calorimeter wedge contains four layers of muon chambers. In both the forward and backward directions there is a muon spectrometer consisting of magnetized steel toroids, drift chambers, and triggering scintillation counters. Although neither of these systems are used directly in this analysis, muon hits in the central region were used when scanning events to determine the quality of the jet events.

1. Central Muon Chambers

The central muon chambers (CMU) cover the central rapidity region, $|y| \leq 0.7$, in the CDF detector. The chambers in the CMU were designed to detect, identify,

and measure the direction and position of muons by the penetration of muons through 4.9 absorption lengths of material in the central calorimeter.[40]

The detector is located on the outside of the CHA at a radial distance of 3470 mm from the beam axis and is segmented in ϕ into 12.6 degree wedges. Each detector is further segmented into 3 modules of 4.2 degrees each in ϕ. Each module consists of 4 layers of 4 rectangular drift cells. A stainless steel resistive sense wire is located in the center of each cell. A single timing measurement is used for the measurements in the drift direction (ϕ), while charge division on the sense wire is used for measurements of η. The chamber operates in the limited streamer mode, has a rms resolution of 250 μm in the drift direction and a rms resolution of 1.2 mm along the sense wire direction.

2. Forward Muon Chambers

The forward muon spectrometers (FMU) consists of a pair of magnetized iron toroids instrumented with 3 sets of drift chambers and 2 layers of scintillation trigger counters.[41] It was designed to measure the position and momentum of muon in the polar region from 3-16 degrees and 164-177 degrees in the forward/backward region of CDF.

Each plane or set of detectors consists of 24 wedge shape chambers subtending a azimuthal (ϕ) angle of 15 degrees. Each wedge is staggered relative to its neighbors to form overlap regions and eliminate dead spots and detector boundaries. The toroids are 1 m deep, with an outer diameter of 7 m and an inner diameter of 1 m. Two of the four 395 ton magnets are located at both the forward and backward detector regions. Each toroid is made of 4 rectangular coils consisting of 28 turns of copper to

provide an azimuthal field in the steel. Each chamber consists of two planes of drift cells. The plane closest to the interaction region consists of 56 cells and the other plane consists of 40 cells staggered relative to the first plane so as to resolve left-right ambiguities. Each cell contains a stainless steel sense wire strung along the cord to provide a polar angle measurement and the two sides of the chamber share a common copper foil cathode plane divided into 15 cathode pads.

E. Data Acquisition System

The CDF detector has a total of 100,000 electronic channels for readout of the various detector components. The calorimetry requires a large dynamic range to measure energy of a few tens of MeV to hundreds of GeV; therefore a special front end electronic system called RABBIT was developed to handle these requirements. Before any of this could be readout, a trigger system also had to be developed to exploit the design of the projective geometry in the calorimeter towers. The beam-beam counters are the first layer of the trigger system. The various aspects of these systems will be discussed briefly in this section.

1. Front End Electronics

The front end electronics at CDF are based on the RABBIT (Redundant Analog Bus-Based Information Transfer) system.[42] This crate based front end system features low cost, compact packaging, fast readout, command capability, 16 bit digitization and a high degree of redundancy. The crates can contain a variety of instrumentation modules and are designed to be placed near the detector. Since access to the CDF detector is not possible during machine operation, the electronics had to

be designed to perform all normal operations without physical access to the system. The components of the RABBIT system are the RABBIT crate, the system modules, front end instrumentation modules, and special purpose processors to direct readout. The overriding design specifications for the system required it be able to read many calorimeter channels within 1-2 ms for which the ratio of full scale signal to calibration signal would be 1000:1. It was also necessary to have a calibration accuracy of 1%.

2. Data Acquisition

All CDF events are collected in a multilevel FASTBUS network.[43] The choice of FASTBUS was motivated by the ability of FASTBUS to support high data rates and both high speed devices (synchronous transfers) and low speed devices in asynchronous full handshake transfers. The data acquisition (DAQ) and trigger systems operate in a hierarchical structure. The level 1 and 2 triggers must filter the raw interaction rate down to 100 Hz or less. The 100 Hz rate a practical limit at which events can be digitized and buffered.

If an event is accepted by both the level 1 and level 2 triggers, the front end crates are digitized and readout by scanner modules. The calorimetry and the central muon chambers are readout by MX scanners (MX scanners are used to access RABBIT front end electronics), and the tracking systems use a SSP scanner (SSP scanners are used to access FASTBUS based front end electronics). Each scanner has four event buffers. Once all MX and SSP scanners have finished reading and buffering an event, a trigger supervisor module signals the buffer manager the event is ready. The buffer manager (BFM) controls data flow from the scanners to the VAX host

computers. The BFM signals the event builder (EVB) to read a specified buffer and reformat the complete event. When the EVB finishes, it signals the BFM, which in turn instructs the trigger supervisor the specified buffer is now available for a new event.

From the EVB, the event is passed onto the level 3 trigger which uses VME based processors and control modules developed by the Fermilab Advanced Computer Program (ACP). The BFM instructs the EVB to write out an event to one of the ACP processors. Events accepted by level 3 are then read by the Buffer Multiplexor executing on the VAX cluster. The event can then be logged to disk or tape to be accessed in real time by computer processes executing on both host and remote VAX computers using DECNET.

3. Beam-Beam Counters

The beam-beam counters (BBC) provide a minimum bias trigger for the CDF detector and are used as the primary luminosity monitor for CDF.[29] The BBC consists of a plane of scintillation counters on the front face of each the forward and backward shower counters, each consisting of 16 time-of-flight counters. These counters (BBC) have excellent timing properties (a timing resolution of 200 ps) and provide the best measurement of the time of the interaction, as well as a crude measurement of the z vertex (within 10 cm at the trigger level). These counters are arranged in a rectangle around the beam pipe and cover the angular region (measured in either the horizontal or vertical direction) of 0.32-4.47 degrees.

4. Triggering

A two level FASTBUS based trigger system provide the initial triggers for the CDF detector.[44] The purpose behind this multi-level trigger system is to introduce as little bias as possible at the lowest trigger levels, while reducing the event rate so the higher trigger levels can do a more sophisticated analysis without a significant amount of time lost. The readout of the CDF detector by the data acquisition system is the most time consuming process which takes on the order of 1 ms.

Analog signals are used to form sums and moments before digitization in order to have a fast trigger. This is done using 10 FASTBUS analog crates which can be identified by type of calorimeter signal (electromagnetic or hadronic) and geographic location (central, plug and forward detector regions). Calorimeter towers are summed into towers of $\Delta\phi = 15$ degrees and $\Delta\eta = 0.2$, these signals are then sent to the corresponding FASTBUS analog crate. Receive and weight (RAW) cards in the crates compensate the various detector components so that a 50 GeV transverse energy (E_t, where $E_t = E\sin(\theta)$) deposition produces a -1 volt signal. These signals are passed onto a compare and sum (CAS) card which sums all the towers in a single RAW card above some threshold. The CAS card sums three different quantities, the linear sum, the sum weighted by $\sin\phi$, and the sum weighted by $\cos\phi$. An inclusion register controls which channels will be added into the sum so that bad channels can be turned off.

The crate sum boards take the three sums (E_t, $E_t \sin\phi$ and $E_t \cos\phi$) and converts them from analog to digital signals. At the same time, since each CAS card has a mean η hardwired into it, the crate sum board also calculates the sum $E_t\,\eta$ and

$E_t\,\eta^2$. After being digitized by the crate sum, the sums for all the separate detector components are brought together in the level 1 sum board. There is one level 1 sum board for each quantity summed (E_t, $E_t \sin\phi$ and $E_t \cos\phi$). Each board creates a grand total sum of the electromagnetic, hadronic and combined E_t, which are then compared to programmable thresholds.

The level 2 trigger uses a cluster finder board interacting with the CAS board. In level 2, the outputs from the CAS boards are loaded into the cluster finder which then process the data and returns a set of towers corresponding to one cluster of energy. The algorithm for finding clusters used in the cluster finder is the nearest neighbor algorithm and will be discussed in Chapter III. Following a similar path as in level 1, level 2 then proceeds to find the E_t, $E_t \sin\phi$, and $E_t \cos\phi$ for each individual cluster, as well as $E_t\,\eta$ and $E_t\,\eta^2$.

The first two levels of the CDF trigger, as discussed above, are able to reduce the raw event rate of 50-75 kHz to 1-100 Hz introducing as little bias as possible.

CHAPTER III

MEASUREMENT OF JETS AT CDF

The processes required to measure the inclusive jet cross section are examined in this chapter. The measurement of the cross section begins with the definition of a jet and the physical quantities associated with a jet. The collection of the jet data and the processing of this data are discussed next. This is followed by a description of background and fiducial cuts needed before the jet cross section can be extracted. Finally, the procedure used to extract the jet cross section from the data is explained.

A. Jet Definition

In proton-antiproton ($p\bar{p}$) collisions, parton-parton scattering gives rise to jet production. Experimentally, the signature of a jet is a large energy deposit in a localized area of the detector. Theoretically and experimentally, the definition of a jet is ambiguous.[21] Choosing an appropriate algorithm to find and measure the physical properties of jets in the detector will be discussed here. How these jets and the measurement of their physical properties are compared to theory will be discussed in the next chapter.

The CDF calorimetry is segmented in azimuth (ϕ) and in pseudorapidity (η, where $\eta \equiv -\ln(\tan\frac{\theta}{2})$), as shown in Figure 5. This type of segmentation forms towers which project from the center of the detector where the collision nominally takes place outward. Most particles coming from the interaction region near the center of the detector shower in the calorimeters and are observed as towers of energy

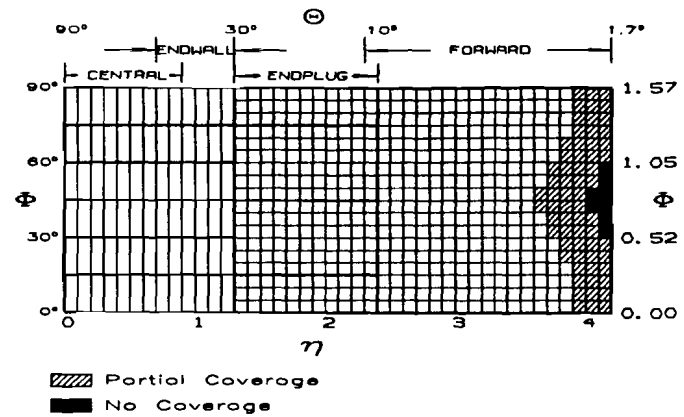

Figure 5. An example of the η-ϕ segmentation in one quadrant of the CDF hadronic calorimeter.

(see Figure 6). This projective geometry allows jets to be identified by algorithms which collect the towers into clusters of energy.

The types of algorithms typically used in $p\bar{p}$ experiments are nearest neighbor[45, 46] and fixed cone.[26, 24] Each clustering algorithm starts with a list of seed towers. A seed tower is a single calorimeter tower with a transverse energy (E_t, where $E_t \equiv E\sin\theta$) greater than some threshold ($E_{t_{seed}}$).

In the nearest neighbor algorithm used in the trigger at CDF,[45] a list of candidate towers is then generated where a candidate tower is a calorimeter tower with E_t above a second threshold ($E_{t_{cand}}$). This algorithm then examines the 4 nearest neighbor towers (diagonal towers are not included, another algorithm examined by

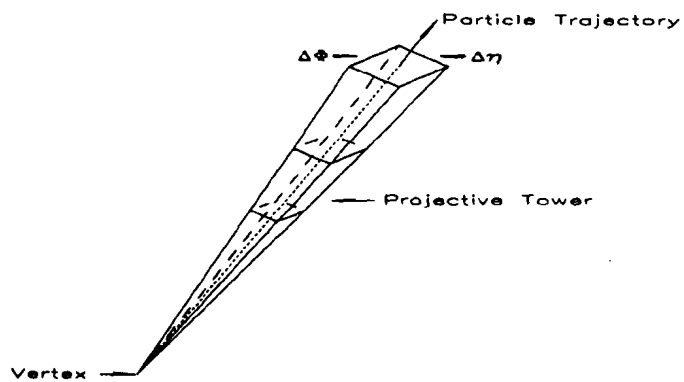

Figure 6. An illustration of a particle transversing a projective tower.

CDF used the 8 nearest neighbor towers)[47] of the seed tower and merges them with the seed tower if they are candidate towers. This process is then repeated using the candidate towers passing this requirement as seed towers until no new candidate towers are merged. The whole procedure of finding jet clusters is repeated until no further seed towers exist.

Another type of algorithm examined by CDF is the variable cone algorithm.[47] For both the variable and fixed cone algorithms, the cone size (R) in η ϕ space is defined to be $R = \sqrt{\Delta\eta^2 + \Delta\phi^2}$. The variable cone algorithm also forms a list of candidate towers as in the case of the nearest neighbor algorithm. Candidate towers are then merged with the seed tower if they are inside a cone of radius that varies as a function of E_t, where the E_t is initially the E_t of the seed tower. Then, for

this algorithm, a new E_t is calculated from the resulting merged cluster. The change in E_t is then used to compute the ratio $\frac{\Delta E_t}{E_t}$, and if this ratio is greater than some fraction (0.02), a new cone size (which is now a function of jet E_t) is calculated and new candidate towers are merged. This process is repeated until $\frac{\Delta E_t}{E_t}$ is less than the chosen ratio or the process of calculating R has been repeated a maximum of five times. This procedure is again repeated until no more seed towers remain.

At CDF, jets are identified based on a fixed cone algorithm. This algorithm forms a list of seed and candidate towers as described above with $E_{t_{seed}} = 1.0$ GeV and $E_{t_{cand}} = 1.0$ GeV. Towers in the forward and endplug region (see Figure 5) are joined together in ϕ in order to correspond to the tower segmentation found in the central region. Next, preclusters are formed from chains of contiguous towers that decrease in E_t, as in the nearest neighbor algorithm (using the 8 nearest neighbors). The preclusters with E_t greater than 1 GeV are then used as starting points for clustering as shown in the flow chart in Figure 7. The E_t weighted centroid of the precluster is found and a fixed cone in η-ϕ space is placed around this centroid. Candidate towers inside this cone are then merged together using the true tower segmentation (no joining in ϕ). A new centroid is calculated and a new cone is drawn with this centroid as its center and a new list of merged towers is generated. This process is repeated until the list of merged towers in the cone remains unchanged.

The procedure is repeated until no preclusters remain.

Overlapping jets, that is jets that contain all or part of another jet cluster, are potentially difficult for any jet clustering algorithm. CDF handles this by comparing the amount of E_t in towers common to both clusters to the amount of E_t in the smaller cluster. If the ratio of these two numbers is larger than some cutoff (0.75), the two clusters are merged into one cluster. If this ratio is smaller than this cutoff, then clusters are kept as separate jets and the towers in the overlap region are divided between the two jets based on their distance from the centroid of each cluster. New centroids are then computed for each cluster and the original overlapping towers are then re-divided accordingly. This process is repeated until the list of towers in the clusters remains unchanged.

All of these algorithms were examined in detail for the analysis of CDF's 1987 data set.[47] The fixed cone algorithm was chosen over the other algorithms for several reasons, including the stability of this algorithm in measuring energy and position in the presence of other clusters, and the relative sharpness in η-ϕ space for its ability to distinguish between separate jets.

The various physical quantities of the jet are characteristics which can be measured experimentally. CDF uses the following definitions for the energy, momentum, transverse momentum and transverse energy of the jet. The energy of each jet is defined to be the sum of the energies found in all the towers inside this cone,

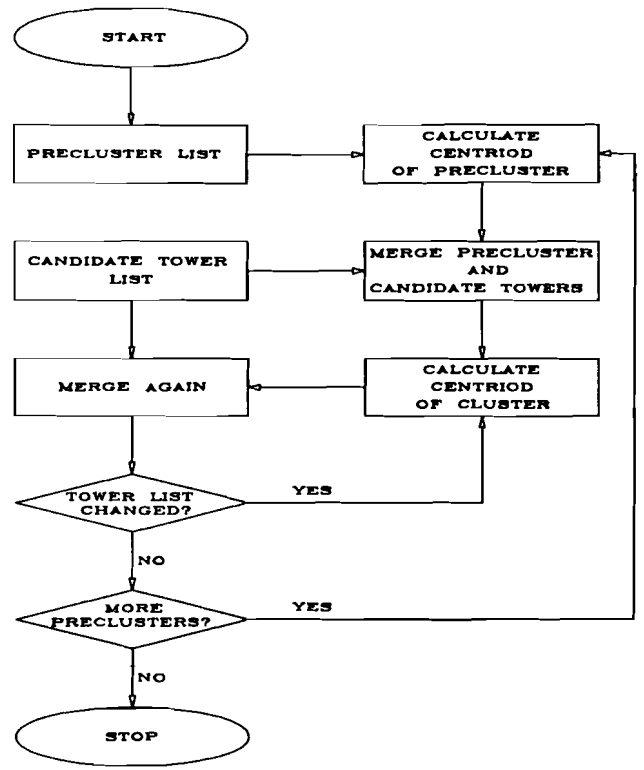

Figure 7. Flow chart of the fixed cone algorithm used by CDF, starting after candidate tower, seed tower and precluster lists have been formed.

$E = \sum_{i=1}^{\#\text{ towers in cone}} E_i$. The momentum is calculated by assuming the center of each tower consists of massless particles and then defining:

$$P_x = \sum_{i=1}^{\#\text{ towers in cone}} E_i \cos\phi_i \sin\theta_i, \tag{8}$$

$$P_y = \sum_{i=1}^{\#\text{ towers in cone}} E_i \sin\phi_i \sin\theta_i, \tag{9}$$

$$P_z = \sum_{i=1}^{\#\text{ towers in cone}} E_i \cos\theta_i, \tag{10}$$

$$|P| = \sqrt{P_x^2 + P_y^2 + P_z^2}, \tag{11}$$

where E_i, ϕ_i, and θ_i are the energy, azimuth, and polar angle of the *ith* tower. The transverse momentum (P_t) and E_t, of the jet are defined as follows:

$$P_t = \sqrt{P_x^2 + P_y^2}, \tag{12}$$

$$E_t = E(P_t/|P|),$$

$$= E\sin\theta, \tag{13}$$

where E, P, and θ are the energy, momentum, and polar angle of the jet.

The definition of a jet that CDF uses is compatible with that found in next-to-leading order QCD inclusive jet cross section calculations done by S. Ellis, Z. Kunszt and D. Soper.[21] One difference in the two algorithms is the definition of E_t. The next-to-leading order QCD calculation defines $E_t = \sum_i E_i \sin\theta_i$ whereas in the CDF algorithm $E_t = \sum_i E_i \sin\theta$, where θ is the polar angle for the E_t weighted centroid of the jet. This difference is not expected to be larger than the theoretical uncertainties associated with the cross section.[21]

B. Data Collection and Triggering

During the period from August 1988 until June 1989, CDF collected 4×10^6 events corresponding to 4.2 pb^{-1} of integrated luminosity on 5,500 magnetic tapes. Collecting this amount of data required the ability to search the information recorded by the detector quickly for interesting events and to store these events on tape for later use. This was accomplished using a multiple level trigger. The trigger contained 4 different levels where each succeeding level reduced the amount of data by placing more stringent requirements on the data.

The first level (Level 0) of triggering required a coincidence between the east and west beam-beam counters, as described in Chapter II. Events passing this requirement then went on to the next level of triggering (Level 1). The Level 1 jet trigger summed (using the calorimeter summer[45]) all trigger towers above 1 GeV and required this sum to be either greater than 20 or 18 GeV, depending on which trigger was being used. Events passing the Level 1 trigger were then sent on to the Level 2 trigger.

The Level 2 trigger was the main level of triggering used for this jet measurement. Events in this trigger were required to contain at least one jet cluster with E_t greater than 20, 40, or 60 GeV, where the 20 and 40 GeV triggers were rate limited (pre-scaled). Initially, the pre-scale factors for the 20 and 40 GeV triggers were 100 and 10 respectively. These pre-scale factors were chosen to keep the overall trigger rate at around 1-2 Hz, the rate at which the tape drives could be operated reliably. This increases the efficiency for collecting the data by reducing the amount of time lost in writing data to magnetic tape. These factors were changed to 300 and 30 later in order to decrease the amount of time lost collecting data when the luminosity of the

beam grew larger. Jets clusters were found by the Level 2 cluster finder which used a nearest neighbor algorithm to cluster jets. This algorithm required a seed tower of greater than 3 GeV and summed candidate towers of greater than 1 GeV.[48]

The Level 3 trigger was used to further filter the jet events. Level 3 is capable of executing algorithms written in FORTRAN 77, similar to the event reconstruction program used offline to process the data.[49] This allowed algorithms which filtered noise and other backgrounds from the events to be run before recording the event to tape. This was only used during the later runs and required the event to have passed the Level 2 trigger before it was used. Since the same requirements of the Level 3 trigger were made when processing the data offline, this trigger was equivalent to selecting events which passed the Level 2 trigger and had gone through offline event reconstruction, except that it controlled which events were to be written to tape. Therefore, for this analysis an event was only required to pass the Level 2 trigger and to have gone through the event reconstruction processing.

C. Event Reconstruction

Analysis of the jet data begins with the reconstruction of the events stored on tape. The reconstruction program was used to filter noise from the data and remove events from individual runs with known detector problems. Some of the sources of noise were pedestal shifts, bad electronics cards, "Texas Towers "(large energy spikes, thought to be associated with low energy neutrons first observed in the forward hadron calorimeter)[50], and cable noise on the cables connecting the detector to the electronics. Runs with known detector problems were runs with the

high voltage turned off to part of the detector as well as runs with bad MET centering in the central detector (MET centering is the mean average missing E_t calculated using minimum bias events)[51, 52]. Reconstruction also took raw data and processed it into a format easily accessible to individual analysis programs.

The process started by filtering the events according to trigger and then removing events which came from runs with known detector problems. The event vertex was then reconstructed and raw calorimeter data was converted into energy. Next, filters were used to clean the events of noise [53, 54, 55, 56] and remove events containing cosmic rays not in coincidence with event crossings.[57] Tracks were reconstructed in the central tracking chamber and jets were clustered using the fixed cone algorithm (discussed in the first section of this chapter) with cone sizes of 0.4, 0.7 and 1.0. Figure 8 is a flow chart which illustrates the reconstruction path used for the jet data.

Data structures containing trigger, vertex, tracking and jet information were then written to special files for analysis. This eliminated the need for the raw data and reduced the storage size of the data while maintaining all the necessary information needed for the final analysis.

D. Background Cuts

To attempt to make any kind of a measurement of the jets themselves, it was necessary to remove non-jet events from the data sample. Cosmic ray bremsstrahlung is one source of non-jet events. Thus, it was necessary to define criteria to identify these types of events and remove them from the event sample. To study the criteria

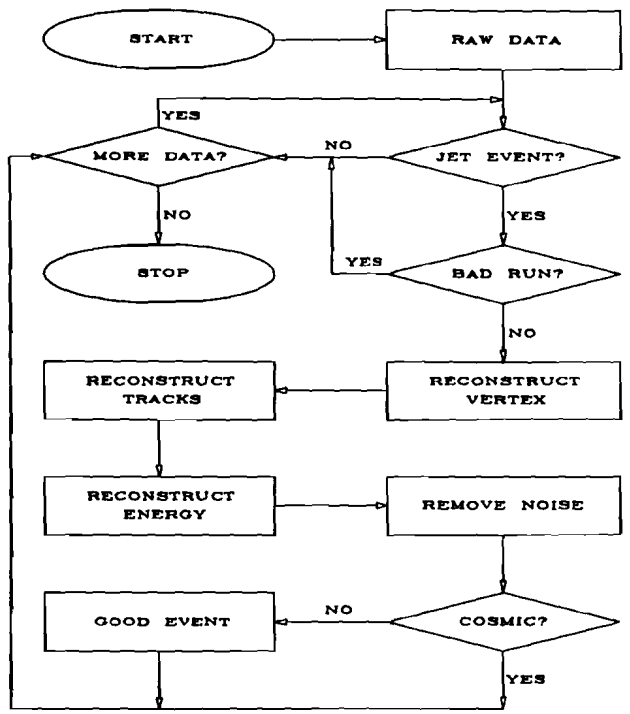

Figure 8. Flow chart illustrating the reconstruction path used for the jet data.

necessary to remove these cosmic rays, a data set which consisted of 845 nb^{-1} (187260 events) of reconstructed data (with jets clustered using a cone size of 0.7) was used.

Three quantities were used to determine the characteristics of an event in order to distinguish jet events from background.[58, 59] These quantities EMF, CHF, and MET will be described below. Cuts were made on these quantities and the events were classified according to which cuts they passed and which cuts they failed.

A jet is expected on average to have an electromagnetic fraction (EMF) between zero and one. Cosmic ray bremsstrahlung, on the other hand, tends to leave energy in either the hadronic or electromagnetic calorimeter, thus having an EMF near zero or one. The EMF of the highest E_t central jet was examined, but high energy photons or π^0's also have an EMF near zero or one thus EMF was re-defined to be a more global quantity. EMF was re-defined to be the E_t weighted EMF over the whole detector as follows:

$$EMF = \frac{\sum_{j=1}^{N_{jet}} E_{t_j} \times EMF_j}{\sum_{j=1}^{N_{jet}} E_{t_j}}, \tag{14}$$

where N_{jet} is the number of jets with $E_t > 5$ GeV, E_{t_j} is the E_t of the jth jet and EMF_j is the EMF of jet j. This re-definition of the EMF considers the event as a whole instead of just one isolated jet in the event which may contain some interesting physics.

The value of this cut defined events with $0.1 \leq EMF \leq 0.95$ to be acceptable. Figure 9 shows the EMF for each event calculated by using the EMF of the highest E_t central jet. Figure 10 shows the EMF for each event as defined in Equation 14. The large spike observed in Figure 9 near zero is a result of events which contained

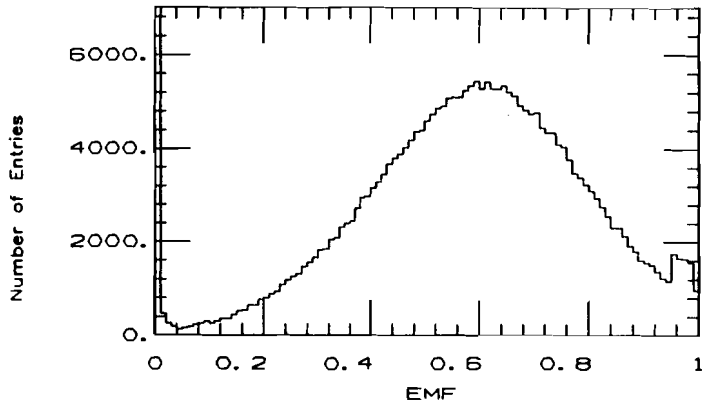

Figure 9. EMF of highest E_t central jet in each event.

no jets above 10 GeV in the central calorimeter. The tails of Figure 10 show that the cuts used are reasonable.

Partons originate from a $p\bar{p}$ collision and then emerge from the event vertex as a spray of both charged and neutral particles which leave energy in the calorimeter and are clustered into jets. Charged particle tracks associated with the jets, can then be reconstructed in the central tracking chamber. Cosmic rays and other backgrounds do not originate from the center of the detector and may or may not pass through the tracking chamber. Therefore, few if any tracks are found pointing at clusters of energy associated with these backgrounds. The next cut used was based on this premise and used the charged hadron fraction (CHF) to determine whether the event may be a jet event or a non-jet event. The CHF of the event was calculated by first

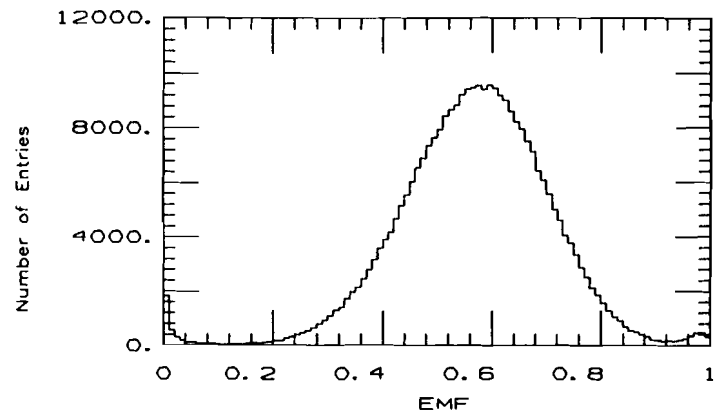

Figure 10. E_t weighted EMF for each event (EMF).

finding all tracks pointing to each jet within a cone of 0.7 centered on the η and ϕ of the jet. Since the tracking was only available in the central calorimeter, only the central area was used in this study. Therefore, there was an additional cut requiring $|\eta_{detector}| \leq 0.7$, where $\eta_{detector}$ is the pseudorapidity of the jet calculated, assuming a vertex of zero. CHF was then calculated as follows:

$$CHF = \frac{\sum_{j=1}^{N_{\rm jet}} \frac{(\sum_{i=1}^{\#\,\rm Tracks} P_{t_i})_j}{E_{t_j}}}{N_{\rm jet}}, \tag{15}$$

where $N_{\rm jet}$ is the number of jets with $E_t > 10$ GeV, $(\sum_{i=1}^{\#\rm Tracks} P_{t_i})_j$ is the sum of the P_t of all the tracks in a cone of 0.7 around jet j as measured by the tracking chamber, and E_{t_j} is the E_t of jet j as measured by the calorimeters. To pass this cut, the event was required to have $CHF \geq 0.175$ in order to be accepted. Figure 11

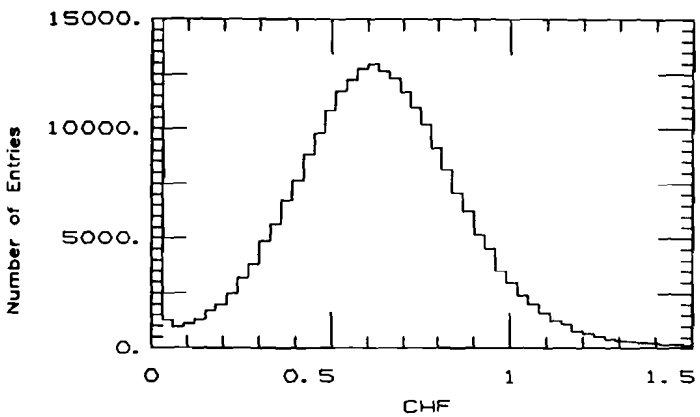

Figure 11. Average P_t/E_t for all central jets in each event (CHF).

shows this quantity as defined in Equation 15 for each event and shows that this cut is reasonable.

The final cut used was based on Missing E_t significance (MET). Physics requires momentum to be conserved. In particular, since the initial beam particles (protons, anti-protons) have little or no momentum transverse to the beam direction, the total transverse momentum (P_T) is expected to be small or zero from conservation laws. Typically, a jet event will have two jets which balance in P_t (see Appendix A). More specifically, for two jet events, the jets will be separated by approximately 180 degrees in azimuthal angle (ϕ) and will have approximately equal amounts of E_t. MET is a measure of this balancing. Cosmic rays tend to deposit all their energy into one cluster and will have no balancing energy cluster, further, if they do manage

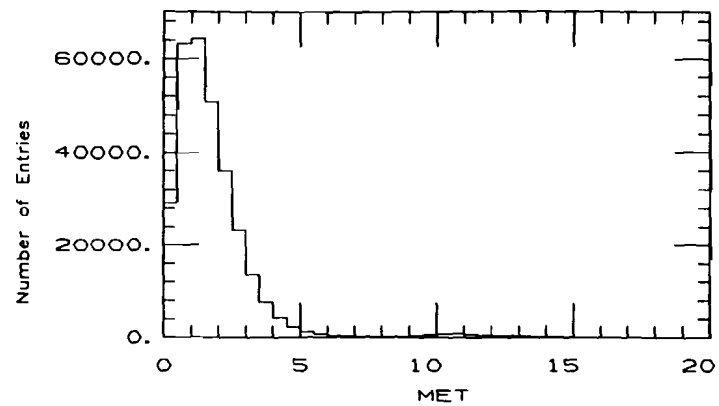

Figure 12. Missing E_t significance for each event (MET).

to deposit energy into two separate clusters, these clusters tend not to be separated in ϕ by 180 degrees, hence they can be identified and removed. MET was calculated as follows:

$$MET = \frac{((\sum_{j=1}^{N_{\rm jet}} E_{t_j} \times \cos\phi_j)^2 + (\sum_{j=1}^{N_{\rm jet}} E_{t_j} \times \sin\phi_j)^2)^{\frac{1}{2}}}{0.8 \times (\sum_{j=1}^{N_{\rm jet}} E_{t_j})^{\frac{1}{2}}}, \qquad (16)$$

where $N_{\rm jet}$ was the number of jets with $E_t > 5$ GeV and the event was considered acceptable if $MET \leq 6.5$. Figure 12 shows the value of this quantity as defined in Equation 16 for each event.

The events were then classified based on these cuts as shown in Table IV. Because certain real physics processes can fail at least one of these cuts, and cosmic rays are expected to fail the majority of these cuts, events were required to pass at

Table IV. This is the event classification scheme for determining backgrounds in jet events. All classes of events are shown. The numbering scheme for the classes was for simplicity in coding.

Class	Criteria	Category
Class 0	No Central Jets with $E_t > 10$ GeV	Non-Central
Class 5	$EMF < 0.10, CHF > 0.175, MET > 6.5$	Cosmic
Class 6	$EMF > 0.95, CHF > 0.175, MET > 6.5$	Cosmic
Class 11	Failed 2 of 3 cuts	Cosmic
Class 21	Failed 1 of 3 cuts	Jet Event
Class 31	Failed 0 of 3 cuts	Jet Event

least two of these cuts in order to be accepted as jet events. Figures 13, 14, and 15 show correlations between EMF, CHF, and MET. These figures show that the majority of the events tend to satisfy at least two of these cuts. While the rest of the events form isolated islands in these figures where the cosmic rays and other jet backgrounds are expected to be.[58]

The number of events in each Class is shown in Table V for the events in the data sample used in this study. The 19 events with no classification are events which did not contain a jet cluster.

Most of the Class 5, 6, 11, and 21 events with at least one jet in the central calorimeter having an $E_t \geq 100$ GeV were then scanned. Scanning involved interactively examining each event using a display program which showed how the event looked in the detector. The calorimeter energy, tracks and muon hits were examined

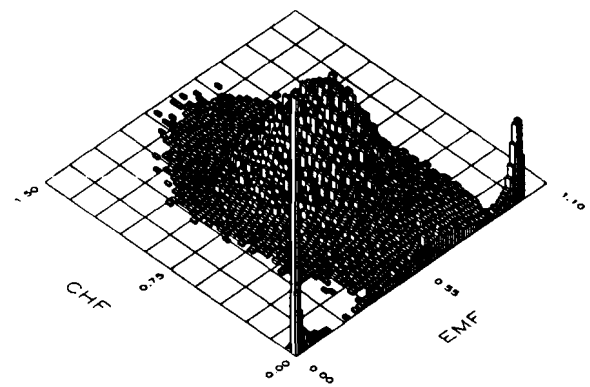

Figure 13. CHF versus EMF.

in order to determine whether the event was background or not. All events in Class 21 and 31 with at least one jet in the central with $E_t \geq 175$ GeV were also scanned. (Note that events were not double counted for Class 21 events with $E_t \geq 175$ GeV.) The results are summarized in Table VI.

Table VI shows Class 11 was the place where the efficiency for distinguishing between jet events and background was the worst. However this Class only represents 0.09% of the total; thus by filtering on Classes 5,6, and 11 only about 2.9% of these discarded central events were jet events while only 0.2% of events kept were cosmic rays.

Figure 16 shows the effective cross section for these background events as determined using the data set and cuts described above. This means discarding events in

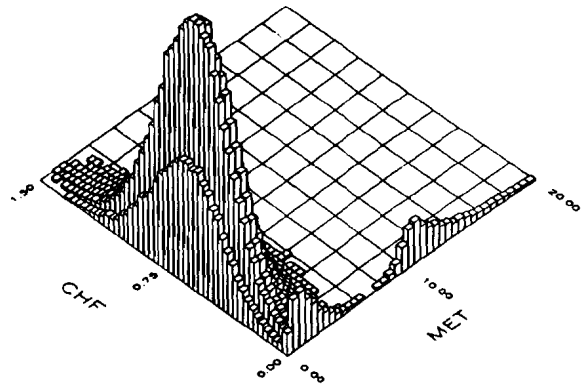

Figure 14. CHF versus MET.

Classes 5,6 and 11 as background and only keeping events in Class 21 or 31. (Class 0 events are also discarded, not because they are cosmic background, but because they are non-central events.) Figure 17 shows the fraction of events discarded versus E_t. The expected cosmic ray background at CDF has been investigated[60] using a monte carlo simulation. The simulation included the effects of energy loss by cosmic rays due to bremsstrahlung, e^+e^- pair-production, and knock-on processes. The expected rates in the central hadronic calorimeter (CHA) and the central electromagnetic calorimeter (CEM) were calculated. Then using Table VI, Figure 16 was scaled and compare this to these results. Figure 18 shows the results of this study.

From the results shown here, it has been demonstrated that these cuts are very efficient in removing the cosmic background from the data sample. The agreement

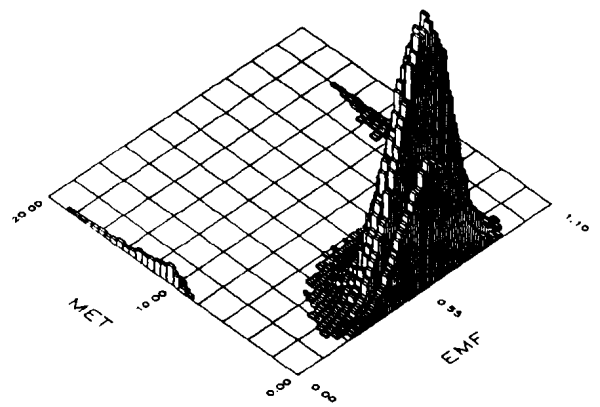

Figure 15. MET versus EMF.

between the predicted rates of cosmic rays with the rates found in the data shows these cuts are efficient at removing cosmic background from the data. In fact, the corrections for residual background contamination and for inefficiencies are so small that there is no reason to correct for this.

E. Acceptance Region

The calorimetry at CDF is broken up into three main detector regions, the central region with a pseudorapidity (η) from $-1.3 \leq \eta \leq 1.3$, the plug region covering $1.3 \leq |\eta| \leq 2.4$, and the forward region for $2.3 \leq |\eta| \leq 4.2$. In the central region the calorimeter is made of scintillator and absorber, whereas in the plug and forward regions the calorimeters are gas proportional chambers. Gaps are

Table V. Number of events per Class, found in the data sample used in this study.

Class	Events	Percent of Total (%)
Class 0	41098	21.95
Class 5	430	0.23
Class 6	276	0.15
Class 11	175	0.09
Class 21	3852	2.06
Class 31	141410	75.51
No Class	19	0.01
Total	187260	100.00

Table VI. Results from event scanning.

	Jet		Cosmic		
Class	Events	%	Events	%	Total Events
Class 5	0	0.0	96	100.0	96
Class 6	0	0.0	48	100.0	48
Class 11	3-4	11.1-14.8	24-23	88.9-85.2	27
Class 21	102	100.0	0	0.0	102
Class 21 and 31	400	99.8	1	0.2	401

found in the regions that separate these various detector components. These gaps, combined with the different detector components, cause the jet resolution and the

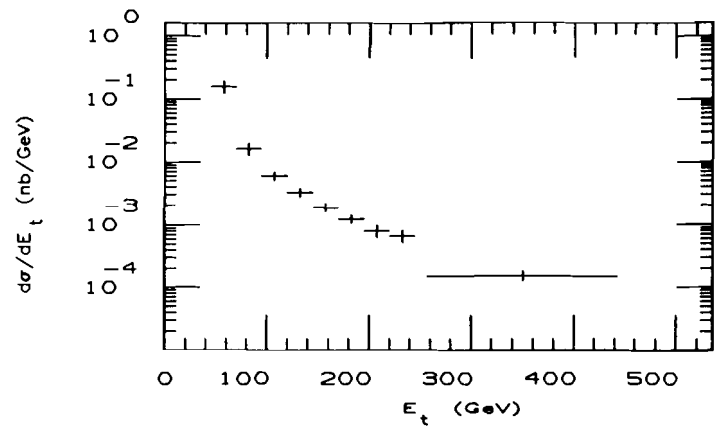

Figure 16. Effective cross section for jet backgrounds; Class 5, 6 and 11.

jet energy corrections to be dependent on the the η of the jet. QCD predicts a flat spectrum at $\eta = 0$ and the rate drops off by approximately 8% at $\eta = 1.0$.[61]

To insure full acceptance and a uniform detector response, the event vertex was restricted to be within 60 *cm* of the center of the detector and the jets were restricted to have a detector pseudorapidity centroid of $0.1 \leq |\eta| \leq 0.7$, which is consistent with previous analyses.[26, 62]

Since the vertex cut reduces the number of events in the sample, the luminosity was corrected based on the vertex distributions for the data sample before and after these cuts. Figure 19 shows there are 243,100 events before this cut and there are 227,400 events after this cut. Therefore, the integrated luminosity was reduced by the ratio 227400/243100 (0.94) to 3.9 pb^{-1}.

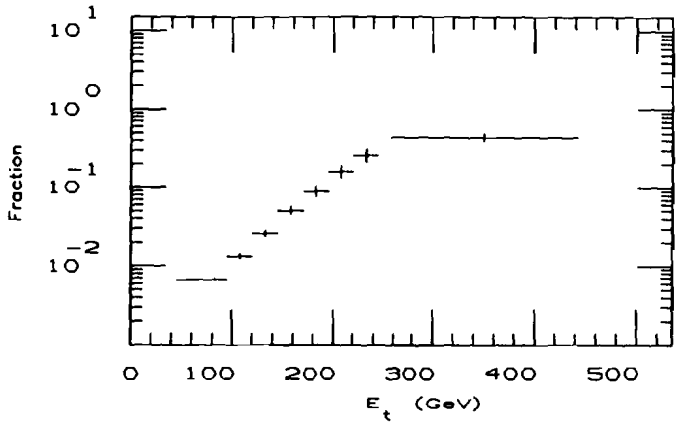

Figure 17. Fraction of jet backgrounds; Class 5, 6 and 11.

F. Measuring the Raw Cross Section

The raw jet cross section is the measured jet cross section which has not been corrected for the detector effects. The raw cross section was derived by collecting the jets in events passing the trigger, reconstruction, background, and fiducial cuts in 5 GeV bins (for each trigger).[63] Jets from events passing triggers that were pre-scaled were scaled appropriately. The average E_t was calculated for each bin and the number of entries in each bin was divided by the luminosity, bin size, and the pseudorapidity range (1.2). This gives a raw jet cross section which is not corrected for jet resolution smearing and detector effects.

The raw cross sections for each trigger can then be compared to determine, for each trigger, at what threshold the trigger becomes fully efficient. In the regions of

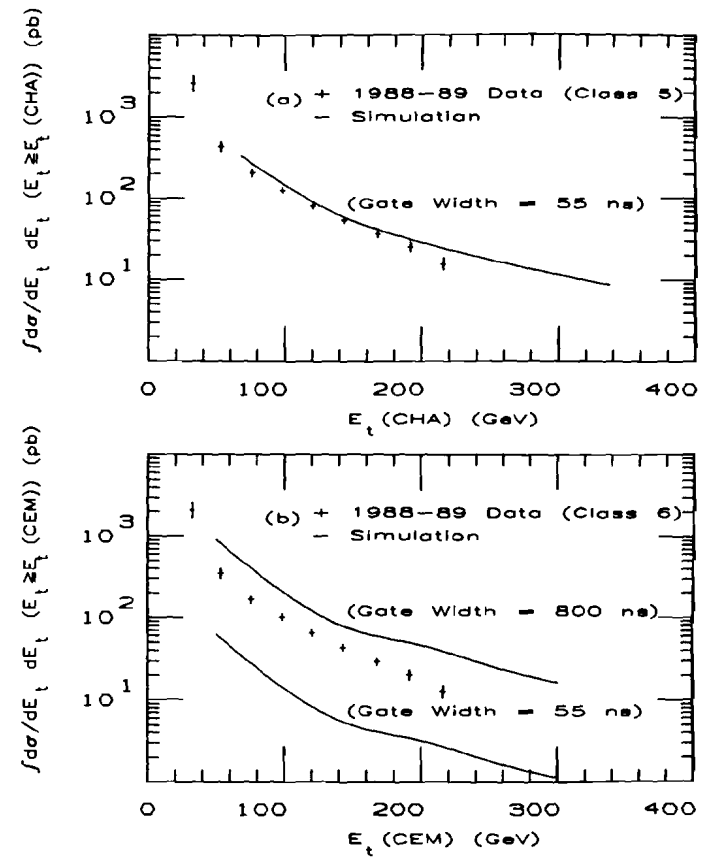

Figure 18. Expected cosmic ray event rates. Found in the a) CHA, and b) CEM.

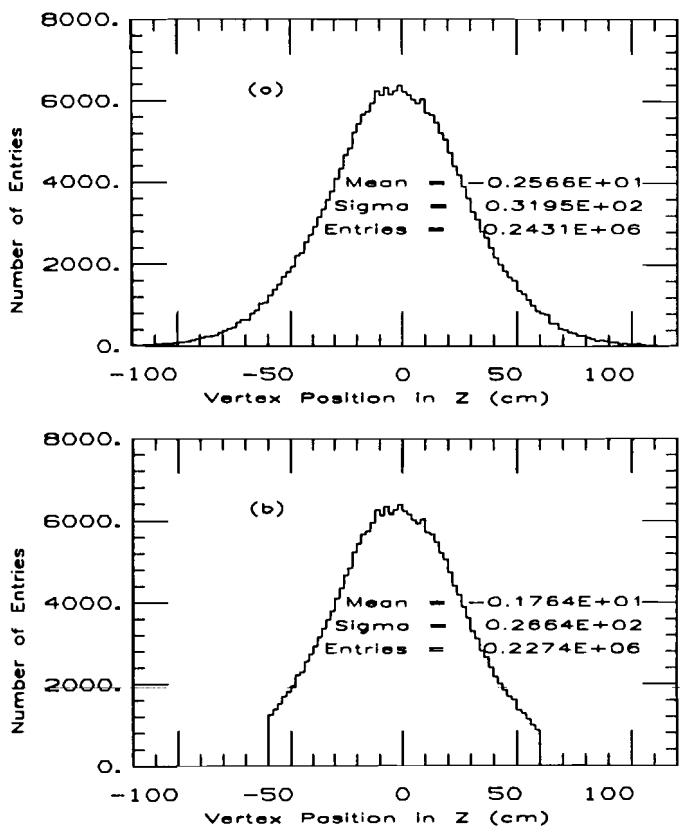

Figure 19. Event vertex distribution. Shown are the distributions found a) without and b) with the 60 *cm* vertex cut.

E_t where the different triggers overlap, cuts were studied to determined the range where the triggers were fully efficient. These cuts were determined both as a function of trigger threshold and as a function of cone size. Figure 20 shows the comparison of the raw jet cross section for a cone size of 0.7 for the various triggers. A special 15 GeV trigger was used to compare to the 20 GeV trigger. Table VII gives the effective cutoff threshold which was determined for each trigger as a function of cone size. This threshold is the point at which each trigger becomes fully efficient for each cone size.

The data below these thresholds were removed and the triggers combined to form the completed raw cross section. Bins which contained no events were merged with adjacent bins, and for bins containing fewer than 20 jets the statistical errors were determined using Poisson statistics.[64]

Using the procedures described in this chapter, the raw jet cross section has been measured for three cone sizes. The measured raw jet cross section for cone sizes of 0.4, 0.7, and 1.0 are listed in Tables VIII, IX, and X respectively. Also listed in these tables are the number of jets found in each bin scaled by the appropriate pre-scale and the statistical error associated with the raw jet cross section.

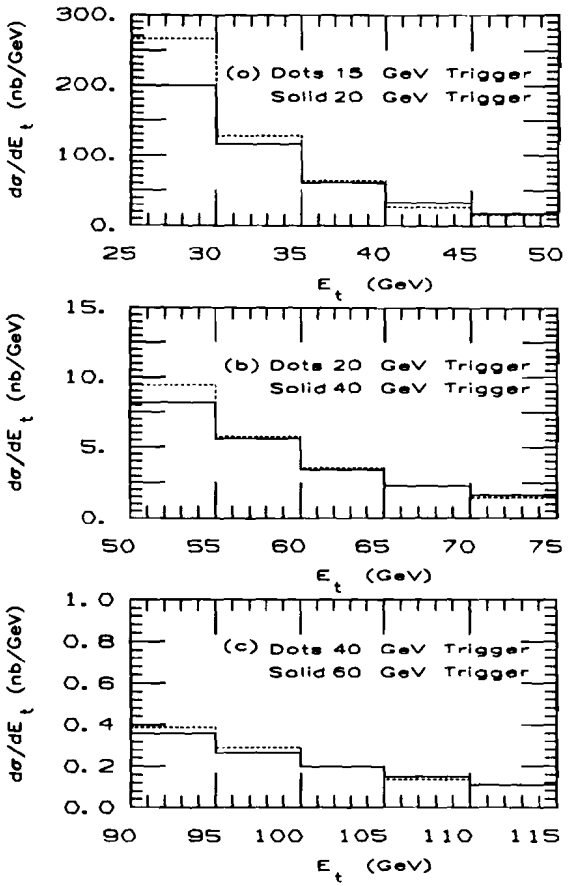

Figure 20. Comparisons of the raw trigger cross sections for jets with a cone size of 0.7. The following triggers have been compared: a) 15 GeV trigger compared to 20 GeV trigger, a) 20 GeV trigger compared to 40 GeV trigger, a) 40 GeV trigger compared to 60 GeV trigger.

Table VII. Efficiency thresholds for jet triggers as a function of cone size.

	Efficiency Threshold (GeV)		
Cone Size	20 GeV trigger	40 GeV trigger	60 GeV trigger
1.0	45	70	110
0.7	35	60	100
0.4	30	50	90

Table VIII. Raw jet cross section and related quantities for a jet clustering cone size of 0.4, number of jets has been scaled accordingly.

Bin Edges (GeV) Lower	Upper	Mean E_t (GeV)	Number of Jets	Raw Cross Section (nb/GeV)	Statistical Error (nb/GeV)
30	35	32.21	1775400	75.2	± 0.974
35	40	37.25	895500	37.9	± 0.692
40	45	42.28	447200	18.9	± 0.489
45	50	47.24	251700	10.7	± 0.367
50	55	52.29	151160	6.40	± 0.0874
55	60	57.33	93080	3.94	± 0.0687
60	65	62.30	57380	2.43	± 0.0540
65	70	67.41	38880	1.65	± 0.0444
70	75	72.42	26480	1.12	± 0.0366
75	80	77.31	17540	0.743	± 0.0299
80	85	82.37	12340	0.523	± 0.0252
85	90	87.32	9410	0.399	± 0.0218
90	95	92.37	6323	0.268	± 0.00337
95	100	97.36	4663	0.198	± 0.00289
100	105	102.32	3576	0.152	± 0.00253
105	110	107.31	2504	0.106	± 0.00212
110	115	112.50	1953	0.0827	± 0.00187
115	120	117.47	1472	0.0624	± 0.00163
120	125	122.43	1118	0.0474	± 0.00142
125	130	127.39	892	0.0378	± 0.00127
130	135	132.34	737	0.0312	± 0.00115
135	140	137.49	602	0.0255	± 0.00104
140	145	142.34	423	0.0179	± 0.000871

Table VIII. Continued

Bin Edges (GeV) Lower	Upper	Mean E_t (GeV)	Number of Jets	Raw Cross Section (nb/GeV)	Statistical Error (nb/GeV)
145	150	147.32	340	0.0144	± 0.000781
150	160	154.83	539	0.0114	± 0.000492
160	170	164.57	335	0.00710	± 0.000388
170	180	174.62	202	0.00428	± 0.000301
180	190	184.93	115	0.00244	± 0.000227
190	205	196.62	117	0.00165	± 0.000153
205	220	212.77	70	0.000989	± 0.000118
220	235	226.41	35	0.000494	± 0.0000836
235	250	243.51	28	0.000395	± 0.0000747
250	270	260.91	26	0.000275	± 0.0000540
270	290	281.68	8	0.0000847	$^{+0.0000419}_{-0.0000293}$
290	310	299.29	6	0.0000636	$^{+0.0000381}_{-0.0000253}$
310	330	319.53	3	0.0000318	$^{+0.0000310}_{-0.0000173}$
330	360	349.99	3	0.0000212	$^{+0.0000207}_{-0.0000115}$
360	405	385.92	2	0.00000942	$^{+0.0000125}_{-0.00000610}$

Table IX. Raw jet cross section and related quantities for a jet clustering cone size of 0.7, number of jets has been scaled accordingly.

Bin Edges (GeV) Lower	Upper	Mean E_t (GeV)	Number of Jets	Raw Cross Section (nb/GeV)	Statistical Error (nb/GeV)
35	40	37.25	1529200	64.8	± 0.904
40	45	42.20	800100	33.9	± 0.654
45	50	47.22	446800	18.9	± 0.489
50	55	52.33	236300	10.0	± 0.356
55	60	57.33	143500	6.08	± 0.277
60	65	62.30	87030	3.69	± 0.0664
65	70	67.31	57700	2.44	± 0.0541
70	75	72.33	41590	1.76	± 0.0459
75	80	77.31	27150	1.15	± 0.0370
80	85	82.36	18840	0.798	± 0.0310
85	90	87.30	13150	0.557	± 0.0259
90	95	92.31	9740	0.413	± 0.0223
95	100	97.36	7290	0.309	± 0.0192
100	105	102.39	4952	0.210	± 0.00298
105	110	107.36	3736	0.158	± 0.00259
110	115	112.37	2730	0.116	± 0.00221
115	120	117.41	2064	0.0874	± 0.00192
120	125	122.38	1581	0.0670	± 0.00168
125	130	127.35	1222	0.0518	± 0.00148
130	135	132.47	970	0.0411	± 0.00132
135	140	137.41	755	0.0320	± 0.00116
140	145	142.34	619	0.0262	± 0.00105
145	150	147.37	478	0.0203	± 0.000926

Table IX. Continued

Bin Edges (GeV) Lower	Upper	Mean E_t (GeV)	Number of Jets	Raw Cross Section (nb/GeV)	Statistical Error (nb/GeV)
150	160	154.62	711	0.0151	± 0.000565
160	170	164.42	475	0.0101	± 0.000462
170	180	174.70	280	0.00593	± 0.000354
180	190	184.64	156	0.00330	± 0.000265
190	205	196.34	161	0.00227	± 0.000179
205	220	211.73	98	0.00138	± 0.000140
220	235	226.08	56	0.000791	± 0.000106
235	250	243.19	29	0.000410	± 0.0000761
250	270	259.56	31	0.000328	± 0.0000590
270	290	278.95	16	0.000169	$^{+0.0000540}_{-0.0000421}$
290	310	298.70	7	0.0000741	$^{+0.0000400}_{-0.0000274}$
310	330	318.75	5	0.0000530	$^{+0.0000360}_{-0.0000229}$
330	360	353.57	3	0.0000212	$^{+0.0000207}_{-0.0000115}$
360	410	389.56	2	0.00000847	$^{+0.0000112}_{-0.00000549}$

Table X. Raw jet cross section and related quantities for a jet clustering cone size of 1.0, number of jets has been scaled accordingly.

Bin Edges (GeV) Lower	Upper	Mean E_t (GeV)	Number of Jets	Raw Cross Section (nb/GeV)	Statistical Error (nb/GeV)
45	50	47.30	712600	30.2	± 0.617
50	55	52.18	395500	16.8	± 0.460
55	60	57.30	238100	10.1	± 0.357
60	65	62.31	143100	6.06	± 0.276
65	70	67.51	97400	4.13	± 0.228
70	75	72.33	54790	2.32	± 0.0526
75	80	77.24	39550	1.68	± 0.0448
80	85	82.39	27000	1.14	± 0.0370
85	90	87.41	19280	0.817	± 0.0313
90	95	92.33	13190	0.559	± 0.0259
95	100	97.39	9830	0.416	± 0.0223
100	105	102.45	7090	0.300	± 0.0190
105	110	107.46	5170	0.219	± 0.0162
110	115	112.40	3826	0.162	± 0.00262
115	120	117.40	2815	0.119	± 0.00225
120	125	122.42	2177	0.0922	± 0.00198
125	130	127.37	1631	0.0691	± 0.00171
130	135	132.42	1254	0.0531	± 0.00150
135	140	137.39	1077	0.0456	± 0.00139
140	145	142.43	808	0.0342	± 0.00120
145	150	147.46	646	0.0274	± 0.00108
150	160	154.78	931	0.0197	± 0.000646
160	170	164.54	635	0.0135	± 0.000534

Table X. Continued

Bin Edges (GeV) Lower	Upper	Mean E_t (GeV)	Number of Jets	Raw Cross Section (nb/GeV)	Statistical Error (nb/GeV)
170	180	174.76	377	0.00799	± 0.000411
180	190	184.50	219	0.00464	± 0.000314
190	205	196.69	212	0.00299	± 0.000206
205	220	212.30	126	0.00178	± 0.000159
220	235	225.88	72	0.00102	± 0.000120
235	250	241.99	37	0.000523	± 0.0000859
250	270	258.34	41	0.000434	± 0.0000678
270	290	280.24	19	0.000201	$^{+0.0000577}_{-0.0000459}$
290	310	300.00	9	0.0000953	$^{+0.0000437}_{-0.0000312}$
310	330	320.63	4	0.0000424	$^{+0.0000337}_{-0.0000203}$
330	360	347.38	6	0.0000424	$^{+0.0000254}_{-0.0000168}$
360	410	393.87	4	0.0000169	$^{+0.0000135}_{-0.00000813}$

CHAPTER IV

JET CORRECTIONS

In order to compare the inclusive jet cross section to theory, the raw cross section needs to be corrected for several effects. Energy degradation due to calorimeter effects and resolution smearing combined with the effect of a falling spectrum causes the jet cross section to be mismeasured. In order to correct for these effects, a detailed detector simulation has been employed to ascertain the magnitude of these effects. In conjunction with this, an unsmearing procedure was developed to correct the raw cross section for these effects. In the sections which follow, these procedures will be discussed in detail.

A. Simulation

The jet E_t corrections used in previous CDF analyses were only calculated to 250 GeV. The 1988–1989 data set extends the cross section to 410 GeV in E_t; therefore, it was necessary to recalculate these corrections and extend their range of validity. The jet resolution can also be extracted from the simulation at the same time.

In order to extract both E_t corrections and resolution for jets in the CDF detector, a detector simulation was used to study the response of the detector to jets. A major ingredient of the jet E_t corrections and jet resolution is the non-linearity in the response of the detector to charged particles. Therefore, the simulation was tuned to reproduce the single pion response observed in the test beam and the jet

fragmentation observed in the data. In addition, the tracking efficiency in jets has been measured, parameterized, and introduced into the tracking simulation.

Much work has been done to tune the simulation to reproduce the results of the test beam.[65] The simulation has been tuned to reproduce the observed single pion response, as well as the non-linearity observed at lower pion energies in minimum bias data. An increase in the amount of data available, compared to the previous CDF collider run, has extended the momentum range covered in the tuning of the single pion response. This combined with a redefinition of the calorimeter energy associated with the projected track has led to a substantial reduction in the systematic uncertainty associated with the neutral pion (π^0) subtraction. It was therefore believed that if the simulation was tuned to reproduce the fragmentation observed in the data, the simulation would give the correct result for the jet E_t corrections and jet resolution.

A data set which consisted of approximately 4.2 pb^{-1} of jet data in the region above 120 GeV in E_t, and approximately 871 nb^{-1} of jet data in the region from 30–120 GeV, was used to study the fragmentation.

The simulation was performed using the following analysis routines: SIMJET, SETPRT, QFLANA, JETCLU, QTKEFF, CENJET, and JETFRG.

1. SIMJET generated jets. It created two partons in a falling spectrum defined to match the spectrum measured in the inclusive jet cross section. The generated jets were also required to have $\eta > 0.9$.
2. SETPRT fragmented the jets. This routine has five adjustable parameters which were used to tune the fragmentation. During this study it was necessary to

modify this routine to incorporate an E_t dependence into one of these five variables.

3. QFLANA simulated the detector response based on the CDF detector geometry using generated particles as input and returning information on the energy in the calorimeter towers and tracks observed in the tracking chamber. This information could then be used to cluster jets.[66]
4. JETCLU clustered the simulated jets using the same algorithm as was used for the data.
5. QTKEFF incorporated tracking efficiency into the simulation by flagging tracks as lost on the basis of a parameterization of tracking efficiency in jet events.
6. CENJET removed cosmic rays in the data and was therefore used on the simulation also.
7. JETFRG extracted and plotted the various fragmentation quantities examined in this study.

Since the simulation only supplied two partons, the data was required to be two jet events. This was done by requiring the following criteria from the events.

1. There must be at least two jets.
2. There must be no third jet with $E_t > 20$ GeV.
3. The highest E_t jet and the second highest E_t jet must be separated by at least 150 degrees in azimuthal angle (ϕ).
4. The Z vertex was required to be within 60 cm of the center of the detector.
5. At least one jet was required to be in the central detector, $0.1 \leq |\eta| \leq 0.7$.

The jets were clustered with a cone size of 0.7 and tracks were required to be within the cone of the jet and to have $P_t \geq 500$ MeV/c. It should be noted that these same cuts were applied to both the simulation and the data.

The fragmentation distributions observed in the data also includes the effects of tracking efficiency in jets. It is therefore necessary to measure the tracking efficiency in jets and apply this in the simulation. This work was done by B. Winer and P. Tipton and was incorporated into QTKEFF.[67]

In order to compare the data and simulation, the following quantities were used to tune the fragmentation:

1. The fragmentation distribution (Z) defined in the following ways:

$$Z(P) = P_{//}(Track)/P(Jet), \tag{17}$$

$$Z(E) = P_{//}(Track)/E(Jet), \tag{18}$$

$$Z(T) = P_{//}(Track)/\sum_{in\ cone}(P(Track)), \tag{19}$$

$P_{//}$ is the momentum of the track parallel to the jet axis. Each Z was plotted as $(1/N_{jets})(dN/dZ)$.

2. The number of tracks in the cone of the jet (Jet Multiplicity) was plotted as $(1/N_{jets})(Mult)$.
3. The number of tracks in the cone 90 degrees away in ϕ from the jet (Underlying Event Multiplicity) was plotted as $(1/N_{jets})(Mult_{Und})$.
4. The momentum perpendicular to the jet axis of tracks in the cone of the jet was plotted as $(1/N_{jets})(dN/dP_{\perp})$, where $P_{\perp}$ is the momentum of the track perpendicular to the jet axis.

5. For the tracks in a cone 90 degrees away in ϕ from the jet, the momentum perpendicular to the axis of this cone was plotted as $(1/N_{jets})(dN/dP_{\perp\ Und})$.
6. The P_t (relative to the beam axis) of the tracks in the cone around the jet was plotted as $(1/N_{jets})(dN/dP_t)$.
7. The P_t of the tracks in the cone 90 degrees away from the jet was plotted as $(1/N_{jets})(dN/dP_{t\ Und})$.
8. The P_t flow of the tracks with respect to the lead jet in ϕ, which is the $\Delta\phi$ of the track with respect to the lead jet weighted by the P_t of the track.
9. The P_t loss flow of the tracks with respect to the lead jet in ϕ, which is the $\Delta\phi$ of the track with respect to the lead jet weighted by the amount P_t(loss) by the track due to the non-linearity.
10. The amount of energy loss in the jet due to the non-linearity in the central hadron calorimeter.

All of these variables were plotted as a function of jet E_t for tuning any possible fragmentation evolution.

SETPRT contains five variables which can be used to tune the fragmentation of jets. These variables are labeled in SETPRT as follows: $XGEN(1)$, $XGEN(2)$, $SIGQT$, $SIGQT0$, and $CON2$. $XGEN(1)$ and $XGEN(2)$ are used to describe the Field Feynman fragmentation parameterization[68] for jets in SETPRT (see Equation 20). The Field Feynman fragmentation is parameterized by,

$$F(Z) = 1 - XGEN(1) + XGEN(1) \times (XGEN(2) + 1) \times (1 - Z)^{XGEN(2)}, \quad (20)$$

where $XGEN(1)$ essentially controls the normalization and $XGEN(2)$ controls the slope of the fragmentation distribution. The fragmentation routine (SETPRT) does not include the effects of gluon radiation which distorts the fragmentation, therefore the transverse fragmentation needed to be tuned in order to match the data.[69] $SIGQT0$ is used to define the transverse P_t of the tracks in the underlying event and $SIGQT$ is used to define the transverse P_t of the tracks in the jets as shown by the parameter SIG in Equation 21. CON2 represents the transverse fragmentation power as described by Equation 21.

$$P_t = N * SIG * \sqrt{R^{-1/CON2} - 1}, \quad (21)$$

defines the $P_\perp$ distribution of the tracks in the event where SIG modifies the normalization N for the jet or underlying event and $CON2$ controls the slope for the distribution. The default values of these variables are listed in Table XI, along with the final tuned values. These five variables were tuned until there was agreement between the data and simulation for the plots listed above. This implies that the means, sigmas and shapes of each plot in the simulation was in agreement with the data. The simulation was tuned for jets with low E_t ranging from 30-60 GeV and also for jets with high E_t ranging from 120-150 GeV.

After examining the simulation at higher E_t's in comparison with the data, it was necessary to make SIGQT a function of jet E_t. Knowing both the high (120-150 GeV) and low (30-60 GeV) E_t tunes, SETPRT was then modified to scale SIGQT with jet E_t. These low and high values are also listed in Table XI.

Table XI. Values of the tuned parameters in SETPRT. Including the values of the default parameters and both low (30-60 GeV) and high (120-150 GeV) tune values for the unmodified version of SETPRT.

Variable	Default Value	Low Value	High Value	Final Tune
XGEN(1)	0.950	0.950	0.950	0.950
XGEN(2)	7.000	7.500	7.500	7.500
SIGQT	0.275	0.275	0.600	0.250
SIGQT0	0.370	0.370	0.370	0.370
CON2	1.100	1.200	1.200	1.200

With the final modifications to SETPRT, the fragmentation was tuned in SETPRT to agree with what was observed in the CDF jet data over the full range of jet E_t's. In order to check the fragmentation at low E_t, an unbiased data sample was needed. This was obtained by using the jets in the photon data sample which had a lower trigger threshold. The results of the fragmentation observed in jets ranging from 10-20 GeV in the photon data sample were then compared to the simulation. As can be seen in Figures 21, 22, 23, and 24, the various fragmentation plots in both simulation and data agree at both low and high E_t.

The jet fragmentation was also tuned to model the non-linearity of the hadronic calorimeter since the main source of energy loss in jets are low energy particles. Figure 25 shows the percent of energy loss due to the non-linearity in the central hadronic calorimeter for both the data and simulation. This energy loss in the simulation and the data agree at the level of 1-3%. This agreement combined with the tuning of

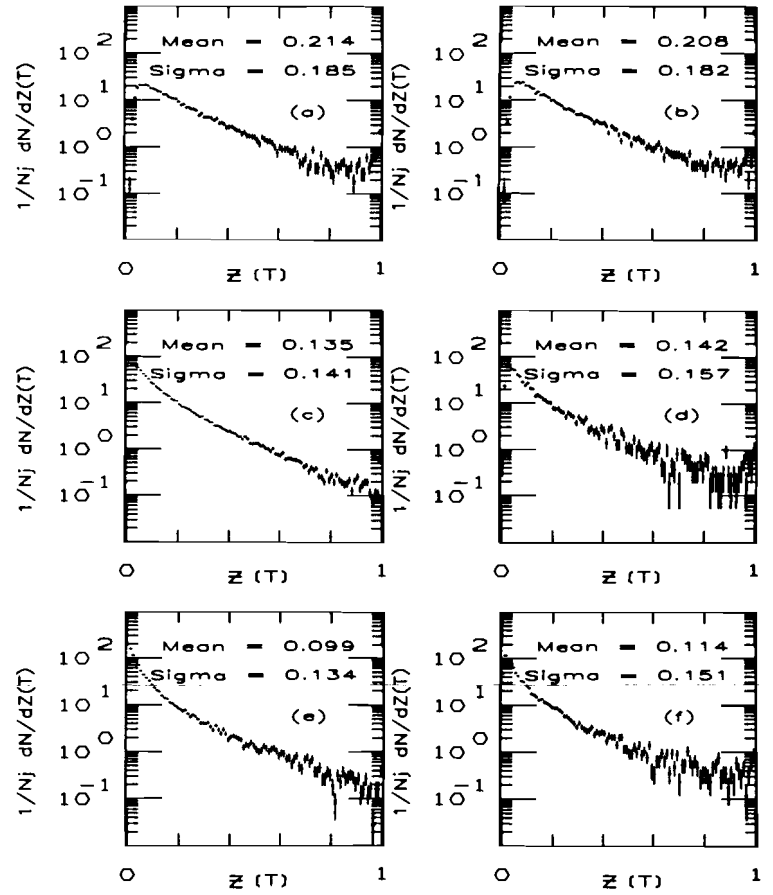

Figure 21. The distribution of $Z(T)$ in jets with a cone size of 0.7 as defined in Equation 19. Shown are the a) data and b) simulation in the E_t range 10-20 GeV, c) data and d) simulation in the E_t range 30-60 GeV, e) data and f) simulation in the E_t range 120-150 GeV.

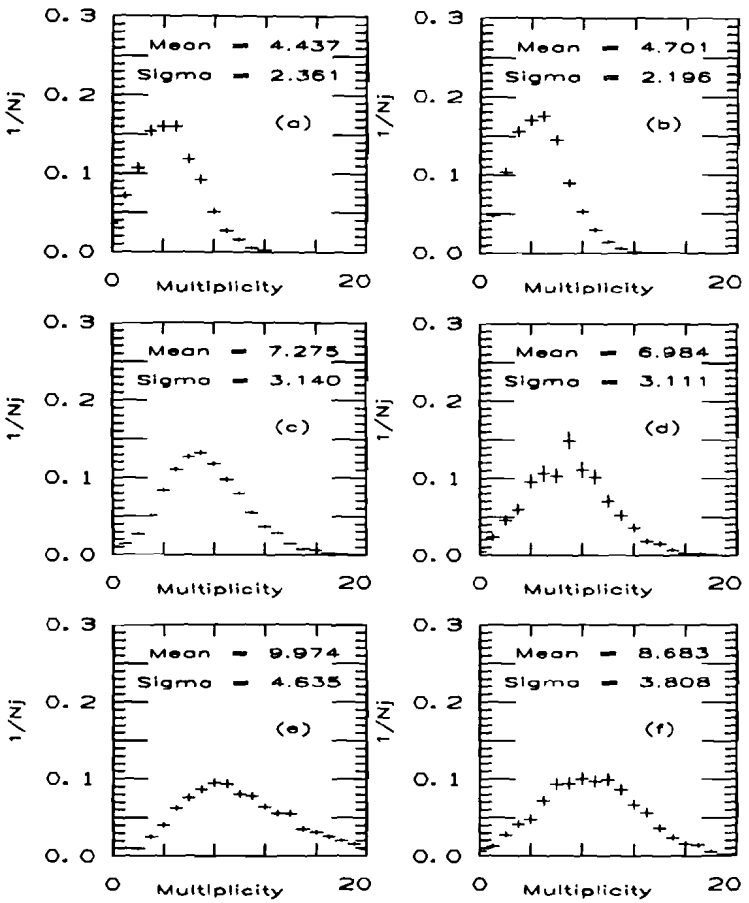

Figure 22. The jet track multiplicity in jets with a cone size of 0.7. Shown are the a) data and b) simulation in the E_t range 10-20 GeV, c) data and d) simulation in the E_t range 30-60 GeV, e) data and f) simulation in the E_t range 120-150 GeV.

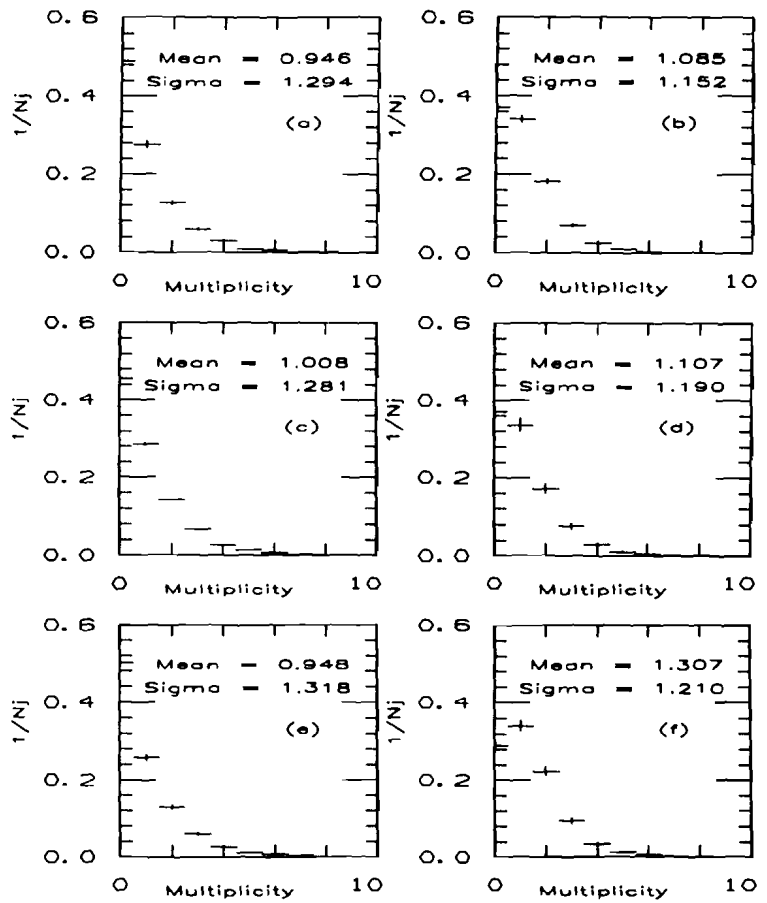

Figure 23. The underlying event track multiplicity in jets with a cone size of 0.7. Shown are the a) data and b) simulation in the E_t range 10-20 GeV, c) data and d) simulation in the E_t range 30-60 GeV, e) data and f) simulation in the E_t range 120-150 GeV.

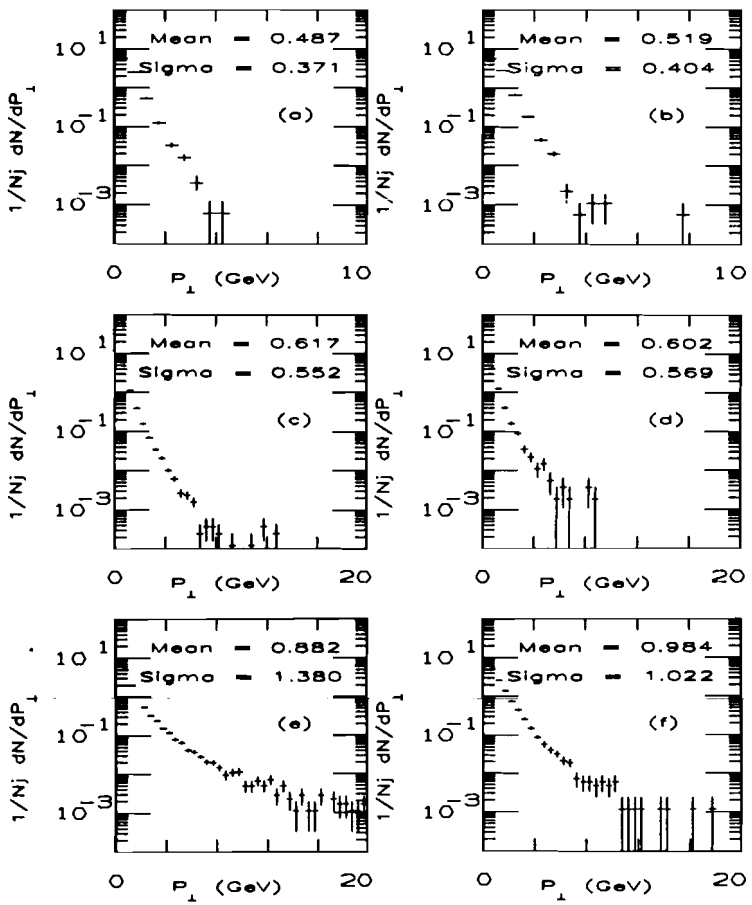

Figure 24. The distribution of $P_\perp$ in jets with a cone size of 0.7. Shown are the a) data and b) simulation in the E_t range 10-20 GeV, c) data and d) simulation in the E_t range 30-60 GeV, e) data and f) simulation in the E_t range 120-150 GeV.

the single pion response, shows both jet E_t corrections and jet resolution can be accurately extracted from the simulation out to 450 GeV in E_t.

B. Jet E_t and Resolution

In this section the procedure used to obtain the corrected inclusive jet E_t cross section from the measured spectrum is described. In order to have a well defined method for accounting for the effects of both jet resolution and E_t degradation, the E_t corrections and jet resolution have been combined into a single unsmearing procedure.[70]

In order to measure the inclusive jet cross section, the data was first placed in bins of measured (uncorrected) E_t. A given jet of true transverse energy (E_t^{true}) may contribute to a bin of measured E_t (E_t^{meas}) because of energy degradation or calorimeter measurement error (resolution). Therefore, the E_t and resolution corrections to the observed jet cross section are coupled and corrections to the cross section must account for this coupling. Traditionally, jet E_t corrections (obtained through detector simulation) have been based on the relationship between the true jet E_t and the average E_t^{meas} associated with that true jet; this is an inappropriate correction to apply when jet resolution effects contribute substantially to E_t^{meas}. Therefore, E_t and resolution effects have been combined in the unsmearing of the inclusive jet cross section.

In order to begin the process of unsmearing the cross section, the jet response function for all values of E_t^{true}, namely the set of measured jet E_t distributions associated with each E_t^{true}, were obtained. These response functions, which reflect both

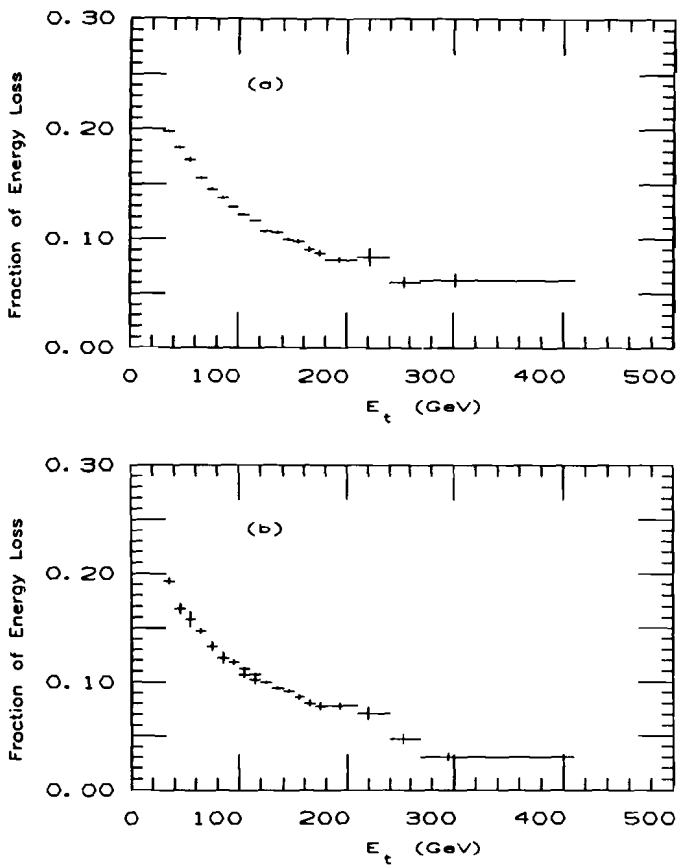

Figure 25. Fraction of energy loss in jets with a cone size of 0.7, due to hadronic non-linearity. This energy loss is plotted for both the a) data and b) simulation.

degradation and resolution, were found using a detector simulation tuned to reproduce single-particle calorimeter response[65] and jet fragmentation properties as discussed earlier. Dijet events with a flat E_t^{true} spectrum were generated without k_t smearing (which is a smearing of the momentum balance in two jet events). k_t smearing was not used since this is sensitive to QCD effects of both soft and hard gluon emission and detector effects, and the corrections for detector effects needed to be isolated. The events were generated in the E_t interval of 0-900 GeV, and a scatterplot of E_t^{meas} vs E_t^{true} was made. (Jets were also required to impact the calorimeter in the detector-η interval $0.1 < |\eta_d| < 0.7$, the same requirement was made for the data.) E_t^{true} was defined to be the sum of all generated particles which point into the measured jet clustering cone associated with the reconstructed jet. Only particles coming from the parton closest in η and ϕ were considered in the sum, and no correction was made for energy lost outside the cone. This was done in order to be able to compare the final cross section to next-to-leading order QCD calculations where a correction for energy lost outside the clustering cone is no longer valid.[21]

Using this scatterplot, distributions of E_t^{meas} were extracted for various values of E_t^{true}. These distributions were parameterized as an exponential smeared by a Gaussian: parameters in the fits were (1) the average of the E_t^{meas} distribution (*Mean*), (2) the decay constant of the exponential (*Slope*), and (3) the standard deviation of the Gaussian (*Sigma*). Typical fits of this parameterization for a measured jet cone size of 0.4, 0.7, and 1.0 evaluated at $E_t^{true} = 20, 50$, and 200 GeV can be seen in Figure 26. The *Mean*, *Slope*, and *Sigma* were then parameterized as a function

of E_t^{true}, thus defining the jet response functions for an E_t range from 0 900 GeV. The response functions predicted from detector simulation were found to have upward going non-Gaussain tails for E_t^{true}'s below about 50 GeV, were nearly Gaussian in the interval 50–80 GeV, and developed downward going non-Gaussain tails above about 80 GeV. These tails in the distributions are associated with the effect of the non-linearity for low energy pions in the hadron calorimeter.

Jet response functions were measured for cone sizes of 0.4, 0.7, and 1.0; the following parameterizations were then used for $Mean$, $Sigma$, and $Slope$;

$$Mean = AE_t^3 + BE_t^{1/3} + CE_t^2 + DE_t^{1/2} + EE_t + F, \tag{22}$$

$$Sigma = W(E_t + X)^Y + Z, \tag{23}$$

$$Slope = ME_t + N \text{ (for } E_t < CUTOFF),$$

$$Slope = QE_t + R \text{ (for } E_t \geq CUTOFF), \tag{24}$$

where E_t is E_t^{true}. The values for the parameters in the parameterization of the $Mean$ are listed in Table XII. The values of the parameters in the parameterization of $Sigma$ are listed in Table XIII and the values of the parameters in the parameterization of $Slope$ are listed in Table XIV.

The contribution of the cluster-finding efficiency to the response functions has also been considered. The cluster-finder efficiency can be included in the response functions, $R(E_t^{true}, E_t^{meas})$, by scaling them by this efficiency. If $Eff(E_t^{true})$ is the fraction of time that a true jet of E_t^{true} leaves no cluster, the new response function is redefined as $R(E_t^{true}, E_t^{meas}) = |1 - Eff(E_t^{true})| \times R(E_t^{true}, E_t^{meas})$. The results from photon-jet balancing studies [71] were used to determine the size of Eff.

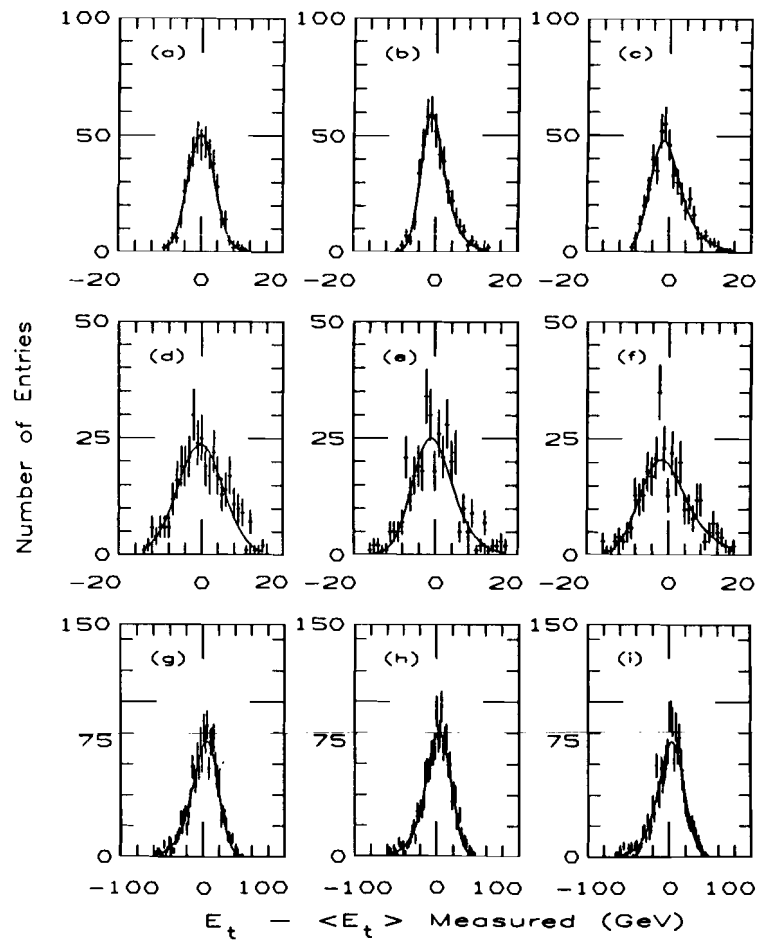

Figure 26. The simulated response of the detector at several E_t's for jets. The response is shown for the following cone sizes and energies: a) cone size of 0.4, b) cone size of 0.7, and c) cone size of 1.0 with true E_t of 20 GeV; d) cone size of 0.4, e) cone size of 0.7, and f) cone size of 1.0 with true E_t of 50 GeV; g) cone size of 0.4, h) cone size of 0.7, and i) cone size of 1.0 with true E_t of 200 GeV.

Table XII. The values of the parameters obtained for the parameterization of the *Mean*, for each cone size.

Variable	Cone Size 0.4	Cone Size 0.7	Cone Size 1.0
A	1.139×10^{-7}	7.979×10^{-8}	4.679×10^{-8}
B	-0.358	-3.826×10^{-2}	-0.299
C	-1.561×10^{-4}	-1.089×10^{-4}	-6.288×10^{-5}
D	-1.691	-2.070	-1.830
E	1.023	1.005	0.978
F	3.485	4.868	6.080

Table XIII. The values of the parameters obtained for the parameterization of the *Sigma*, for each cone size.

Variable	Cone Size 0.4	Cone Size 0.7	Cone Size 1.0
W	1.350	2.012	3.186
X	2.297	16.465	13.082
Y	0.453	0.409	0.353
Z	-2.668	-6.306	-8.316

With response functions in hand, the jet E_t and resolution corrections for measured jet cross section can be evaluated. Overall, the procedure is conceptually like a monte carlo simulation which would start with a true E_t spectrum for jets, pass the jets through the detector simulation and clustering routine and eventually yield a measured spectrum. The actual procedure was a quick version of the above which

Table XIV. The values of the parameters obtained for the parameterization of the *Slope*, for each cone size.

Variable	Cone Size 0.4	Cone Size 0.7	Cone Size 1.0
M	0.0329	0.0403	0.00642
N	1.187	1.171	3.621
$CUTOFF$	40 GeV	48 GeV	70 GeV
Q	-0.0855	-0.0935	-0.0823
R	2.118	5.187	3.525

uses the parameterized response functions rather than actually throwing events. A tunable function was used for the true spectrum and this function was tuned until the χ^2/dof between the smeared spectrum calculated by the program and the measured data spectrum was minimized. Figure 27 illustrates how this unsmearing procedure works.

The procedure started with a parameterized curve that represents the true (but unknown) inclusive jet cross section. For this study the following parameterization was found to be capable of describing the cross section:

$$P(E_t^{true}) = A((E_t^{true})^{-M}(1 - x_t + Cx_t^2)^N), \tag{25}$$

$$x_t = 2E_t^{true}/1800, \tag{26}$$

where M, C, and N are the tunable parameters. (A, the normalization, was obtained by requiring that the area of the smeared distribution from the parameterized curve equal the area in the data.) This parameterization was found to fit both standard

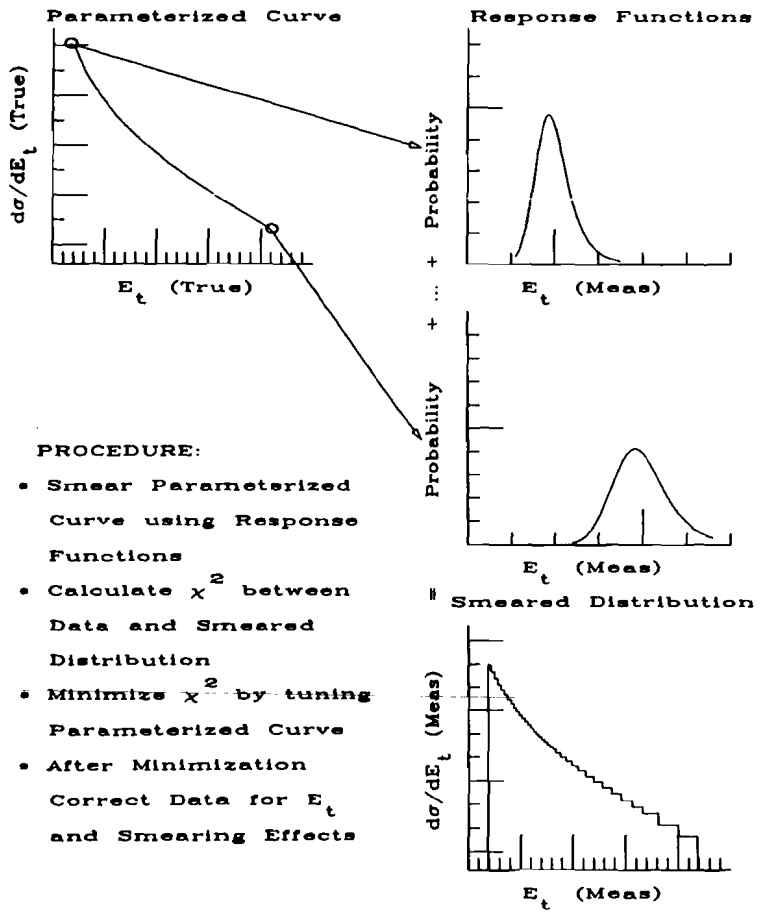

Figure 27. An illustration of the unsmearing procedure.

QCD and a range of compositeness curves very well. In addition, this functional form yielded a smeared distribution which agreed well with the data.

This parameterized curve was then smeared and degraded using the simulation-derived response functions and the resulting smeared distribution was collected into the same size bins that were used for the data spectrum; in this way, effects of bin-integration were included in the comparison with the binned data. For a given measured bin in the data where the low edge of the bin is *low* and the high edge is *high*, the following convolution was performed to obtain a smeared distribution for this bin:

$$\frac{d\sigma(E_{t,bin}^{meas})}{dE_t^{meas}} = \frac{\int_{low}^{high} dE_t^{meas} \int_0^{\sqrt{s}/2} dE_t^{true} R(E_t^{true}, E_t^{meas}) P(E_t^{true})}{high - low}, \qquad (27)$$

where $P(E_t^{true})$ is the value of the parameterized curve evaluated at E_t^{true} and the response function $R(E_t^{true}, E_t^{meas})$ represents the probability that a true jet at E_t^{true} would contribute to the measured spectrum at E_t^{meas}. $E_{t,bin}^{meas}$ is the calculated average value of E_t^{meas} for each bin. This integration was done from 0-$\sqrt{s}/2$ (where $\sqrt{s}$ is defined to be the center of mass energy) since this covered the range of possible jet E_t's expected to be observed. This convolution was performed for every bin used in the analysis, thus a smeared-and-binned distribution from the parameterized curve was derived.

Next, a sum of the bin-by-bin χ^2's between the data and smeared distribution was calculated using the statistical errors from the data. The procedure was then iterated modifying M, C, and N until the χ^2/dof was minimized. In Figure 28 the results of the unsmearing procedure (a comparison of smeared and true spectra and

the bin-by-bin residuals between the smeared distribution and the measured data) for cone sizes of 0.4, 0.7, and 1.0 are plotted. The values obtained for M, C, N, and A are given in Table XV along with the χ^2/dof.

Having found the best fit for the parameterized curve which when smeared agreed with the data, the data points must be moved onto this parameterized curve. In order to do this, the following variables were defined for every bin in the data:

$$E_{t,bin}^{meas} = \frac{\int_{low}^{high} dE_t^{meas} \int_0^{\sqrt{s}/2} dE_t^{true} E_t^{meas} R(E_t^{true}, E_t^{meas}) P(E_t^{true})}{\int_{low}^{high} dE_t^{meas} \int_0^{\sqrt{s}/2} dE_t^{true} R(E_t^{true}, E_t^{meas}) P(E_t^{true})}, \tag{28}$$

and

$$E_{t,bin}^{true} = \frac{\int_{low}^{high} dE_t^{meas} \int_0^{\sqrt{s}/2} dE_t^{true} E_t^{true} R(E_t^{true}, E_t^{meas}) P(E_t^{true})}{\int_{low}^{high} dE_t^{meas} \int_0^{\sqrt{s}/2} dE_t^{true} R(E_t^{true}, E_t^{meas}) P(E_t^{true})}, \tag{29}$$

$E_{t,bin}^{true}$ is the calculated average value of E_t^{true} that the smearing procedure predicts for each bin (this value results from both resolution and energy degradation). The energy corrections to the data-points was defined in such a way that the average measured E_t of a given bin was scaled up to the average true E_t contributing to that bin:

$$E_{t,bin} = \frac{E_{t,bin}^{true}}{E_{t,bin}^{meas}} E_{t,bin}^{data}, \tag{30}$$

After correcting the E_t for the bin (using $E_{t,bin}^{true}$ and $E_{t,bin}^{meas}$), any residual correction was performed by a scaling of cross section using the ratio of the value of the parameterized curve evaluated at $E_{t,bin}^{true}$ and the value of the smeared distribution associated with this bin at $E_{t,bin}^{meas}$:

$$CS_{bin} = CS_{bin}^{data} \left(\frac{d\sigma(E_{t,bin}^{true})}{dE_t^{true}}\right) / \left(\frac{d\sigma(E_{t,bin}^{meas})}{dE_t^{meas}}\right), \tag{31}$$

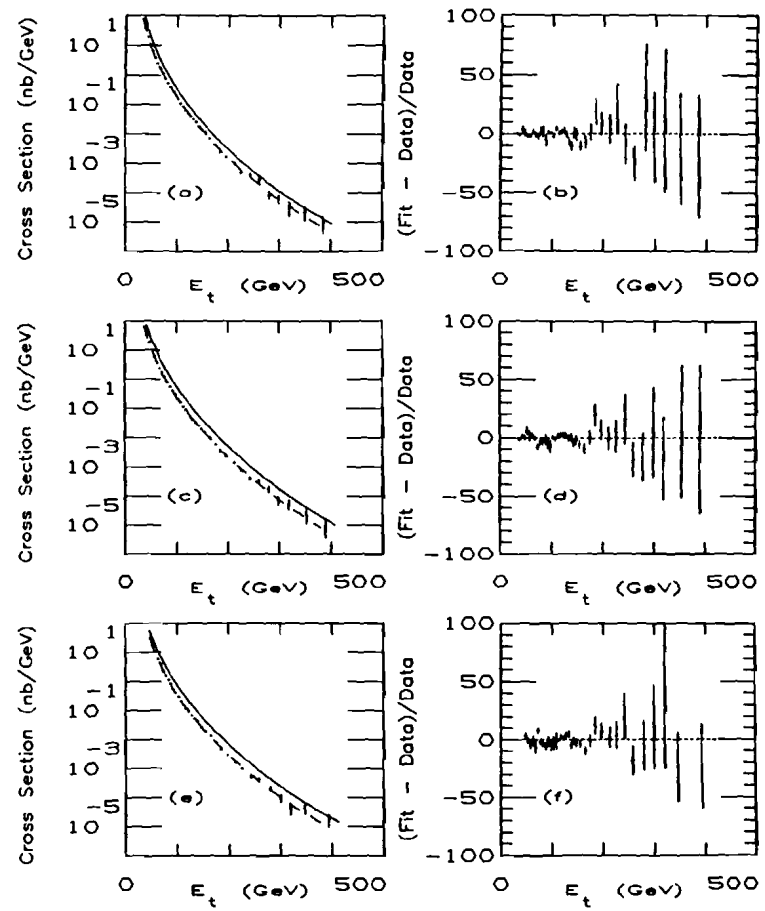

Figure 28. Unsmearing plots for cross sections of the various cone sizes. The solid line represents the unsmeared parameterized curve and the dashed line represents the smeared parameterized curve. Plotted are the a) fits and b) residuals for cone size of 0.4, c) fits and d) residuals for cone size of 0.7, e) fits and f) residuals for cone size of 1.0.

Table XV. Fits to parameterized curve used in unsmearing procedure.

Parameter	Cone Size 0.4	Cone Size 0.7	Cone Size 1.0
A	0.11307×10^{10}	0.22106×10^{10}	0.12370×10^{10}
M	4.405	4.431	4.195
C	0.632	0.578	0.683
N	15.867	15.772	18.102
χ^2/dof	1.303	1.220	1.579

Thus, $E_{t,bin}$ and CS_{bin} are the corrected E_t and cross section for each bin in the inclusive jet cross section. Figure 29 shows the measured data and the corrected data (for a cone size of 0.7). As shown, the E_t corrections move the data horizontally in this plot and the smearing corrections move the data vertically.

This procedure has been applied to the 1988-1989 CDF jet data set for cone sizes of 0.4, 0.7, and 1.0. The corrections obtained for cone sizes of 0.4, 0.7 and 1.0 are listed in Tables XVI, XVII, and XVIII respectively. The results were found to be consistent with results from the 1987 CDF inclusive jet measurement: Figure 30 shows the cross section calculated using the data collected by CDF in their 1987 data run (for a cone size of 0.6) together with the cross section calculated here using the CDF 1988-1989 data set (with a cone size of 0.7). Agreement is expected only within systematic uncertainty since the assumptions about jet resolution have evolved since 1987; in addition, a correction for energy loss outside the clustering cone was applied in the 1987 analysis, unlike the current analysis.

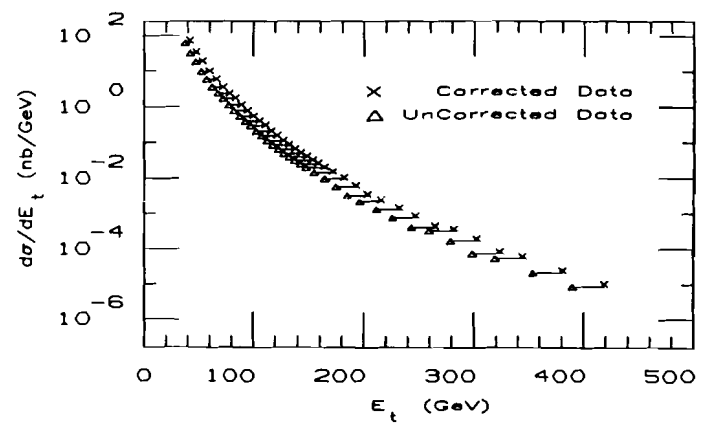

Figure 29. Unsmeared and corrected cross section for jets with a cone size of 0.7, the lines indicate direction of corrections.

The E_t corrections extracted from the current detector simulation are also consistent with the E_t corrections from the 1987 analysis. Figure 31 shows the magnitude and direction of the E_t corrections from the 1987 result[72] for a cone size of 0.6 where the energy out of the cone corrections were removed, plotted along side the result arrived at using SETPRT for a cone of 0.7.

Dijet balancing techniques, described in Appendix A, were first introduced by the UA2 collaboration[73, 74] and have been used extensively in jet measurements at CDF.[75, 76] Using these techniques, the jet resolution extracted from the simulation was found to be consistent with what was observed in the data. Figure 32 shows $\sigma'/\sqrt{2}$ vs E_t for jets with a cone size of 0.7 in the data compared to the simulation where

Table XVI. Corrections to the raw jet cross section and related quantities for a jet clustering cone size of 0.4.

Mean	Smearing Corrections			
E_t (GeV)	Lower Edge	Upper Edge	Mean E_t	Cross Section
32.21	1.124	1.126	1.125	1.156
37.25	1.126	1.123	1.125	1.109
42.28	1.123	1.126	1.124	1.103
47.24	1.126	1.129	1.128	1.097
52.29	1.129	1.127	1.129	1.086
57.33	1.127	1.123	1.126	1.083
62.30	1.123	1.119	1.121	1.084
67.41	1.119	1.115	1.117	1.086
72.42	1.115	1.111	1.113	1.088
77.31	1.111	1.108	1.110	1.090
82.37	1.108	1.105	1.106	1.093
87.32	1.105	1.102	1.103	1.095
92.37	1.102	1.099	1.100	1.097
97.36	1.099	1.097	1.098	1.100
102.32	1.097	1.094	1.095	1.102
107.31	1.094	1.092	1.093	1.104
112.50	1.092	1.090	1.091	1.106
117.47	1.090	1.088	1.089	1.108
122.43	1.088	1.086	1.087	1.110
127.39	1.086	1.085	1.086	1.112
132.34	1.085	1.083	1.084	1.114
137.49	1.083	1.082	1.083	1.116
142.34	1.082	1.080	1.081	1.118

Table XVI. Continued

Mean	Smearing Corrections			
E_t (GeV)	Lower Edge	Upper Edge	Mean E_t	Cross Section
147.32	1.080	1.079	1.080	1.120
154.83	1.079	1.077	1.078	1.129
164.57	1.077	1.075	1.076	1.132
174.62	1.075	1.073	1.074	1.134
184.93	1.073	1.071	1.072	1.137
196.62	1.071	1.069	1.070	1.148
212.77	1.069	1.067	1.068	1.150
226.41	1.067	1.065	1.066	1.152
243.51	1.065	1.064	1.065	1.154
260.91	1.064	1.063	1.063	1.163
281.68	1.063	1.062	1.062	1.162
299.29	1.062	1.061	1.061	1.160
319.53	1.061	1.060	1.061	1.157
349.99	1.060	1.060	1.060	1.166
385.92	1.060	1.061	1.060	1.175

$\sigma' = (\sigma^2_{k_{t_\parallel}} - \sigma^2_{k_{t_\perp}})^{1/2}$ also plotted is what the parameterization of the response function (for a cone of 0.7) predicts for the single jet resolution ($\sigma_{rms} = (Slope^2 + Sigma^2)^{1/2}$). A quantitative evaluation of the level of agreement for the jet resolution and E_t corrections will be discussed in the next chapter.

This method is an improvement over the previous methods used for correcting the inclusive jet cross section for two reasons.[77] First, the old scheme for corrections

Table XVII. Corrections to the raw jet cross section and related quantities for a jet clustering cone size of 0.7.

Mean	Smearing Corrections			
E_t (GeV)	Lower Edge	Upper Edge	Mean E_t	Cross Section
37.25	1.110	1.125	1.118	1.194
42.20	1.125	1.131	1.128	1.094
47.22	1.131	1.140	1.134	1.063
52.33	1.140	1.152	1.145	1.048
57.33	1.152	1.159	1.155	1.030
62.30	1.159	1.161	1.160	1.022
67.31	1.161	1.160	1.161	1.017
72.33	1.160	1.157	1.159	1.017
77.31	1.157	1.153	1.155	1.020
82.36	1.153	1.149	1.151	1.025
87.30	1.149	1.146	1.148	1.030
92.31	1.146	1.142	1.144	1.035
97.36	1.142	1.139	1.141	1.040
102.39	1.139	1.136	1.137	1.045
107.36	1.136	1.133	1.134	1.050
112.37	1.133	1.130	1.131	1.054
117.41	1.130	1.127	1.128	1.059
122.38	1.127	1.124	1.126	1.063
127.35	1.124	1.122	1.123	1.067
132.47	1.122	1.120	1.121	1.071
137.41	1.120	1.118	1.119	1.075
142.34	1.118	1.115	1.117	1.079
147.37	1.115	1.113	1.114	1.083

Table XVII. Continued

Mean	Smearing Corrections			
E_t (GeV)	Lower Edge	Upper Edge	Mean E_t	Cross Section
154.62	1.113	1.110	1.112	1.094
164.42	1.110	1.106	1.108	1.101
174.70	1.106	1.103	1.105	1.107
184.64	1.103	1.101	1.102	1.113
196.34	1.101	1.097	1.099	1.127
211.73	1.097	1.093	1.095	1.135
226.08	1.093	1.090	1.092	1.141
243.19	1.090	1.088	1.089	1.147
259.56	1.088	1.085	1.086	1.161
278.95	1.085	1.082	1.083	1.166
298.70	1.082	1.080	1.081	1.170
318.75	1.080	1.078	1.079	1.172
353.57	1.078	1.076	1.077	1.189
389.56	1.076	1.073	1.074	1.224

did not account for bin-integration effects having to do with the size of the bin used, whereas the new procedure does. The second improvement is conceptual: the actual detector response to jets is now modeled by combining the resolution effects with the E_t corrections, whereas before the E_t corrections where handled separately from the resolution. The reason this is more indicative of the actual physics processes involved in measuring the data is that physically a jet of E_t^{true} is not always measured as a

Table XVIII. Corrections to the raw jet cross section and related quantities for a jet clustering cone size of 1.0.

Mean	Smearing Corrections			
E_t (GeV)	Lower Edge	Upper Edge	Mean E_t	Cross Section
47.30	0.932	1.006	0.968	1.847
52.18	1.006	1.055	1.030	1.492
57.30	1.055	1.084	1.070	1.294
62.31	1.084	1.100	1.093	1.169
67.51	1.100	1.108	1.104	1.111
72.33	1.108	1.116	1.112	1.096
77.24	1.116	1.124	1.120	1.088
82.39	1.124	1.128	1.126	1.076
87.41	1.128	1.130	1.129	1.067
92.33	1.130	1.129	1.130	1.063
97.39	1.129	1.128	1.129	1.063
102.45	1.128	1.126	1.127	1.065
107.46	1.126	1.124	1.125	1.068
112.40	1.124	1.122	1.123	1.072
117.40	1.122	1.120	1.121	1.075
122.42	1.120	1.119	1.119	1.078
127.37	1.119	1.117	1.118	1.082
132.42	1.117	1.115	1.116	1.085
137.39	1.115	1.114	1.114	1.088
142.43	1.114	1.112	1.113	1.091
147.46	1.112	1.111	1.112	1.094
154.78	1.111	1.108	1.110	1.104
164.54	1.108	1.106	1.107	1.108

Table XVIII. Continued

Mean	Smearing Corrections			
E_t (GeV)	Lower Edge	Upper Edge	Mean E_t	Cross Section
171.76	1.106	1.104	1.105	1.112
181.50	1.104	1.102	1.103	1.116
196.69	1.102	1.099	1.100	1.128
212.30	1.099	1.097	1.098	1.131
225.88	1.097	1.094	1.096	1.134
241.99	1.094	1.093	1.094	1.135
258.34	1.093	1.091	1.092	1.143
280.24	1.091	1.089	1.090	1.141
300.00	1.089	1.088	1.088	1.137
320.63	1.088	1.087	1.087	1.131
347.38	1.087	1.086	1.087	1.133
393.87	1.086	1.087	1.086	1.137

jet of some average E_t^{meas}; its relative contribution to E_t^{meas} depends on the jet E_t spectrum and the size of the E_t^{meas} bin.

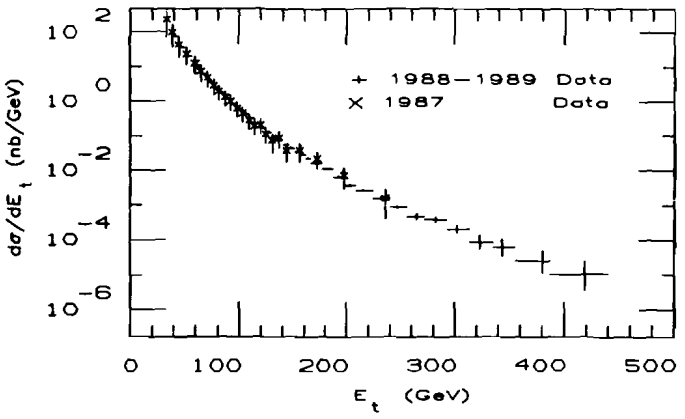

Figure 30. The 1987 cross section for jets with a cone size of 0.6 compared to 1988–1989 cross section for jets with a cone size of 0.7.

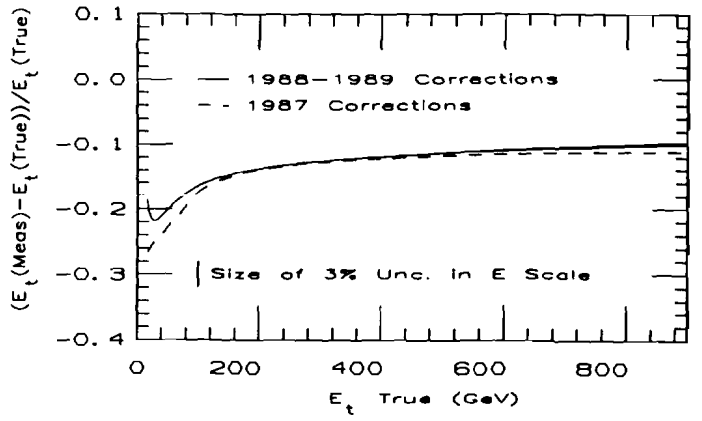

Figure 31. The 1987 E_t corrections compared to the 1988-1989 E_t corrections.

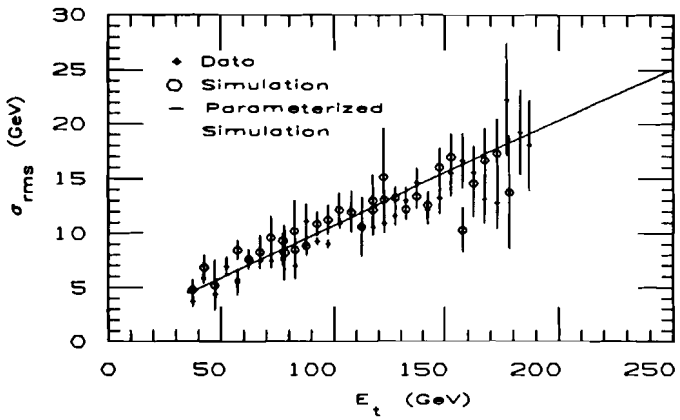

Figure 32. Comparison of the rms resolution for data, simulation and the parameterized response for jets with a cone size of 0.7.

CHAPTER V

SYSTEMATIC UNCERTAINTIES

Systematic uncertainties in the jet E_t scale and resolution introduce a systematic uncertainty into the measurement of the inclusive jet cross section. The systematic uncertainty on the luminosity also contributes to the uncertainty on the cross section. This chapter will describe the uncertainty on the jet E_t scale, jet resolution, and luminosity. It will then explain how these uncertainties are factored into the inclusive jet cross section.

A. E_t Scale Systematic Uncertainties

The jet E_t scale was determined using a detector simulation which was tuned to reproduce the single pion response and the jet fragmentation using both test beam and collider data.[65, 67] The major source of systematic uncertainty on the jet E_t scale is the calorimeter response uncertainty in the azimuthal boundary (cracks) regions of the detector. Other sources of uncertainty on the jet E_t scale include the calorimeter response in other areas of the detector, the fragmentation tuning in the simulation, and the energy from the underlying event (within the clustering cone). The energy from the underlying event is energy associated with the interactions from spectator partons and small collisions occurring without any hard scattering (minimum bias events). An uncertainty is also associated with the jet E_t scale based on preliminary results from the analysis of the 1990 test beam data where a difference in the calorimeter response to pions has been observed.

1. Calorimeter Response

Pions in an energy range from 750 MeV to 20 GeV were extracted from minimum bias collider data, and pions at higher energies of 57 GeV and 145 GeV were used from the 1984/1985 test beam data to measure the single pion response in the central calorimeter. The response of the calorimeter to pions was measured using both the tracking chamber and calorimeter. Neutral pions (π^0's) cannot be measured in the tracking chamber, but do leave energy in the calorimeter. The π^0's that overlap with charged pions can cause the response of the calorimeter towers to pions to be mismeasured. In order to estimate this background, it was assumed that the shower leakage from the target tower was small and that the energy found in neighboring towers was from π^0 background. The background was estimated using the energy found in the neighboring electromagnetic calorimeter towers.

Shower leakage from the target tower and the possibility of finding more π^0's in the target tower than in the neighboring towers are possible sources of mismeasurement for this background. The average border tower energy was small ($\sim$ 2% of the momentum), therefore a conservative 5% systematic uncertainty was assigned to the π^0 background subtraction in the single pion response.[65] This is the dominant uncertainty for pions with energies less than 25 GeV.

The azimuthal crack response observed in the data is not in agreement with the response used in the simulation to obtain the energy and smearing corrections. The size of the shift in the E_t scale calculated using the simulation with and without the azimuthal crack response is a 7% shift in the measured jet E_t. This shift is a measure of the uncertainty in the azimuthal crack response on the E_t scale. Therefore, a 7%

uncertainty on the measured jet E_t was calculated for the azimuthal crack uncertainty using the simulation.

The response in the azimuthal crack region was also studied using pions in the test beam. There was difficulty in determining the amount of muon contamination in the pion beam which varied run by run. Run by run variations in the measured response and the uncertainty in the muon contamination, as well as tower to tower variations in the response and an uncertainty in the tower calibration, gave a total uncertainty of 8% on the crack response.[78] This was the dominant source of uncertainty in the response for pions with energies greater than 25 GeV. This 8% uncertainty on the response is in addition to the 7% uncertainty on the measured jet E_t.

2. Fragmentation Tuning

The non-linearity of the central hadron calorimeter to charged particles is a major contribution to the energy loss of the calorimeter. Jet fragmentation is a measure of the distributions of the charged particles found in the central tracking chamber associated with jets and therefore effects how well the simulation reproduces the jet energy corrections. The overall tuning of the fragmentation in the simulation is in good agreement with the data. The uncertainty in the fragmentation tuning, however, is correlated with the efficiency of finding tracks in jets. The uncertainty in this tracking efficiency therefore affects the uncertainty on the fragmentation tuning. The uncertainty in the efficiency of finding tracks in jets was found to be $\pm 7\%$, based on the trends observed in measuring the efficiency and the correctness of the embedding scheme.

Since the efficiency of finding tracks in jets is related to the ability of the detector to resolve tracks in a dense track environment, the tracking efficiency was parameterized in terms of the distance of closest approach between two charged tracks in the central tracking chamber. The efficiency was determined by injecting charged tracks from Monte Carlo into jet events, and the determining the reconstruction efficiency, and parameterizing this in terms of the average separation to the nearest track in the jet. In this procedure, there is an inherent uncertainty based on whether the efficiency measured in such a way is to be applied to one or two tracks. This uncertainty It was decided to apply the efficiency to both tracks per pair and as a systematic uncertainty on this measurement to use the case of applying the efficiency to one track per pair.

The limited statistics in the data at high E_t meant this efficiency could not be determined for jets with $E_t > 250$ GeV. A limit of 400 GeV was arbitrarily chosen as the E_t at which to pin the efficiency such that above this limit the efficiency does not change. This limit was changed to 250 GeV, a point where the statistics were reasonable in the data, in order to check the uncertainty on this quantity.[67]

3. Underlying Event

The underlying event E_t density was measured using dijet events in the 1987 data; that measurement was used here.[79] Cuts used to define the dijet sample, such as the maximum allowed E_t for any third jet in the event and the azimuthal separation requirements for the jets, give a range of underlying event E_t densities. A systematic uncertainty of $\pm$ 300 MeV/rad^2 reflects the uncertainty on the E_t density due to the choice of appropriate dijet cuts.

Run by run variations in the detector performance were another source of uncertainty in this measurement. These run by run variations gave a systematic uncertainty of ± 100 MeV/rad^2. An additional 80 MeV/rad^2 statistical uncertainty was also associated with this measurement. Finally, the E_t density was determined and found to be independent of jet E_t within ± 100 MeV/rad^2. Together with the other uncertainties, the total uncertainty on the underlying event E_t density was determined to be ± 340 MeV/rad^2.

4. 1990 Test Beam Results

Recent results from the 1990 CDF test beam have led to a difference in the calorimeter response of the detector to 150 GeV pions and the amount of shower leakage from the target tower. Compared to 1985 test beam data, the calorimeter response to 150 GeV pions was found to be 6% lower in the 1990 test beam data. In addition to this change in response, shower leakage from the target tower contributing energy to the neighboring towers was observed in the CEM. This effects the initial assumption that shower leakage from the target tower was small and that all the energy found in neighboring towers was from π^0 background. A study is currently in progress of 1990 test beam data, which also includes examining the calorimeter response to pions at higher energies which may have some effect on this measurement. While analysis of the 1990 test beam data is still under study, these early results need to be examined here to decide if the size of these effects on the jet E_t scale are large enough to warrant further investigation.

5. Resulting Jet E_t Scale Uncertainty

For the calorimeter and fragmentation, the resulting uncertainty on the jet E_t scale was determined using a loss plot. A loss plot is a measure of the average energy lost due to the hadronic non-linearity, which is directly related to the size of the jet corrections. More specifically, it is the sum of the difference in the momentum and the average calorimeter response ($< R(p) >$) of the tracks in the cone of the jet over the measured E_t of the jet, as defined in the following equation,

$$Loss = \frac{\sum_{i=1}^{\#tracks}(< R(p) > - p_{i,j})}{E_{t,j}}. \tag{32}$$

The difference in the average calorimeter response and the momentum of a track is the amount of energy loss by the track in the calorimeter. Summing this difference over all the tracks in a jet gives the amount of energy loss by the jet. Dividing this sum by the measured jet E_t gives the fraction of energy loss by the jet. The difference between the loss plot measured in the data and the simulation (which can be varied to reflect various systematic uncertainties), is a measure of the uncertainty in the jet E_t scale.

To find the effect of the calorimeter uncertainty on the jet E_t scale, the average response of the calorimeter used in making the loss plot was varied in the data by the uncertainty on the single pion response. The resulting loss plots for these uncertainties were then fit to the function:

$$f = \frac{N}{E_t^A} e^{-BE_t}, \tag{33}$$

where E_t is measured jet E_t. The loss plots extracted from the data using the measured calorimeter response, as well as the loss plots obtained by changing the response within it's uncertainties which were mentioned earlier, can be seen in Figure 33. The difference in the fits obtained for these plots multiplied by the measured jet E_t and divided by the corrected jet E_t gives the fractional uncertainty on the corrected (or true) jet E_t scale. The resulting uncertainty on the jet E_t scale for each cone size is listed in Table XIX. This uncertainty includes all the uncertainties on the calorimeter response mentioned earlier except for the 7% uncertainty on the measured jet E_t scale due to the difference in the jet E_t scale calculated using the simulation with and without the azimuthal crack response.

Using this same technique, the fragmentation uncertainties were varied in the simulation and loss plots were extracted for each of the different uncertainties, as well as the tuned value (see Figure 34). The uncertainty for each of these effects on the jet E_t scale is listed in Table XX for each cone size.

The uncertainty on the jet E_t scale due to the uncertainty on the underlying event E_t density is the uncertainty on the E_t density times the area of the jet clustering cone. The area of the jet clustering cone is basically πR^2, where R is the cone size used in the clustering algorithm. For cone sizes of 0.4, 0.7, and 1.0 the uncertainty in the jet E_t scale is 171 MeV, 523 MeV, and 1068 MeV respectively. This uncertainty is independent of jet E_t, thus the fractional uncertainty on this number grows smaller with increasing jet E_t. Table XXI lists this uncertainty as a fraction of the corrected jet E_t.

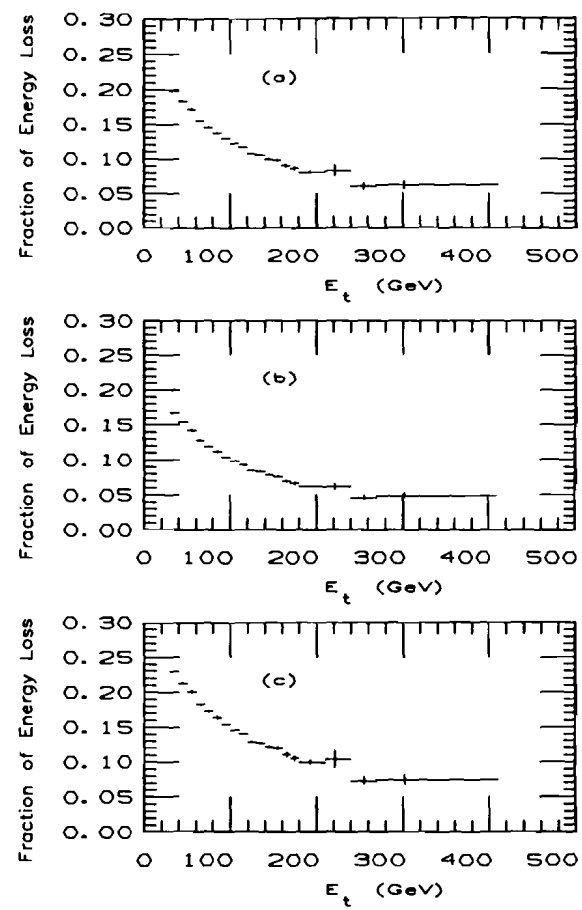

Figure 33. Loss plots as a function of measured jet E_t for the data. Using a) the measured calorimeter response, b) the upper limit of the uncertainty on the response, c) the lower limit of the uncertainty on the response.

Table XIX. Calorimeter response fractional systematic uncertainty on the corrected jet E_t scale.

True Jet	Calorimeter Response		
E_t (GeV)	Cone Size 0.4	Cone Size 0.7	Cone Size 1.0
20.0	0.0265	0.0258	0.0271
40.0	0.0248	0.0247	0.0252
60.0	0.0233	0.0238	0.0241
80.0	0.0220	0.0228	0.0231
100.0	0.0208	0.0218	0.0221
120.0	0.0197	0.0208	0.0212
140.0	0.0186	0.0198	0.0203

In order to examine the size of the effects seen in the 1990 test beam, the calorimeter response in the simulation was changed to reflect the new test beam results. A modified loss plot was made based on generated particle response (which is the calorimeter response of particles generated which does not include the effect of the tracking efficiency in the simulation). The difference in the loss plots made of the generated particle response using the previous response, $< R(p) >$ (based on 1985 test beam results) and the generated particle response using the modified response, $< R_m(p) >$ (based on 1990 test beam results), is a measure of the size of this difference. Figure 35 is a plot of this difference in the fractional energy loss for these generated particle responses. This result was fit to a second order polynomial in order to parameterize this difference. Table XXII lists the results of this uncertainty as

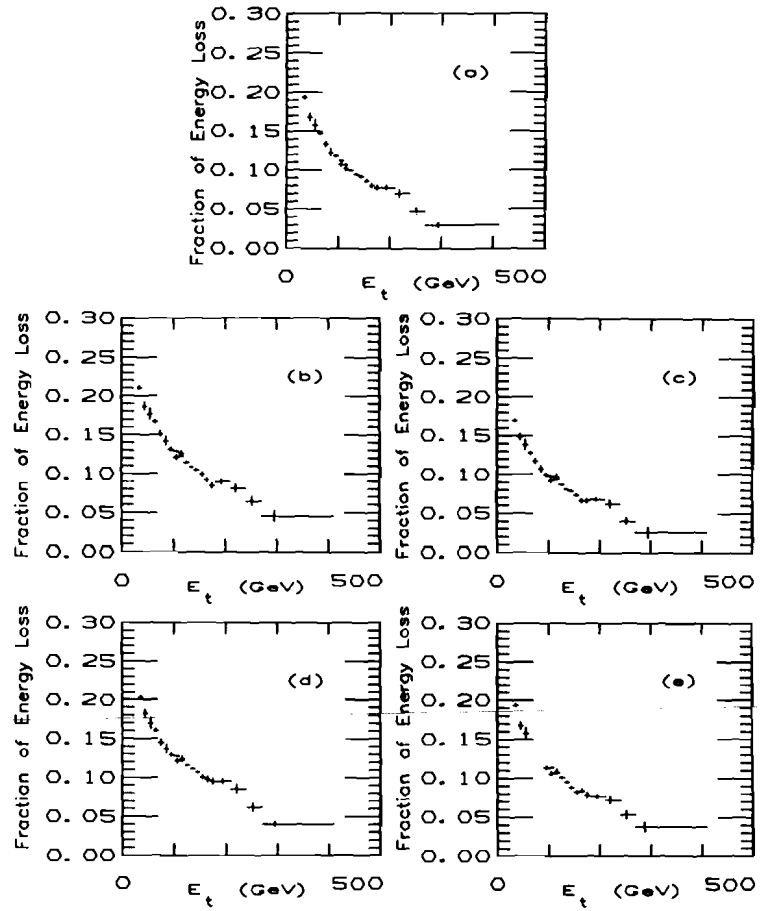

Figure 34. Loss plots from the simulation as a function of measured jet E_t. For, a) the tuned fragmentation, changing the tracking efficiency by b) +7%, c) −7%, d) applying the efficiency to one track per pair instead of two, and e) pinning the efficiency at 250 GeV instead of 400 GeV.

Table XX. Fragmentation fractional systematic uncertainties on the corrected jet E_t scale.

True Jet E_t (GeV)	Fragmentation Tuning	±7% on Efficiency	1-Track per pair	High Pin 250 GeV
		Cone Size 0.4		
20.0	0.0257	0.0188	-0.0131	0.0008
40.0	0.0184	0.0157	-0.0101	0.0003
60.0	0.0148	0.0142	-0.0100	0.0002
80.0	0.0123	0.0132	-0.0107	0.0001
100.0	0.0105	0.0125	-0.0115	0.0000
120.0	0.0091	0.0120	-0.0125	0.0000
140.0	0.0080	0.0115	-0.0134	0.0000
		Cone Size 0.7		
20.0	0.0063	0.0186	-0.0017	-0.0085
40.0	0.0061	0.0172	-0.0071	-0.0012
60.0	0.0065	0.0162	-0.0097	0.0009
80.0	0.0071	0.0152	-0.0113	0.0013
100.0	0.0076	0.0142	-0.0123	0.0011
120.0	0.0080	0.0133	-0.0129	0.0006
140.0	0.0084	0.0125	-0.0133	-0.0001

Table XX. Continued

True Jet E_t (GeV)	Fragmentation Tuning	±7% on Efficiency	1-Track per pair	High Pin 250 GeV
		Cone Size 1.0		
20.0	-0.0092	0.0156	-0.0024	-0.0004
40.0	0.0020	0.0165	-0.0071	0.0000
60.0	0.0062	0.0162	-0.0095	0.0001
80.0	0.0082	0.0156	-0.0110	0.0001
100.0	0.0092	0.0148	-0.0120	0.0001
120.0	0.0095	0.0140	-0.0128	0.0000
140.0	0.0095	0.0131	-0.0133	0.0000

Table XXI. Underlying event E_t density fractional systematic uncertainty on the corrected jet E_t scale.

True Jet	E_t Density		
E_t (GeV)	Cone Size 0.4	Cone Size 0.7	Cone Size 1.0
20.0	0.0085	0.0262	0.0534
40.0	0.0043	0.0131	0.0267
60.0	0.0028	0.0087	0.0178
80.0	0.0021	0.0065	0.0134
100.0	0.0017	0.0052	0.0107
120.0	0.0014	0.0044	0.0089
140.0	0.0012	0.0037	0.0076

a fraction of corrected jet E_t. The size of this effect is smaller than the 7% uncertainty on the measured jet E_t scale resulting from the uncertainty in the azimuthal boundary response. Since the source of this difference is still under study, this uncertainty will be combined with the other uncertainties.

The various uncertainties were then added in quadrature to obtain the total systematic uncertainty on the jet E_t scale. The total systematic uncertainty is listed in Table XXIII. Figure 36 shows the breakdown of the various components of the total uncertainty on the corrected jet E_t scale as a fraction of corrected jet E_t and as a function of the corrected jet E_t.

An additional calibration uncertainty in the central electromagnetic calorimeter was noted during the 1988-1989 collider run, therefore another uncertainty on the

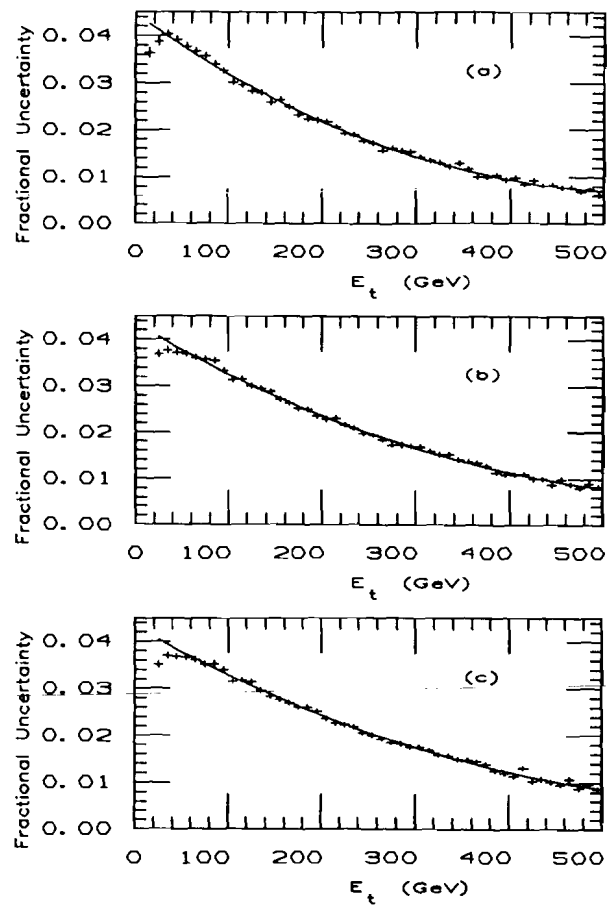

Figure 35. The fractional uncertainty of the corrected jet E_t scale due to the difference in the 1990 test beam with previous test beam results. For a) cone size of 0.4, b) cone size of 0.7, and c) cone size of 1.0.

Table XXII. Fractional uncertainty associated with the difference in the 1990 test beam results and previous test beam results.

True Jet	Test Beam Uncertainty		
E_t (GeV)	Cone Size 0.4	Cone Size 0.7	Cone Size 1.0
20.0	0.0419	0.0411	0.0409
40.0	0.0392	0.0388	0.0388
60.0	0.0367	0.0367	0.0367
80.0	0.0342	0.0346	0.0348
100.0	0.0319	0.0325	0.0328
120.0	0.0297	0.0306	0.0310
140.0	0.0275	0.0287	0.0292

Table XXIII. Total fractional systematic uncertainty on the corrected jet E_t scale for each cone size.

True Jet	Total Systematic		
E_t (GeV)	Cone Size 0.4	Cone Size 0.7	Cone Size 1.0
20.0	0.0812	0.0804	0.0947
40.0	0.0777	0.0758	0.0801
60.0	0.0761	0.0748	0.0770
80.0	0.0749	0.0741	0.0756
100.0	0.0739	0.0734	0.0745
120.0	0.0730	0.0726	0.0736
140.0	0.0722	0.0719	0.0727

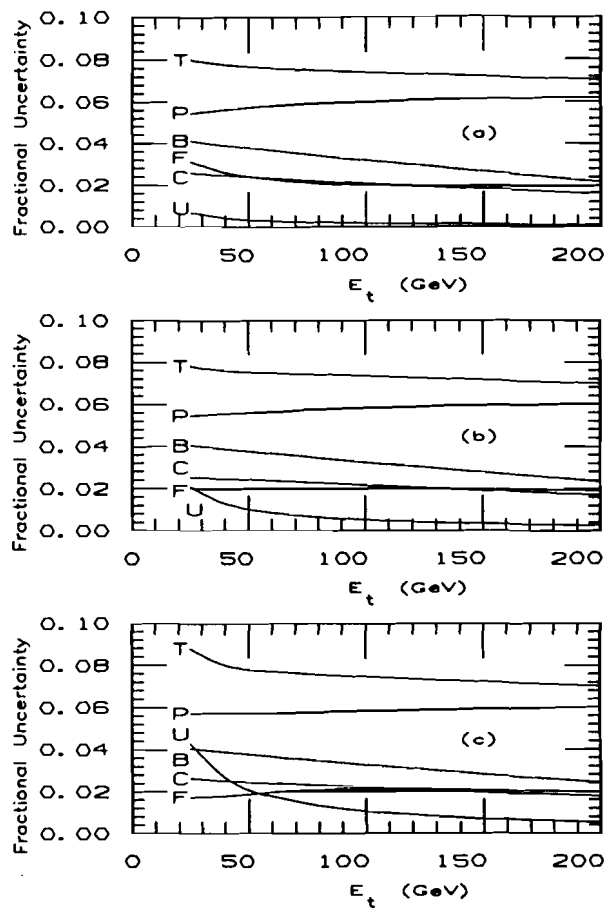

Figure 36. The breakdown of the various components of the total fractional systematic uncertainty on the corrected jet E_t scale for each cone size. For a) cone size of 0.4, b) cone size of 0.7, and c) cone size of 1.0 where the letters represent the following uncertainties: total uncertainty (T), azimuthal crack uncertainty (P), test beam uncertainty (B), calorimeter response (C), fragmentation uncertainty (F), and underlying event (U).

jet E_t scale of 2% was added in quadrature to the resulting uncertainties listed in Table XXIII.

B. Systematic Uncertainty on the Jet Resolution

As a check of the uncertainty on the jet resolution, dijet balancing techniques were used to measure the jet resolution. The uncertainties on the jet resolution due to the use of the simulation is related to the difference in the resolution measured using dijet balancing in both the data and simulation.

Dijet k_t is the vector sum of the transverse momentum in dijet events. It is shown in Appendix A that the width of the $k_{t_\parallel}$ ($\sigma_{k_{t_\parallel}}$) and $k_{t_\perp}$ ($\sigma_{k_{t_\perp}}$) distributions are related to the jet resolution. $\sigma_{k_{t_\parallel}}$ and $\sigma_{k_{t_\perp}}$ have been measured in dijet events for the data and simulation. This information was then used to calculate

$$\sigma' = (\sigma^2_{k_{t_\parallel}} - \sigma^2_{k_{t_\perp}})^{1/2}. \tag{34}$$

The width of the response functions measured in the simulation were parameterized by *Sigma* and *Slope*.[70] These numbers can be related to σ' by using the relation

$$\sigma_{rms} = (Sigma^2 + Slope^2)^{1/2}. \tag{35}$$

This relation expresses the width of the response functions in terms of a single number. The single jet resolution is $\sigma'/\sqrt{2}$ and is directly related to σ_{rms} since both are a measure of the width of the detectors response to jets. Taking the bin by bin difference in $\sigma'/\sqrt{2}$ for the data and simulation gives the systematic difference in the jet resolution. This difference was then fitted to a straight line (parameterized by

slope (m) and offset (b)) in order to parameterize this difference. The errors on the m and b for this line represent the statistical level of uncertainty on this difference.

Changing the parameterized fit by the errors on the m and b, and adding or subtracting the result with the absolute value of the original fit, a band of uncertainty associated with the jet resolution was obtained. Figure 37 shows this result for cone sizes of 0.4, 0.7 and 1.0.

C. Luminosity Uncertainty

The luminosity equals the interaction rate over the effective cross section producing the Beam-Beam counter rates (σ^{eff}_{BBC}). At $\sqrt{s}$ = 1.8 TeV, previous calculations of σ^{eff}_{BBC} depended on the extrapolation of measurements made at the SPS at CERN.[80, 81, 82]

The luminosity calculated using the Beam-Beam counters is expressed as follows,

$$L_{BBC} = \frac{N_{BBC}}{\sigma^{eff}_{BBC}}. \tag{36}$$

The luminosity can also be calculated using accelerator parameters by means of the following expression,

$$L_{Acc} = B\frac{N_p N_{\bar{p}}}{4\pi\sigma_x\sigma_y}f, \tag{37}$$

where B is the number of bunches, N_p and $N_{\bar{p}}$ is the number of protons and antiprotons respectively, σ_x and σ_y are the horizontal and vertical size of the bunch at the interaction point, and f is the revolution frequency of the beams.

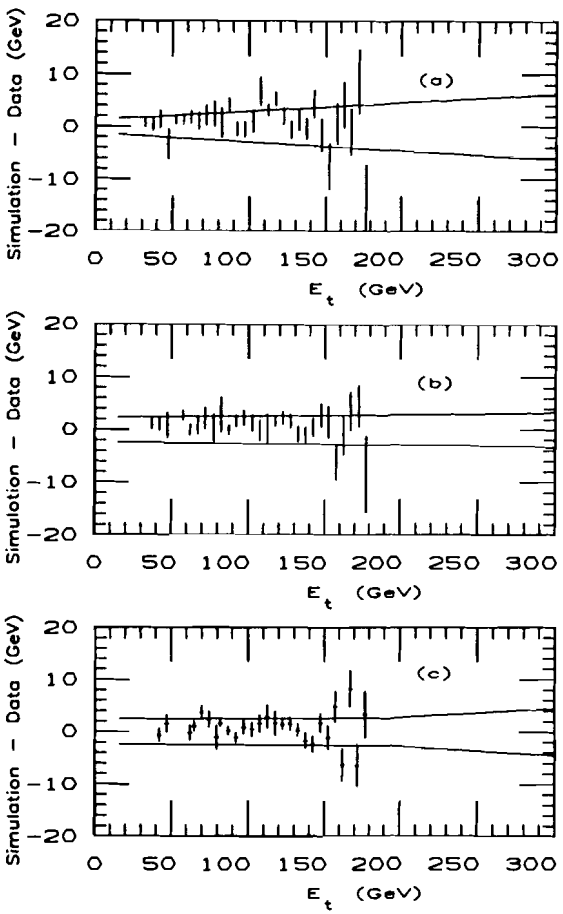

Figure 37. Difference in the rms jet resolution between data and simulation. The lines represent the band of uncertainty associated with this measurement. a) cone size of 0.4, b) cone size of 0.7, and c) cone size of 1.0 .

The ratio of $L_{BBC}(546)/L_{Acc}(546)$ and $L_{BBC}(1800)/L_{Acc}(1800)$ were measured to be 0.753 $\pm$ 0.002 and 0.981 $\pm$ 0.001 respectively.[83] The effective Beam-Beam counter cross section at $\sqrt{s}$ = 1.8 TeV can be expressed by the following equation,

$$\sigma^{eff}_{BBC}(1800) = \sigma^{eff}_{BBC}(546)\frac{L_{BBC}(1800)/L_{Acc}(1800)}{L_{BBC}(546)/L_{Acc}(546)}. \tag{38}$$

The value of $\sigma^{eff}_{BBC}(546)$ has been measured both by the accelerator and UA4 detector to be (32.8 $\pm$ 3.6) mb and (37.1 $\pm$ (5.6%)) mb respectively, for a combined average cross section of (36.0 $\pm$ 1.81) mb. This gives an effective Beam-Beam counter cross section at $\sqrt{s}$ = 1.8 TeV of (46.8 $\pm$ 2.35 $\pm$ 2.16) mb with a total uncertainty of 6.8%.

D. Systematic Uncertainty on the Jet Cross Section

The systematic uncertainties from the jet E_t scale, resolution, and luminosity uncertainty have to be factored into the cross section. The jet E_t scale and resolution are used in the unsmearing procedure to extract the corrected cross section from the data.[70] Therefore, the jet E_t scale and resolution can be varied in the unsmearing procedure to obtain the size of these effects on the cross section. The uncertainty in the luminosity is a normalization uncertainty and was factored into the cross section directly.

The method used for extracting the uncertainty on the cross section arising from the uncertainty on the jet E_t scale and resolution is as follows. The parameterized curve obtained for the corrected cross section is input into the smearing procedure[70] and then the jet E_t scale and resolution are varied separately within their systematic

uncertainties. New corrections are extracted without minimizing the parameterized curve. These new corrections show the size and direction of the systematic uncertainty under study on the cross section. The fractional uncertainty on the cross section is then defined to be the ratio of the difference in the cross section calculated with these new corrections and parameterized curve used as input. This result is then fit to a suitable function, in order to parameterize the fractional uncertainty on the cross section as a function of jet E_t. The results obtained for each cone size when the jet E_t scale was varied are plotted in Figure 38. These results are plotted in terms of the ratio of the uncertainty and the predicted cross section obtained from the parameterized curve. The results obtained for each cone size when the jet resolution was varied are plotted in Figure 39. These results are also plotted in terms of the ratio of the uncertainty and the predicted cross section from the parameterized curve. manner as the results for the jet E_t uncertainty.

The uncertainty on the cross section due to the E_t scale and jet resolution are then added in quadrature with the uncertainty on the luminosity to obtain the full systematic uncertainty on the inclusive jet cross section. The band of systematic uncertainty on the cross section can be seen in Figure 40 for all three cone sizes where it has been plotted as a ratio of the total uncertainty and the predicted cross section from the parameterized curve. Table XXIV, XXV, and XXVI list the systematic uncertainties for each point in the cross section for cone sizes of 0.4, 0.7, and 1.0 respectively.

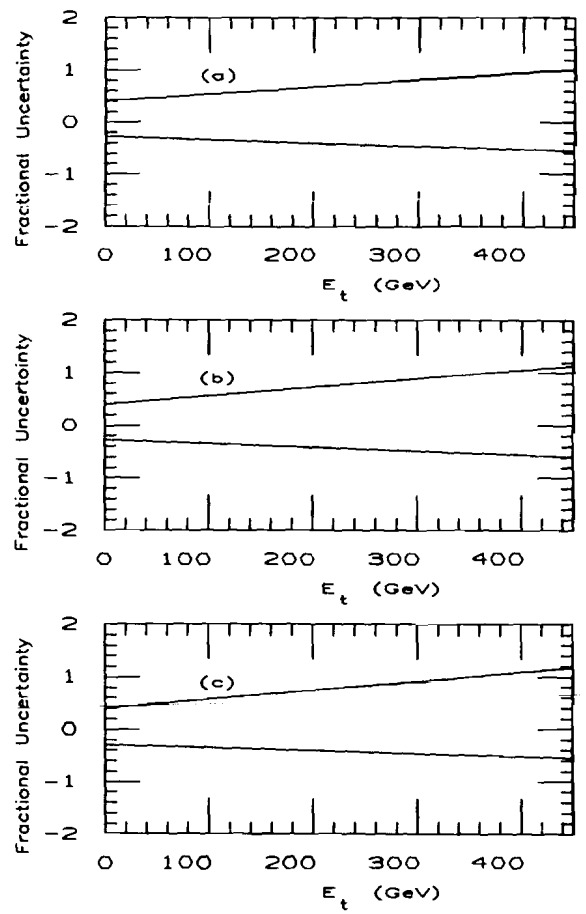

Figure 38. The fraction of uncertainty on the jet cross section, from the uncertainty on the E_t scale. Results are shown for a) cone size of 0.4, b) cone size of 0.7 and c) cone size of 1.0.

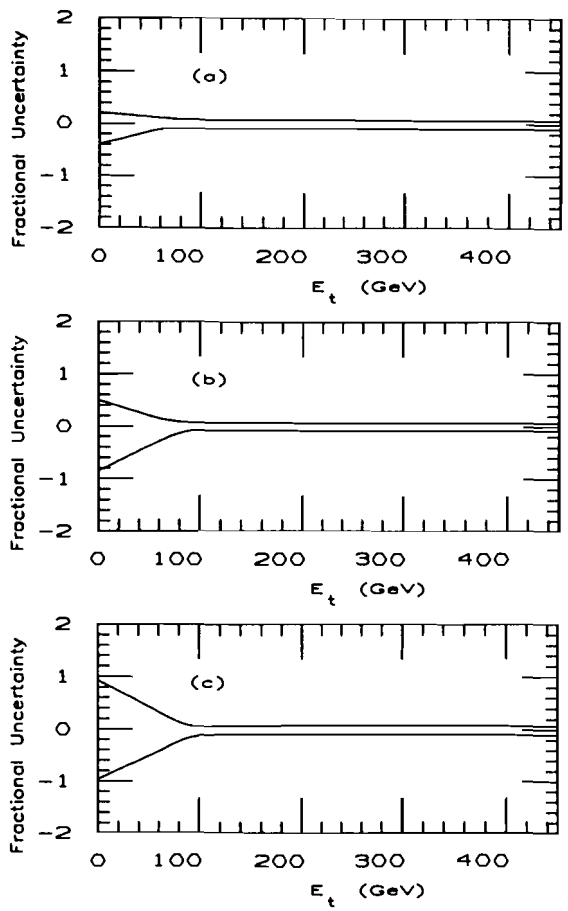

Figure 39. The fraction of uncertainty on the jet cross section, from the uncertainty on the jet resolution. Results are shown for a) cone size of 0.4, b) cone size of 0.7 and c) cone size of 1.0.

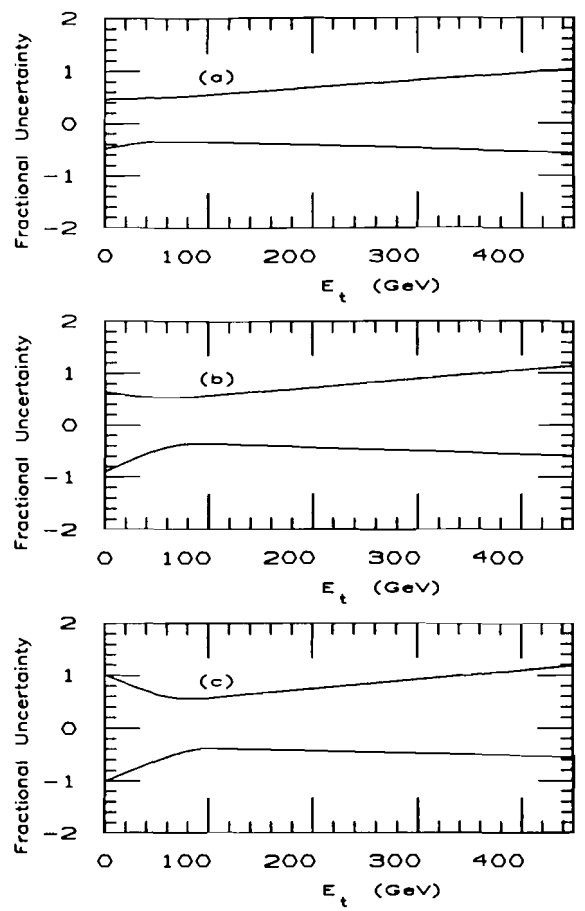

Figure 40. The total fraction of systematic uncertainty on the jet cross section. Results are shown for a) cone size of 0.4, b) cone size of 0.7 and c) cone size of 1.0.

Table XXIV. Percent systematic uncertainty on the inclusive jet cross section for a jet clustering cone size of 0.4.

Mean E_t (GeV)	Systematic Uncertainties E_t Dependent (%)	Total (%)
36.24	+15.50 −4.13	+48.58 −37.21
41.90	+15.93 −2.93	+49.01 −36.00
47.52	+16.39 −1.89	+49.46 −34.97
53.27	+16.88 −1.02	+49.96 −34.10
59.01	+17.39 −0.35	+50.47 −33.43
64.53	+17.92 −0.00	+50.99 −33.08
69.85	+18.44 −0.32	+51.52 −33.40
75.30	+19.00 −0.65	+52.08 −33.73
80.62	+19.57 −0.98	+52.65 −34.05
85.78	+20.14 −1.29	+53.22 −34.37
91.12	+20.83 −1.61	+53.91 −34.69
96.33	+21.53 −1.93	+54.61 −35.01
101.64	+22.25 −2.26	+55.33 −35.33
106.88	+22.96 −2.57	+56.04 −35.65
112.08	+23.66 −2.89	+56.74 −35.97
117.30	+24.37 −3.21	+57.45 −36.29
122.74	+25.11 −3.54	+58.19 −36.62
127.94	+25.81 −3.86	+58.89 −36.94
133.12	+26.51 −4.18	+59.59 −37.26
138.30	+27.22 −4.50	+60.29 −37.58
143.46	+27.91 −4.81	+60.99 −37.89
148.83	+28.64 −5.14	+61.72 −38.22
153.88	+29.33 −5.46	+62.41 −38.53

Table XXIV. Continued

Mean E_t (GeV)	Systematic Uncertainties E_t Dependent (%)	Total (%)
159.07	+30.03 −5.77	+63.11 −38.85
166.90	+31.10 −6.26	+64.17 −39.34
177.03	+32.47 −6.88	+65.55 −39.96
187.49	+33.89 −7.53	+66.97 −40.61
198.23	+35.35 −8.19	+68.43 −41.27
210.38	+37.01 −8.95	+70.08 −42.02
227.23	+39.30 −9.99	+72.38 −43.07
241.41	+41.23 −10.87	+74.31 −43.95
259.30	+43.66 −11.98	+76.74 −45.06
277.46	+46.14 −13.12	+79.22 −46.19
299.20	+49.10 −14.47	+82.18 −47.55
317.64	+51.62 −15.63	+84.70 −48.70
338.92	+54.52 −16.96	+87.60 −50.04
371.08	+58.91 −18.98	+91.99 −52.06
409.19	+64.12 −21.37	+97.20 −54.45

Table XXV. Percent systematic uncertainty on the inclusive jet cross section for a jet clustering cone size of 0.7.

Mean E_t (GeV)	Systematic Uncertainties E_t Dependent (%)	Total (%)
41.63	$^{+18.43}_{-20.16}$	$^{+53.45}_{-55.18}$
47.61	$^{+17.73}_{-15.82}$	$^{+52.75}_{-50.84}$
53.54	$^{+17.27}_{-11.80}$	$^{+52.29}_{-46.82}$
59.93	$^{+17.04}_{-7.89}$	$^{+52.06}_{-42.91}$
66.23	$^{+17.10}_{-4.57}$	$^{+52.12}_{-39.59}$
72.29	$^{+17.41}_{-2.03}$	$^{+52.43}_{-37.05}$
78.15	$^{+18.19}_{-0.30}$	$^{+53.21}_{-35.32}$
83.81	$^{+19.11}_{-0.00}$	$^{+54.13}_{-35.02}$
89.30	$^{+20.01}_{-0.36}$	$^{+55.02}_{-35.38}$
94.82	$^{+20.90}_{-0.72}$	$^{+55.92}_{-35.74}$
100.19	$^{+21.78}_{-1.08}$	$^{+56.80}_{-36.09}$
105.59	$^{+22.66}_{-1.43}$	$^{+57.67}_{-36.45}$
111.04	$^{+23.54}_{-1.79}$	$^{+58.56}_{-36.81}$
116.44	$^{+24.42}_{-2.14}$	$^{+59.44}_{-37.16}$
121.76	$^{+25.29}_{-2.50}$	$^{+60.31}_{-37.51}$
127.12	$^{+26.16}_{-2.85}$	$^{+61.18}_{-37.87}$
132.49	$^{+27.04}_{-3.20}$	$^{+62.06}_{-38.22}$
137.77	$^{+27.90}_{-3.55}$	$^{+62.92}_{-38.57}$
143.05	$^{+28.76}_{-3.90}$	$^{+63.78}_{-38.92}$
148.48	$^{+29.65}_{-4.26}$	$^{+64.67}_{-39.28}$
153.71	$^{+30.50}_{-4.61}$	$^{+65.52}_{-39.63}$
158.92	$^{+31.36}_{-4.95}$	$^{+66.37}_{-39.97}$
164.24	$^{+32.23}_{-5.31}$	$^{+67.24}_{-40.33}$

Table XXV. Continued

Mean E_t (GeV)	Systematic Uncertainties E_t Dependent (%)	Total (%)
171.89	$^{+33.48}_{-5.81}$	$^{+68.49}_{-40.83}$
182.20	$^{+35.16}_{-6.50}$	$^{+70.18}_{-41.52}$
193.03	$^{+36.93}_{-7.22}$	$^{+71.95}_{-42.24}$
203.47	$^{+38.64}_{-7.92}$	$^{+73.66}_{-42.93}$
215.73	$^{+40.65}_{-8.73}$	$^{+75.67}_{-43.75}$
231.87	$^{+43.30}_{-9.81}$	$^{+78.32}_{-44.83}$
246.86	$^{+45.75}_{-10.81}$	$^{+80.77}_{-45.83}$
264.86	$^{+48.71}_{-12.02}$	$^{+83.72}_{-47.04}$
281.96	$^{+51.51}_{-13.17}$	$^{+86.53}_{-48.19}$
302.22	$^{+54.84}_{-14.53}$	$^{+89.86}_{-49.55}$
322.87	$^{+58.23}_{-15.92}$	$^{+93.25}_{-50.94}$
343.87	$^{+61.68}_{-17.33}$	$^{+96.70}_{-52.35}$
380.71	$^{+67.74}_{-19.82}$	$^{+102.76}_{-54.84}$
418.54	$^{+73.96}_{-22.37}$	$^{+108.98}_{-57.39}$

Table XXVI. Percent systematic uncertainty on the inclusive jet cross section for a jet clustering cone size of 1.0.

Mean E_t (GeV)	Systematic Uncertainties E_t Dependent (%)	Total (%)
45.78	+30.81 −27.55	+67.99 −64.73
53.75	+26.55 −21.78	+63.73 −58.96
61.29	+23.23 −16.62	+60.41 −53.81
68.10	+20.93 −12.31	+58.11 −49.49
74.55	+19.44 −8.59	+56.62 −45.77
80.41	+18.71 −5.61	+55.89 −42.79
86.48	+18.65 −3.03	+55.83 −40.21
92.77	+19.72 −0.99	+56.90 −38.17
98.70	+20.73 −0.00	+57.91 −37.18
104.29	+21.69 −0.29	+58.87 −37.47
109.90	+22.65 −0.58	+59.83 −37.76
115.45	+23.59 −0.86	+60.77 −38.05
120.89	+24.53 −1.15	+61.71 −38.33
126.24	+25.44 −1.42	+62.62 −38.60
131.64	+26.36 −1.70	+63.54 −38.88
137.04	+27.29 −1.98	+64.47 −39.16
142.37	+28.20 −2.26	+65.38 −39.44
147.79	+29.13 −2.54	+66.31 −39.72
153.12	+30.04 −2.82	+67.23 −40.00
158.53	+30.97 −3.10	+68.15 −40.28
163.91	+31.90 −3.38	+69.08 −40.56
171.74	+33.24 −3.78	+70.42 −40.97
182.16	+35.03 −4.33	+72.21 −41.51

Table XXVI. Continued

Mean E_t (GeV)	Systematic Uncertainties E_t Dependent (%)	Total (%)
193.07	+36.90 −4.90	+74.08 −42.08
203.44	+38.68 −5.44	+75.86 −42.62
216.42	+40.91 −6.12	+78.10 −43.30
233.06	+43.78 −6.99	+80.96 −44.17
247.46	+46.25 −7.74	+83.43 −44.92
264.64	+49.21 −8.64	+86.39 −45.82
282.03	+52.21 −9.55	+89.39 −46.74
305.43	+56.24 −10.79	+93.42 −47.97
326.53	+59.88 −11.90	+97.06 −49.08
348.63	+63.69 −13.06	+100.88 −50.24
377.44	+68.67 −14.58	+105.85 −51.76
427.84	+77.37 −17.25	+114.55 −54.43

CHAPTER VI

COMPARISONS WITH QCD AND A COMPOSITE MODEL

The measured inclusive jet cross section can be compared to predictions made by QCD and composite models.[19] Composite calculations for the inclusive jet cross section agree with QCD calculations at low values of E_t, but as the E_t increases they start to deviate from one another. The comparison between the data and these models of parton-parton interactions may be used to search for evidence of quark substructure. Below, the procedures followed to compare the data with QCD and to extend the limits on the composite parameter Λ_c are described in detail.

A. Fitting Procedure

In order to compare the measured cross section to theoretical predictions, a fitting procedure was developed to normalize a theoretical cross section to the measured cross section. This fitting procedure had to be able to normalize a theoretical cross section (either QCD or composite models) to the measured cross section in the presence of correlated systematic uncertainties, and in some cases, the presence of large statistical errors in the data. The procedure described in this section attempts to account for both of these effects.

Theoretical points for the inclusive jet cross section are first calculated at the mean E_t for each measured data point. To account for the fact that no jets are observed in the data above the highest E_t bin, the integrated cross section above the

point at which there is no data is also calculated. This is referred to as the empty or null bin in the data.

Normalization of the theoretical distribution to the data is then accomplished using both the statistical errors and systematic uncertainties on the cross section for the data, no attempt is made to account for any theoretical uncertainty. The systematic uncertainty is separated into two parts, an E_t dependent part and an E_t independent part. The E_t independent part is treated as a normalization uncertainty on the data and the E_t dependent part is assumed to be totally correlated bin to bin. This assumption is based on the belief that a systematic uncertainty in one bin of the data is strongly correlated to the systematic uncertainties in the other bins since the source of these uncertainties are the same. This implies that if the cross section in one bin of the data is moved up or down, the cross section in the other bins move up or down coherently.

In order to find the normalization in some region of E_t, the sum of the bin by bin χ^2 is calculated in that region and the normalization is adjusted in order to minimize this χ^2.

In the bins containing more than twenty jets in both the data and the theoretical calculation, the χ^2 is calculated using the statistical errors combined with the systematic uncertainties on the data. The number twenty was chosen for this cutoff in order to be consistent with the use of Poisson statistics in the calculation of the statistical errors on the cross section (see Chapter III). In matrix notation the χ^2 for bins with greater than twenty jets is represented as follows,

$$\chi^2 = \vec{\Delta}^t V^{-1} \vec{\Delta}, \tag{39}$$

where

$$\vec{\Delta} = \begin{pmatrix} \Delta_1 \\ \Delta_2 \\ \vdots \\ \Delta_l \end{pmatrix} \tag{40}$$

and

$$V = \begin{pmatrix} \sigma_{11}^2 & \sigma_{12}^2 & \cdots & \sigma_{1l}^2 \\ \sigma_{21}^2 & \sigma_{22}^2 & \cdots & \sigma_{2l}^2 \\ \vdots & \vdots & \ddots & \vdots \\ \sigma_{l1}^2 & \sigma_{l2}^2 & \cdots & \sigma_{ll}^2 \end{pmatrix}, \tag{41}$$

where l is the number of bins containing more than twenty jets in the fit region. $\vec{\Delta}$ is a vector of differences between the theoretical prediction of the cross section and the measured cross section. Each element in the vector represents one bin in E_t. The matrix V is the error matrix. The diagonal elements are the sum of the squares for the statistical and E_t dependent systematic uncertainties. These elements are defined as follows

$$\sigma_{ii}^2 = \sigma_i^2(stat.) + \sigma_i^2(sys.). \tag{42}$$

where $\sigma_i(stat.)$ and $\sigma_i(sys.)$ are the statistical errors and systematic uncertainties on bin i respectively. The off-diagonal elements are a measure of the correlations between the bins represented by i and j and are defined to be

$$\sigma_{ij}^2 = \rho_{ij}\sigma_i(sys)\sigma_j(sys) \quad \text{for } i \neq j, \tag{43}$$

where ρ_{ij} is the correlation coefficient and $\sigma_i(sys)$ and $\sigma_j(sys)$ represent the systematic uncertainty on bin i and j respectively. The correlation coefficients (ρ_{ij}) were defined to be one since the systematic uncertainties were assumed to be totally correlated from bin to bin.

For the bins with twenty or less jets in either the data or the theoretical calculation (including the empty bin), the χ^2 was formed based on a likelihood ratio test.[61] In this likelihood ratio test the χ^2 in each bin was defined separately to be

$$\chi^2 = -2\ln(\lambda), \tag{44}$$

where

$$\lambda = \frac{e^{-q}q^n}{e^{-n}n^n}. \tag{45}$$

The number of jets predicted by theory is represented by q, and n is the number of jets observed in the data. Factoring Equation 44 after inserting Equation 45 results in

$$\chi^2 = 2((q-n) + n\ln(\frac{n}{q})). \tag{46}$$

This implies that the sum of the χ^2 for all the bins with twenty or fewer jets can be defined to be

$$\chi^2 = 2\sum_{i=1}^{m}((q_i - n_i) + n_i\ln(\frac{n_i}{q_i})), \tag{47}$$

where m is the number of bins containing twenty or fewer jets.

The resulting χ^2 in the fitted region for bins with greater than twenty jets and for bins with twenty jets or less are then combined to form the total χ^2 in the fitted region. The χ^2 in the regions not being used in the fit are also calculated in the same manner allowing these regions to be tested for variations in shape independently of the shape in the fitted region.

B. Comparisons to Leading Order

Both leading order QCD and composite model calculations of the cross section are compared to the measured cross section in the same manner. An appropriate region in E_t is first chosen to normalize the theoretical prediction for the cross section to the data. A normalization region in E_t is chosen for several reasons.

Leading order QCD and composite model predictions for the cross section start to deviate from one another above some value of E_t, but agree at lower values of E_t; the exact value of E_t that this occurs is a function of the compositeness parameter Λ_c. For values of $\Lambda_c \geq 950$ GeV this deviation will occur above an E_t of 160 GeV. Figure 41 shows this deviation in the predictions when using the structure function DFLM set 1.

The systematic uncertainty on the cross section at low E_t is large. In order to avoid having the normalization depend on the data in this region, a lower limit on the fit range was chosen to avoid this region. The fractional systematic uncertainty becomes smallest around 80 GeV (see Chapter V), depending on the cone size under study, so a lower limit of $\sim$ 80 GeV was chosen to avoid this region. Another reason for a lower limit on the fit range when comparing to leading order calculations is the effect of the correction for energy loss outside the clustering cone. When comparing to next-to-leading order calculations, this correction is not appropriate and therefore in this analysis was not applied. For leading order calculations this correction is appropriate. The size of this correction is largest for low values of E_t, therefore when comparing to leading order calculations this can have some effect. This is an

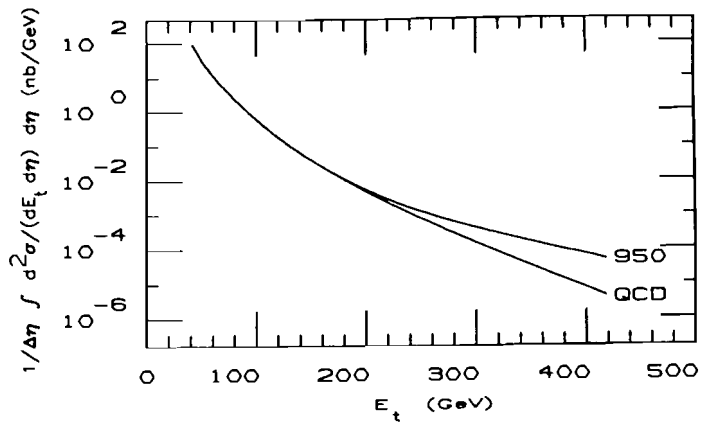

Figure 41. Leading order QCD calculation of the inclusive jet cross section compared to a Composite Model calculation using the structure function DFLM set 1, with $\Lambda_c = 950$ GeV and $Q^2 = 0.5\ E_t^2$.

additional reason for having a lower limit on the range over which leading order calculations are normalized to the data. Table XXVII is a list of the lower and upper E_t limits used to define the fitting region for each cone size, as well as the lower and upper E_t edge of the cross section observed in the data.

With the fit region defined, fits were done for leading order QCD and a Composite Model using a full range of structure functions. The structure functions are related to the probability of finding a parton with a particular momentum inside the proton (or antiproton) and have been measured in deep inelastic scattering experiments.[84]

Table XXVII. List of the lower and upper limits defining the fitting region used for each cone size. Also listed are the lower and upper edges of the cross section observed in the data.

	Fit Range (GeV)		Data Range (GeV)	
Cone Size	Lower Limit	Upper Limit	Lower Edge	Upper Edge
0.4	88.6	161.9	33.7	429.6
0.7	81.2	161.7	38.9	440.0
1.0	83.7	161.3	42.0	445.6

A large number of different structure functions exist. The list of structure functions used in this analysis includes Duke-Owens (DO, sets 1 and 2)[85] and Eichten-Hinchliffe-Lane-Quigg (EHLQ, sets 1 and 2)[27] structure functions which were obtained from the analysis of deep inelastic scattering data available prior to 1984 and used leading order QCD evolution. Diemoz-Ferroni-Longi-Martinelli (DFLM, sets 1, 2 and 3)[86] Martin-Roberts-Stirling (MRS, sets 1, 2, 3, B and E)[87] structure functions are also used in this analysis and are based on newer experimental data available in 1988 using next-to-leading order QCD evolution. Tung-Morfin (TM, sets 1, 2, 3 and 4)[88] structure functions will also be examined in this analysis. Differences within the various sets of structure functions mentioned above concern the treatment of the gluon distribution function and in some cases the use of different experimental data sets as input. In most cases, there exists one set which will use a broad or hard gluon distribution function and one set which uses a soft gluon distribution function.

Those which contain more than two sets will often vary the degree of hardness for this distribution between the two extremes for each set.

The normalization was then found using the prescribed fitting procedure discussed earlier and χ^2's are calculated in all relevant regions using this normalization.

1. QCD

Comparisons to leading order QCD were made using the inclusive jet cross section measured with each of the three cone sizes (0.4, 0.7, and 1.0). Structure functions with a poor χ^2 in the fit region, which yielded a confidence level of less than 5%, were excluded from further use in this analysis (although the results obtained for these structure functions will be tabulated along with the other structure functions). The results of the fitting procedure for a cone size of 0.4 are shown in Table XXVIII. Table XXIX shows the same results for a cone size of 0.7 and Table XXX contains the results for a cone size of 1.0.

Using the remaining structure functions, the combined χ^2's in the fit region, the lower region (bins below the fitted bins) and the upper region (bins above the fitted bins) can be used to determine how well the data is described by leading order QCD using the selected structure functions. Since the measured cross section had a large systematic uncertainty in the lower region and the correction for energy lost outside the clustering cone was not applied, the combined χ^2 used to determine how well the data is described by leading order QCD will be based on only the χ^2 in the fit region and the upper region.

Table XXXI lists the combined χ^2 (fit region combined with upper region), the number of bins (including the empty bin), and the confidence level obtained using

Table XXVIII. The χ^2 and number of bins found in the various regions examined in the fitting procedure for a cone size of 0.4 using the various structure functions.

Structure	Fit Region		Lower Region		Upper Region	
Function	χ^2	NoB	χ^2	NoB	χ^2	NoB
DO 1	11.75	14	7.00	10	16.10	15
DO 2	12.68	14	232.52	10	22.90	15
EHLQ 1	19.69	14	24.36	10	26.90	15
EHLQ 2	24.61	14	10.08	10	42.13	15
DFLM 1	27.40	14	34.23	10	41.19	15
DFLM 2	27.15	14	75.40	10	42.82	15
DFLM 3	24.85	14	115.01	10	39.69	15
MRS 1	12.58	14	9.35	10	17.24	15
MRS 2	9.16	14	146.09	10	14.30	15
MRS 3	7.70	14	6.38	10	14.26	15
MRS E	13.08	14	11.30	10	17.72	15
MRS B	9.71	14	89.18	10	15.15	15
TM 1	17.55	14	64.94	10	18.90	15
TM 2	17.60	14	74.92	10	18.79	15
TM 3	10.11	14	75.05	10	12.47	15
TM 4	16.75	14	24.46	10	18.98	15

Table XXIX. The χ^2 and number of bins found in the various regions examined in the fitting procedure for a cone size of 0.7 using the various structure functions.

Structure	Fit Region		Lower Region		Upper Region	
Function	χ^2	NoB	χ^2	NoB	χ^2	NoB
DO 1	7.09	15	10.80	7	15.43	16
DO 2	27.84	15	198.97	7	55.81	16
EHLQ 1	3.84	15	7.81	7	13.32	16
EHLQ 2	3.59	15	8.25	7	25.66	16
DFLM 1	4.84	15	18.14	7	19.29	16
DFLM 2	4.69	15	32.60	7	21.09	16
DFLM 3	3.23	15	42.35	7	20.85	16
MRS 1	6.60	15	8.95	7	15.43	16
MRS 2	16.36	15	45.91	7	14.08	16
MRS 3	12.03	15	7.20	7	16.40	16
MRS E	6.29	15	8.17	7	15.40	16
MRS B	18.23	15	35.64	7	15.37	16
TM 1	3.22	15	12.13	7	11.55	16
TM 2	3.10	15	13.90	7	11.52	16
TM 3	5.56	15	12.52	7	19.63	16
TM 4	3.84	15	8.03	7	11.43	16

Table XXX. The χ^2 and number of bins found in the various regions examined in the fitting procedure for a cone size of 1.0 using the various structure functions.

Structure	Fit Region		Lower Region		Upper Region	
Function	χ^2	NoB	χ^2	NoB	χ^2	NoB
DO 1	5.66	14	10.83	6	20.21	16
DO 2	21.77	14	186.46	6	48.13	16
EHLQ 1	4.79	14	11.55	6	25.00	16
EHLQ 2	7.69	14	11.33	6	33.33	16
DFLM 1	14.56	14	10.79	6	26.89	16
DFLM 2	14.42	14	13.13	6	29.78	16
DFLM 3	9.88	14	17.45	6	32.93	16
MRS 1	5.50	14	10.49	6	21.39	16
MRS 2	12.41	14	18.23	6	23.92	16
MRS 3	11.96	14	10.99	6	23.91	16
MRS E	5.52	14	10.28	6	20.24	16
MRS B	13.09	14	22.06	6	23.20	16
TM 1	5.86	14	11.68	6	21.72	16
TM 2	5.95	14	11.94	6	21.78	16
TM 3	6.51	14	10.56	6	23.31	16
TM 4	5.42	14	11.27	6	18.36	16

the structure functions for a cone size of 0.4. Table XXXII lists the same information for a cone size of 0.7 and Table XXXIII lists this information for a cone size of 1.0. These tables show the level of agreement between the measured cross section and the predicted leading order QCD cross section. Figure 42 shows the data compared to leading order QCD using the structure function MRS set B for a cone size of 0.4; this information is plotted on both a logarithmic and linear scale. The errors bars in this figure and all other figures, unless otherwise noted, are E_t dependent systematic and statistical uncertainties added in quadrature. The normalization uncertainty and dashed lines shown in these figures represent the E_t independent systematic uncertainty on the cross section. Figure 43 shows the same information for a cone size of 0.4 using the structure function MRS set 3. Figure 44 shows the data compared to leading order QCD using the structure function MRS set B for a cone size of 0.7 and Figure 45 is a comparison of the data to leading order QCD for a cone size of 0.7 using the structure function MRS set 3. Figure 46 shows the data compared to leading order QCD using the structure function MRS set B for a cone size of 1.0 and Figure 47 is a comparison of the data to leading order QCD for a cone size of 1.0 using the structure function MRS set 3.

A slight excess of events can be observed in these figures for high values of E_t. If quarks are composite, then this excess is what would be expected to be observed. This excess will be examined in more detail in the following section.

2. A Composite Model

The cross section calculated using a Composite Model agrees with QCD below $\sim$ 160 GeV, above this compositeness deviates from QCD, this can be seen in

Table XXXI. Combined χ^2 (fit region combined with upper region), number of bins (including the empty bin) and the confidence level obtained using the various structure functions for a cone size of 0.4.

Structure Function	χ^2	NoB	C.L. (%)
DO 1	27.85	29	52.6
DO 2	35.58	29	18.6
EHLQ 1	46.59	29	2.0
EHLQ 2	66.74	29	0.0
DFLM 1	68.59	29	0.0
DFLM 2	69.97	29	0.0
DFLM 3	64.54	29	0.0
MRS 1	29.83	29	42.3
MRS 2	23.46	29	75.5
MRS 3	21.96	29	82.2
MRS E	30.80	29	37.5
MRS B	24.86	29	68.6
TM 1	36.46	29	16.1
TM 2	36.38	29	16.3
TM 3	22.59	29	79.5
TM 4	35.72	29	18.2

Table XXXII. Combined χ^2 (fit region combined with upper region), number of bins (including the empty bin) and the confidence level obtained using the various structure functions for a cone size of 0.7.

Structure Function	χ^2	NoB	C.L. (%)
DO 1	22.51	31	86.6
DO 2	83.65	31	0.0
EHLQ 1	17.16	31	97.9
EHLQ 2	29.25	31	55.6
DFLM 1	24.14	31	80.5
DFLM 2	25.78	31	73.2
DFLM 3	24.08	31	80.7
MRS 1	22.03	31	88.2
MRS 2	30.44	31	49.4
MRS 3	28.43	31	59.9
MRS E	21.69	31	89.3
MRS B	33.61	31	34.2
TM 1	14.76	31	99.4
TM 2	14.62	31	99.4
TM 3	25.19	31	75.9
TM 4	15.27	31	99.2

Table XXXIII. Combined χ^2 (fit region combined with upper region), number of bins (including the empty bin) and the confidence level obtained using the various structure functions for a cone size of 1.0.

Structure Function	χ^2	NoB	C.L. (%)
DO 1	25.87	30	68.2
DO 2	69.91	30	0.6
EHLQ 1	29.79	30	47.7
EHLQ 2	41.02	30	8.7
DFLM 1	41.44	30	8.0
DFLM 2	44.20	30	4.6
DFLM 3	42.81	30	6.1
MRS 1	26.88	30	62.9
MRS 2	36.32	30	19.8
MRS 3	35.87	30	21.2
MRS E	25.77	30	68.7
MRS B	36.29	30	19.9
TM 1	27.57	30	59.3
TM 2	27.72	30	58.5
TM 3	29.83	30	47.5
TM 4	23.78	30	78.2

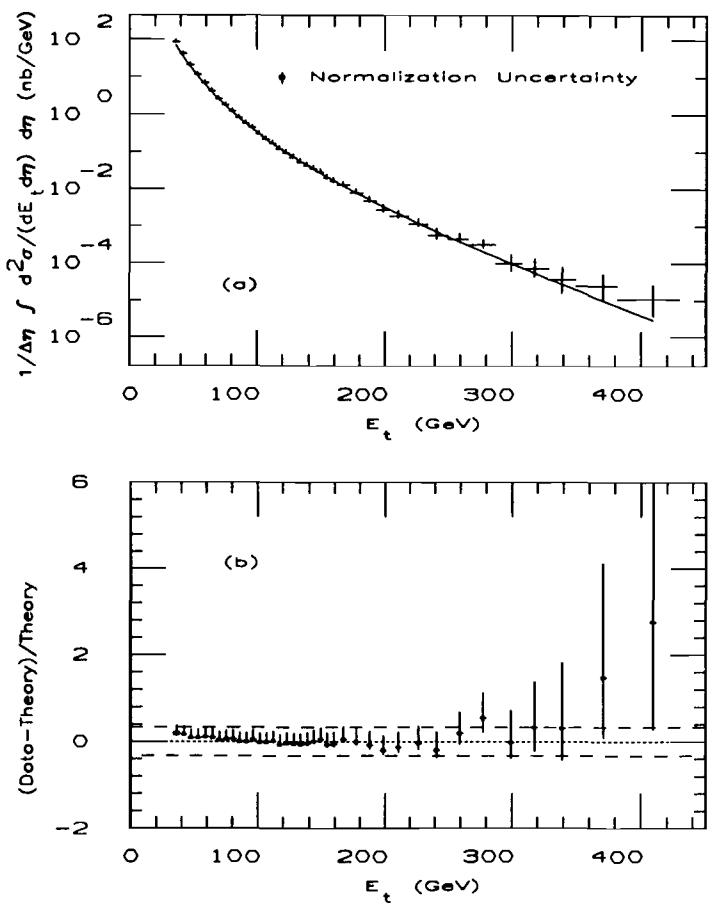

Figure 42. Measured cross section compared to leading order QCD using the structure function MRS set B and a cone size of 0.4. Shown is the a) cross section and b) fractional difference of data with theory.

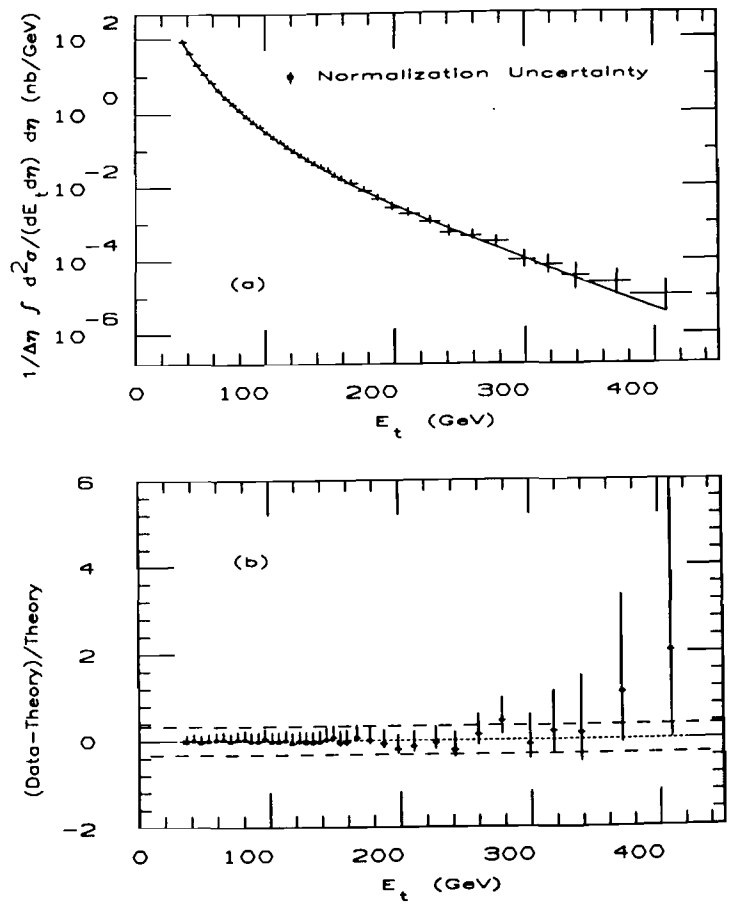

Figure 43. Measured cross section compared to leading order QCD using the structure function MRS set 3 and a cone size of 0.4. Shown is the a) cross section and b) fractional difference of data with theory.

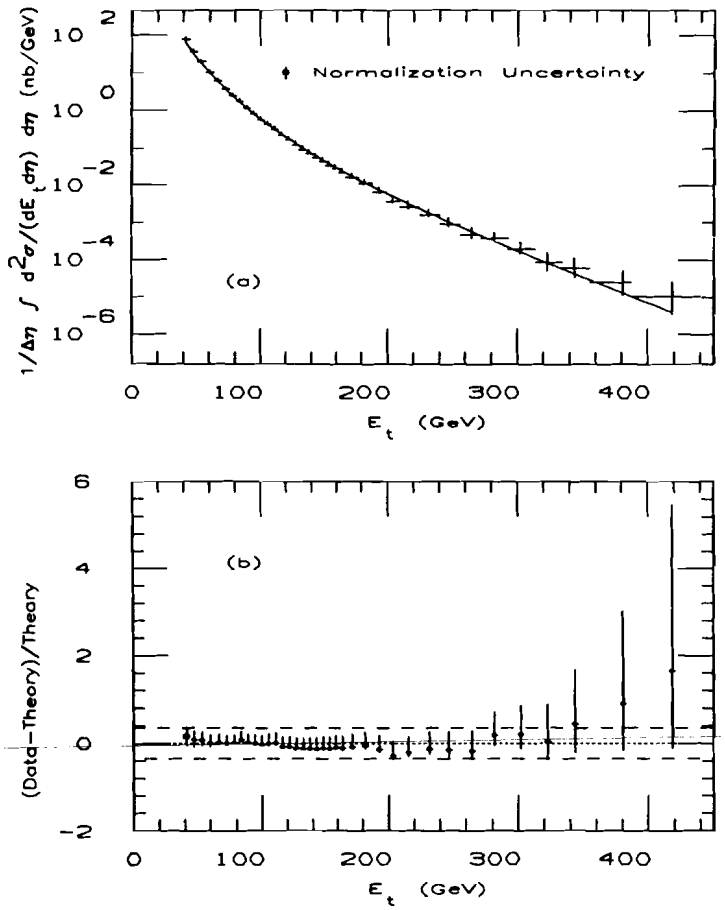

Figure 44. Measured cross section compared to leading order QCD using the structure function MRS set B and a cone size of 0.7. Shown is the a) cross section and b) fractional difference of data with theory.

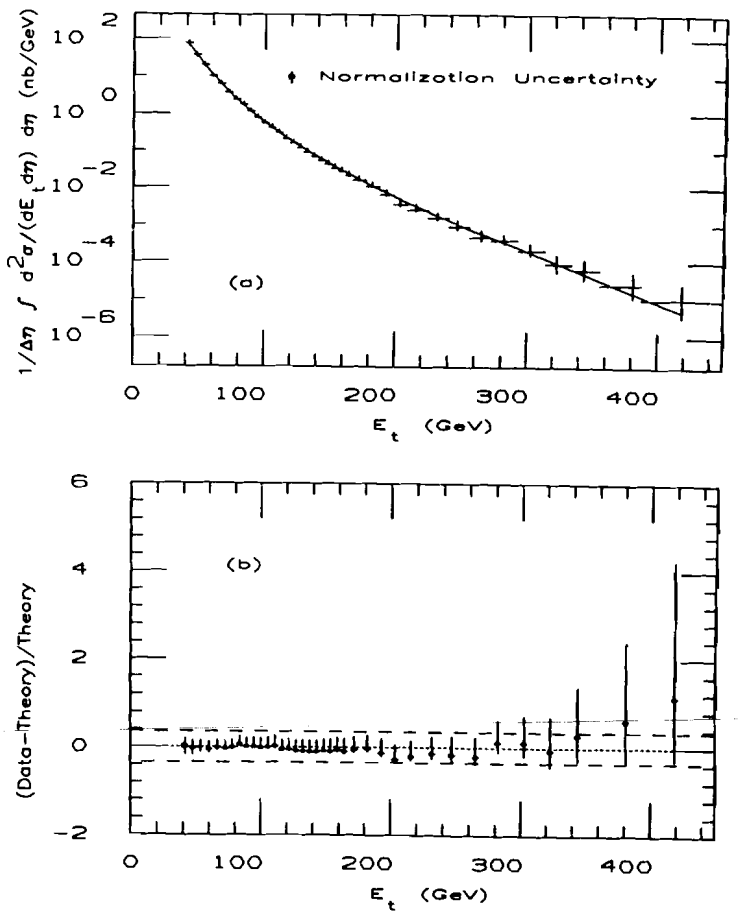

Figure 45. Measured cross section compared to leading order QCD using the structure function MRS set 3 and a cone size of 0.7. Shown is the a) cross section and b) fractional difference of data with theory.

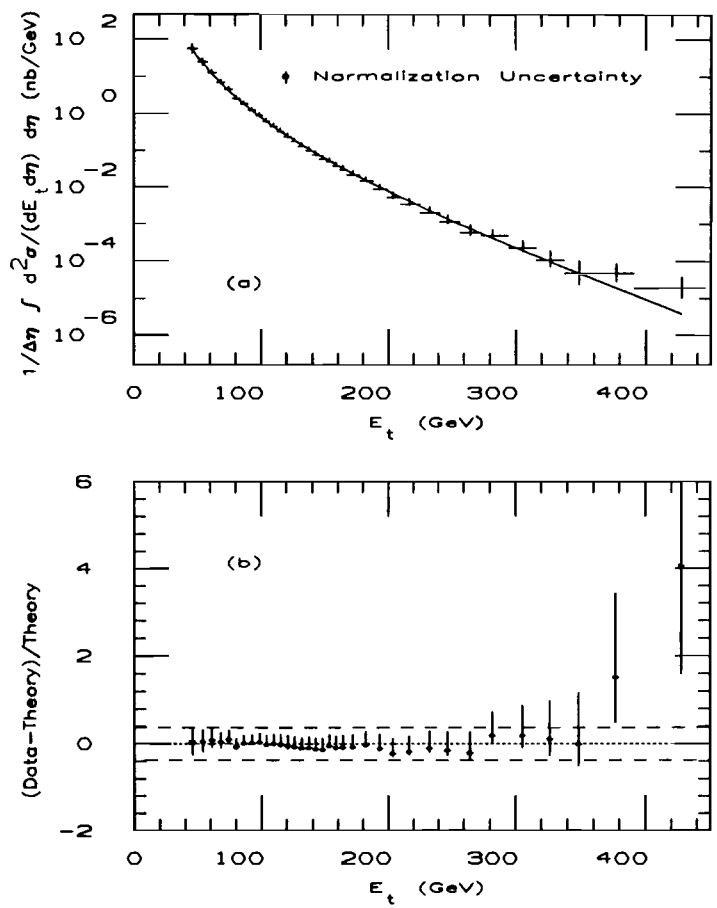

Figure 46. Measured cross section compared to leading order QCD using the structure function MRS set B and a cone size of 1.0. Shown is the a) cross section and b) fractional difference of data with theory.

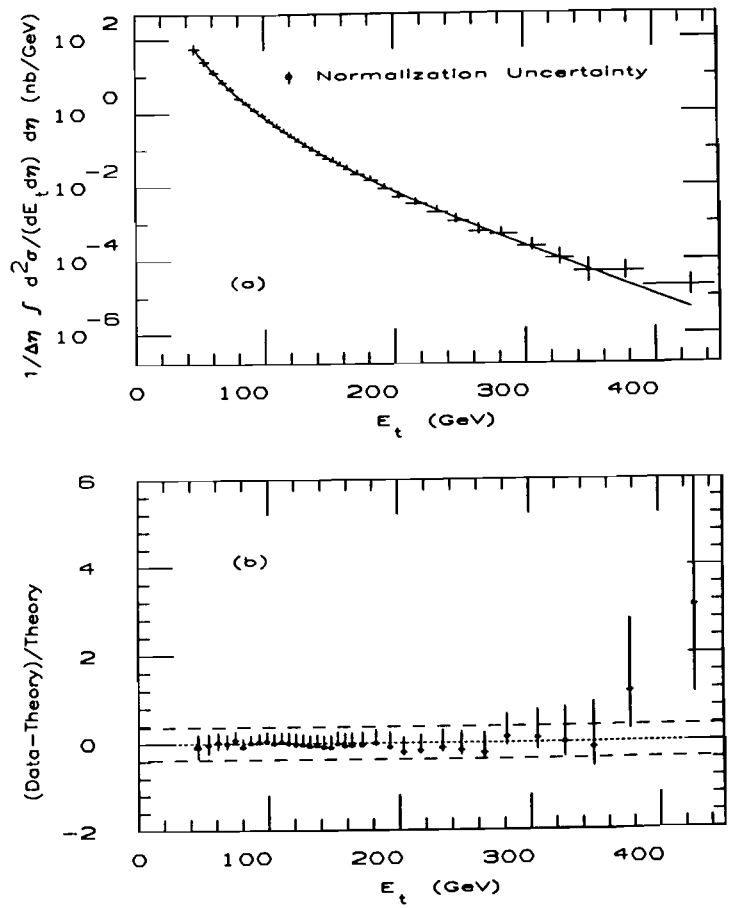

Figure 47. Measured cross section compared to leading order QCD using the structure function MRS set 3 and a cone size of 1.0. Shown is the a) cross section and b) fractional difference of data with theory.

Figure 41 when using the structure function DFLM set 1. Fitting the composite calculation of the cross section to the measured cross section below this limit therefore allows the upper region to be examined in order to search for any possible composite signal. If no signal is observed, the confidence level calculated in the upper region allows a lower limit on the value of the composite scale parameter Λ_c to be set.

Using the structure functions which yielded confidence levels of more than 5% in the fitted region for QCD, the measured cross section has been fit to the cross section calculated for a Composite Model. The confidence levels calculated in the fit region and the upper region for the various values of Λ_c used in the Composite Model are listed in Table XXXIV for a cone size of 0.4, Table XXXV for a cone size of 0.7, and Table XXXVI for a cone size of 1.0.

Figure 48 shows the measured cross section compared to the composite calculation (Λ_c = 980 GeV) on both a linear and logarithmic scale using structure function MRS set 2 for a cone size of 0.4. Figure 49 shows the same comparison for a value of Λ_c = 1010 GeV. Figure 50 shows the measured cross section compared to the composite calculation (Λ_c = 1050 GeV) on both a linear and logarithmic scale using structure function EHLQ set 2 for a cone size of 0.7. Figure 51 shows the same comparison for a value of Λ_c = 1090 GeV. Figure 52 shows the measured cross section compared to the composite calculation (Λ_c = 1100 GeV) on both a linear and logarithmic scale using structure function EHLQ set 2 for a cone size of 1.0. Figure 53 shows this comparison for a value of Λ_c = 1130 GeV using the structure function DFLM set 3 for the same cone size.

Table XXXIV. Confidence Levels (%) in the fit region and upper region for a cone size of 0.4 using the various structure functions.

Structure	Λ_c = 950 GeV		Λ_c = 1000 GeV		Λ_c = 1050 GeV		Λ_c = 1100 GeV	
Function	Fit	Upper	Fit	Upper	Fit	Upper	Fit	Upper
DO 1	75.4	0.0	71.4	0.0	67.2	0.2	63.6	1.7
DO 2	4.4	0.0	42.3	0.0	43.4	0.0	44.2	0.0
EHLQ 1	19.7	0.0	16.2	0.1	13.3	0.8	12.7	3.1
EHLQ 2	4.0	0.0	3.4	0.0	3.1	0.0	3.0	0.0
DFLM 1	2.2	0.0	1.7	0.0	1.5	0.0	1.3	0.0
DFLM 2	2.0	0.0	1.7	0.0	1.5	0.0	1.3	0.0
DFLM 3	3.6	0.0	3.1	0.0	2.8	0.0	2.5	0.0
MRS 1	76.2	0.0	69.9	0.0	64.9	0.1	61.4	0.7
MRS 2	76.7	1.2	76.9	7.3	77.4	18.4	77.1	32.5
MRS 3	87.5	0.0	87.9	0.0	87.9	0.1	87.8	1.1
MRS E	55.2	0.0	64.9	0.0	45.9	0.0	42.7	1.7
MRS B	64.6	0.1	69.6	1.1	70.5	7.1	70.9	17.7
TM 1	31.4	0.0	24.9	0.0	21.6	0.0	19.1	0.0
TM 2	31.2	0.0	26.6	0.0	22.6	0.0	20.7	0.1
TM 3	88.5	0.0	84.8	0.0	82.0	0.0	79.0	0.0
TM 4	33.2	0.0	27.5	0.0	25.3	0.0	23.7	0.0

Table XXXV. Confidence Levels (%) in the fit region and upper region for a cone size of 0.7 using the various structure functions.

Structure	Λ_c = 1000 GeV		Λ_c = 1050 GeV		Λ_c = 1100 GeV		Λ_c = 1150 GeV	
Function	Fit	Upper	Fit	Upper	Fit	Upper	Fit	Upper
DO 1	93.8	0.0	94.1	0.0	94.3	0.0	94.4	0.0
DO 2	1.9	0.0	1.9	0.0	2.0	0.0	2.0	0.0
EHLQ 1	99.7	0.0	99.6	0.0	99.6	0.9	99.7	6.7
EHLQ 2	99.8	0.4	99.8	4.3	99.8	12.4	99.8	23.0
DFLM 1	99.5	0.0	99.4	0.0	99.3	0.0	99.1	0.5
DFLM 2	99.6	0.0	99.4	0.2	99.2	1.9	99.1	7.3
DFLM 3	99.9	0.3	99.9	2.7	99.9	10.7	99.9	21.6
MRS 1	95.8	0.0	96.1	0.0	96.2	0.0	96.3	0.0
MRS 2	25.6	0.0	27.3	0.2	28.0	1.6	29.0	6.1
MRS 3	66.0	0.0	63.8	0.0	61.3	0.0	60.8	0.0
MRS E	96.9	0.0	97.2	0.0	97.1	0.0	97.1	0.0
MRS B	17.4	0.0	15.8	0.0	14.5	0.0	18.4	1.4
TM 1	99.6	0.0	99.6	0.0	99.5	0.0	99.7	0.0
TM 2	99.7	0.0	99.6	0.0	99.6	0.0	99.7	0.0
TM 3	96.1	0.0	96.9	0.0	97.4	0.0	97.6	0.0
TM 4	99.5	0.0	99.4	0.0	99.3	0.0	99.2	0.0

Table XXXVI. Confidence Levels (%) in the fit region and upper region for a cone size of 1.0 using the various structure functions.

Structure	Λ_c = 1050 GeV		Λ_c = 1100 GeV		Λ_c = 1150 GeV		Λ_c = 1200 GeV	
Function	Fit	Upper	Fit	Upper	Fit	Upper	Fit	Upper
DO 1	94.9	0.0	95.4	0.0	95.7	0.0	95.7	0.0
DO 2	6.0	0.0	6.3	0.0	6.5	0.0	6.4	0.0
EHLQ 1	96.5	0.0	96.4	0.2	97.0	1.6	97.1	6.3
EHLQ 2	90.5	1.2	88.9	4.6	87.9	9.7	86.8	12.1
DFLM 1	51.1	0.0	36.2	0.0	39.5	0.0	35.1	0.1
DFLM 2	47.5	0.0	41.1	0.1	37.0	0.3	30.1	10.8
DFLM 3	73.4	0.4	70.4	1.4	65.4	17.1	65.9	16.6
MRS 1	95.5	0.0	96.0	0.0	96.2	0.0	96.3	0.0
MRS 2	49.1	0.0	49.8	0.6	50.1	2.9	50.4	7.2
MRS 3	50.4	0.0	51.4	0.0	52.0	0.0	52.3	0.0
MRS E	95.8	0.0	96.1	0.0	96.3	0.0	96.2	0.0
MRS B	40.9	0.0	41.8	0.0	43.0	0.3	43.3	1.7
TM 1	96.8	0.0	96.6	0.0	96.5	0.0	96.2	0.0
TM 2	96.7	0.0	96.3	0.0	96.2	0.0	95.7	0.0
TM 3	85.9	0.0	86.9	0.0	90.5	0.0	91.3	0.0
TM 4	97.4	0.0	97.4	0.0	97.1	0.0	96.9	0.0

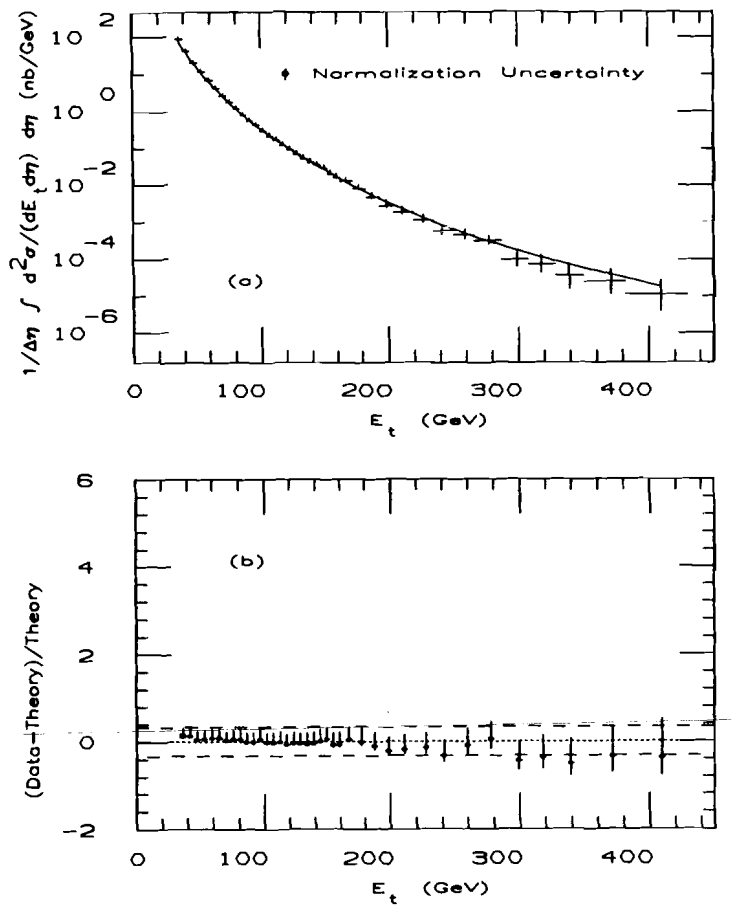

Figure 48. Composite calculation (Λ_c = 980 GeV) of the inclusive jet cross section compare to the measure cross section using the structure function MRS set 2 and a cone size of 0.4. Shown is the a) cross section and b) fractional difference of data with theory.

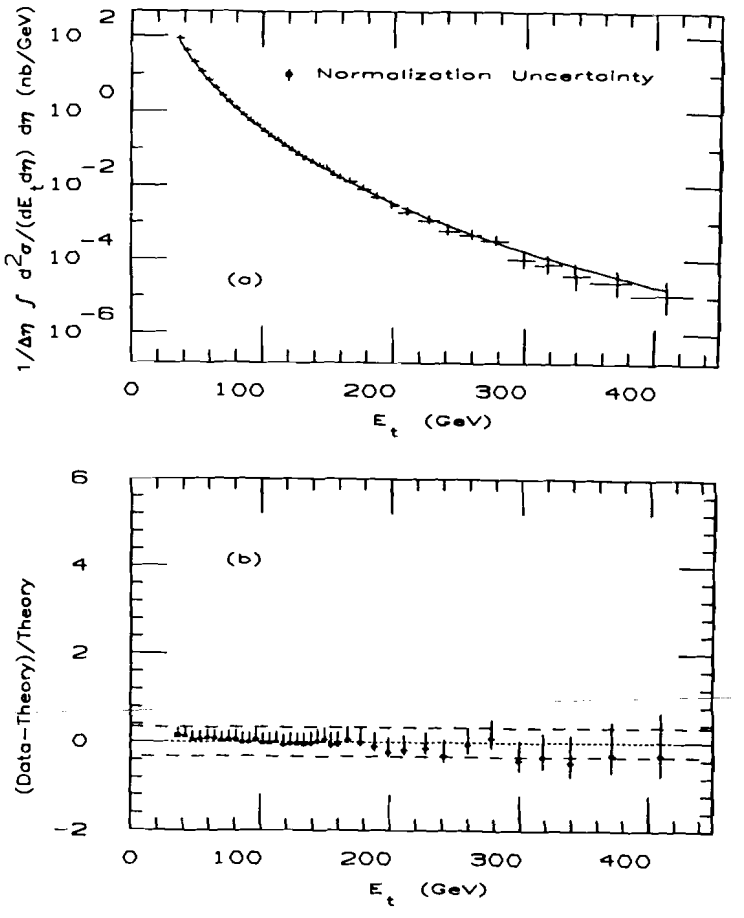

Figure 49. Composite calculation (Λ_c = 1010 GeV) of the inclusive jet cross section compare to the measure cross section using the structure function MRS set 2 and a cone size of 0.4. Shown is the a) cross section and b) fractional difference of data with theory.

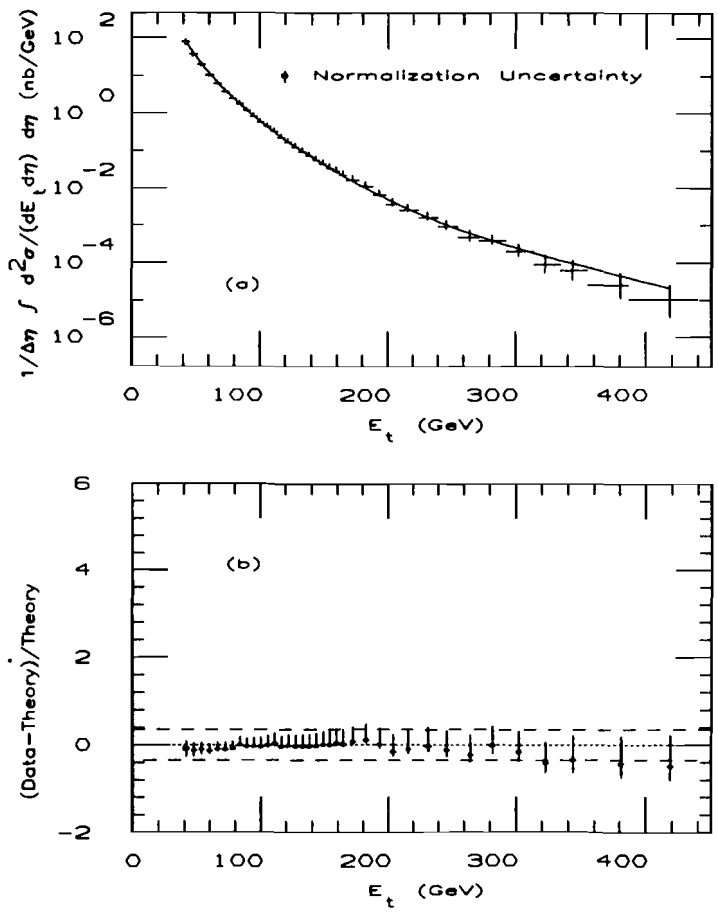

Figure 50. Composite calculation (Λ_c = 1050 GeV) of the inclusive jet cross section compare to the measure cross section using the structure function EHLQ set 2 and a cone size of 0.7. Shown is the a) cross section and b) fractional difference of data with theory.

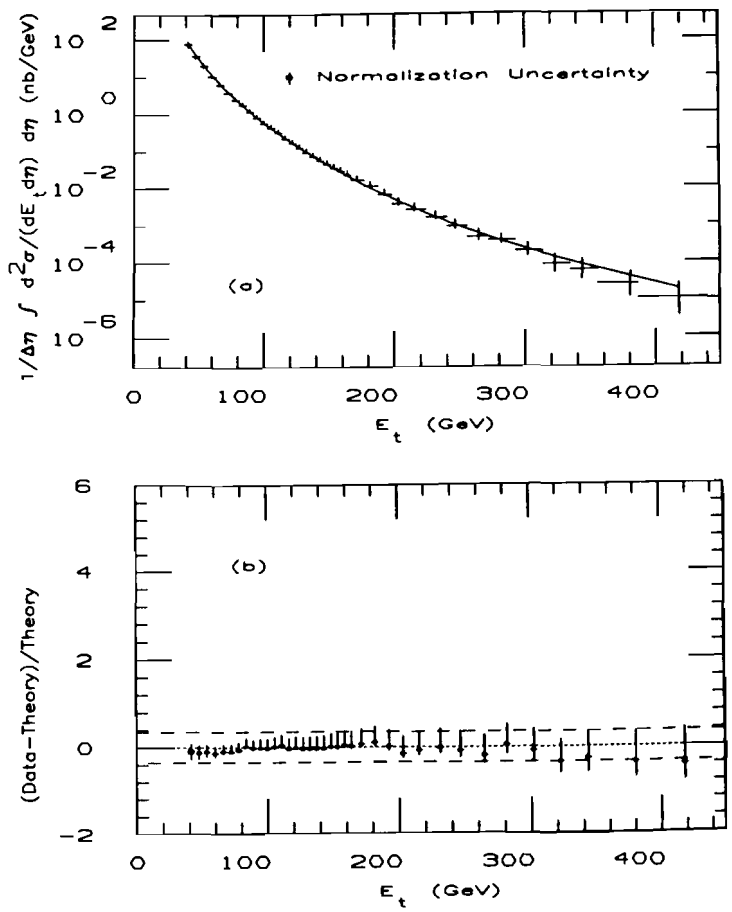

Figure 51. Composite calculation (Λ_c = 1090 GeV) of the inclusive jet cross section compare to the measure cross section using the structure function EHLQ set 2 and a cone size of 0.7. Shown is the a) cross section and b) fractional difference of data with theory.

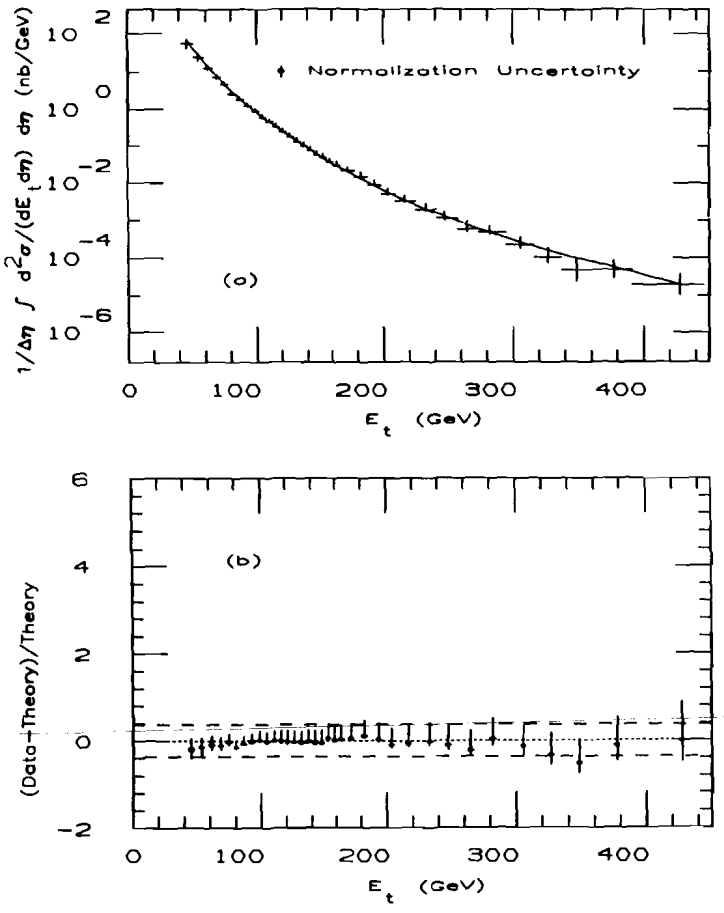

Figure 52. Composite calculation (Λ_c = 1100 GeV) of the inclusive jet cross section compare to the measure cross section using the structure function EHLQ set 2 and a cone size of 1.0. Shown is the a) cross section and b) fractional difference of data with theory.

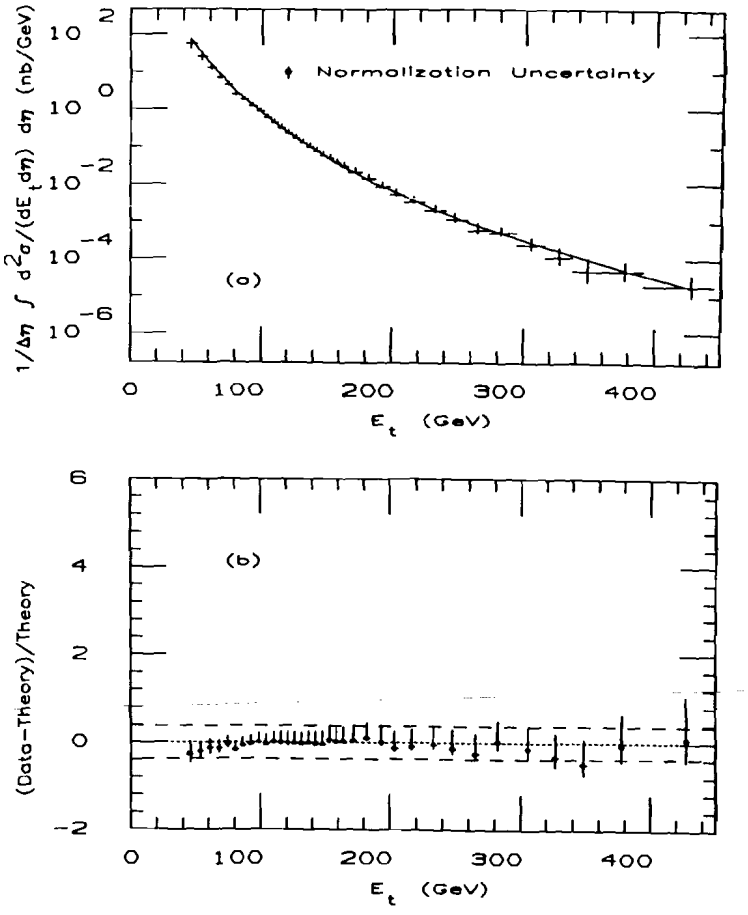

Figure 53. Composite calculation (Λ_c = 1130 GeV) of the inclusive jet cross section compare to the measure cross section using the structure function DFLM set 3 and a cone size of 1.0. Shown is the a) cross section and b) fractional difference of data with theory.

The slight excess of events observed in Figures 42, 43, 44, 45, 46, and 47 may indicate the possibility of new physics. Using the normalization obtained in the fit region and the corrections obtained for the data, the number of jets expected to be observed for QCD and Compositeness can be calculated. The difference in the number of jets predicted and the number of jets observed divided by the square root of the number of predicted jets is a measure of the significance of this excess. Tables XXXVII, XXXVIII, XXXIX list the number of jets found in the region of excess and the number of jets predicted by various theoretical models for the different cone sizes. The significance is also calculated and listed in these tables. As shown in Tables XXXVII, XXXVIII, XXXIX the significance of this excess is on the level of 1-3 sigma, depending on the choice of structure function, and therefore its statistical significance is questionable.

As shown in Table XL, the number of jets and the number of events per bin is nearly the same in the last six bins of the data (where the excess is observed) for each cone size. Thus, the effect of the statistical uncertainty, due to the counting of independent events, on the fitting procedure is small. As the systematic uncertainty is large for these bins, this statistical effect was ignored in the fitting procedure. The total number of jets is slightly larger than the total number of events in the last six bins. This is due to the fact that in most cases if there is a second jet in the event contributing to the cross section, then these two jets nearly balance in E_t. This has a small effect on the calculation of the significance mentioned in the previous paragraph. It also suggests that the number of events in the data may be compared

Table XXXVII. Number of jets found in the E_t range from 266.0 to 429.6 GeV, number of jets predicted by theory and the significance of this excess for a cone size of 0.4.

Structure	Number of Jets		
Function	Data	Theory	Significance
DO 1	48	39.2	-1.40
DO 2	48	50.8	0.39
EHLQ 1	48	33.8	-2.44
EHLQ 2	48	27.0	-4.03
DFLM 1	48	29.4	-3.43
DFLM 2	48	28.1	-3.76
DFLM 3	48	28.5	-3.66
MRS 1	48	38.0	-1.63
MRS 2	48	36.6	-1.89
MRS 3	48	41.0	-1.09
MRS E	48	37.7	-1.67
MRS B	48	37.5	-1.72
TM 1	48	39.8	-1.29
TM 2	48	40.0	-1.27
TM 3	48	44.7	-0.49
TM 4	48	39.9	-1.28

Table XXXVIII. Number of jets found in the E_t range from 271.9 to 440.0 GeV, number of jets predicted by theory and the significance of this excess for a cone size of 0.7.

Structure	Number of Jets		
Function	Data	Theory	Significance
DO 1	64	58.9	-0.67
DO 2	64	135.7	6.16
EHLQ 1	64	49.7	-2.02
EHLQ 2	64	42.7	-3.26
DFLM 1	64	48.2	-2.28
DFLM 2	64	45.7	-2.70
DFLM 3	64	45.1	-2.82
MRS 1	64	56.8	-0.96
MRS 2	64	57.8	-0.82
MRS 3	64	60.1	-0.50
MRS E	64	56.5	-1.00
MRS B	64	55.5	-1.14
TM 1	64	69.5	0.66
TM 2	64	69.8	0.69
TM 3	64	80.7	1.86
TM 4	64	69.7	0.68

Table XXXIX. Number of jets found in the E_t range from 273.2 to 445.6 GeV, number of jets predicted by theory and the significance of this excess for a cone size of 1.0.

Structure	Number of Jets		
Function	Data	Theory	Significance
DO 1	83	74.0	-1.04
DO 2	83	156.4	5.87
EHLQ 1	83	63.8	-2.41
EHLQ 2	83	57.3	-3.40
DFLM 1	83	64.0	-2.38
DFLM 2	83	60.7	-2.86
DFLM 3	83	59.2	-3.09
MRS 1	83	71.3	-1.38
MRS 2	83	69.4	-1.64
MRS 3	83	77.1	-0.67
MRS E	83	71.9	-1.31
MRS B	83	71.5	-1.36
TM 1	83	95.5	1.28
TM 2	83	95.8	1.31
TM 3	83	104.7	2.12
TM 4	83	95.7	1.29

Table XL. Number of jets over the number of events per bin found in the last six bins of the data. Also listed is the total number of jets over the total number of events summed over the last six bins of the data. The results are given for jet clustering cone sizes of 0.4, 0.7, and 1.0.

	Cone Size		
Bin	0.4	0.7	1.0
Last-5	26/23	31/28	41/37
Last-4	8/8	16/14	19/17
Last-3	6/6	7/7	9/9
Last-2	3/3	5/5	4/4
Last-1	3/3	3/3	6/6
Last	2/1	2/1	4/3
Total	48/40	64/55	83/69

to the number of events predicted by QCD (since number of events is an independent quantity) when calculating the significance of an excess.

Based on the confidence level calculated in the upper region for the various structure functions and various values of Λ_c, a lower limit on the value of the compositeness scale parameter Λ_c can be set. Using the structure functions which did not yield a poor χ^2 in the fit region for QCD and which gave the best confidence level in the upper region when fitting for compositeness, a conservative limit on Λ_c can set for each cone size. At the 90% confidence level $\Lambda_c > 1010$ GeV for a cone size of 0.4, $\Lambda_c > 1090$ GeV for a cone size of 0.7, and $\Lambda_c > 1130$ GeV for a cone size of 1.0. At the 95% confidence level $\Lambda_c > 980$ GeV for a cone size of 0.4, $\Lambda_c > 1050$ GeV for a cone size of 0.7, and $\Lambda_c > 1100$ GeV for a cone size of 1.0.

The increase in the limit that is found for the composite parameter Λ_c when the cone size is increased is because the correction for energy lost outside the clustering cone is not being applied. This causes the E_t of the jets to be larger when the cone size is increased, thus extending the E_t range covered by the cross section. The higher in E_t the cross section extends, the larger the limit that can be set on this parameter. This correction is smallest for larger cone sizes (since less energy can be lost outside the cone) and thus the limit obtained from the larger cone sizes is more accurate when comparing to a leading order QCD calculation which requires this correction to be applied. Therefore, an absolute limit of $\Lambda_c > 1100$ GeV can be set at the 95% C.L. based on a comparison of leading order QCD to the measured jet cross section.

C. Comparisons to Next-to-Leading Order

Comparisons to next-to-leading order QCD calculations of the inclusive jet cross section are done in the same manner as the comparisons are done for leading order. Variations in cross section as a function of cone size can also be investigated when comparing to next-to-leading order QCD. Both of these comparisons will be examined in this section. Due to the limited availability of computer time and the length of time required to calculate the next-to-leading order QCD cross section, only the structure function MRS set B could be used to calculate the next-to-leading order QCD cross section in this analysis, using $Q^2 = (P_t/2)^2$. Figure 54 shows a comparison of leading

order QCD to next-to-leading order QCD using the structure function MRS set B.

Using this structure function and the same fit regions as described for the leading order fits, comparisons were made to measured inclusive jet cross section for cone sizes of 0.4, 0.7 and 1.0. Table XLI lists the χ^2's, confidence levels and number of bins found in each region for each cone size. Figure 55 shows the agreement between the next-to-leading order QCD calculation and the data for a cone size of 0.4 plotted on both a logarithmic and linear scale. The normalization found for the predicted cross section for a cone size of 0.4 with the data was 0.723, just within the 33% normalization uncertainty on the data. Figure 56 shows the agreement between the next-to-leading order QCD calculation and the data for a cone size of 0.7 plotted on both a logarithmic and linear scale. The normalization found for the predicted cross section for a cone size of 0.7 with the data was 1.03, well within the 35% normalization uncertainty on the data. Figure 57 shows the agreement between the next-to-leading order QCD calculation and the data for a cone size of 1.0 plotted on both a logarithmic and linear scale. The normalization found for the predicted cross section for a cone size of 1.0 with the data was 1.07, again well within the 37% normalization uncertainty on the data.

Another feature of the next-to-leading order QCD calculations is the predicted variation in cross section as a function of jet clustering cone size. This was examined using cone sizes of 0.4, 0.7 and 1.0. Figure 58 shows the cross section for jets of E_t = 100 GeV measured in the data compared to what was calculated using next-to-leading order QCD as a function of the clustering cone size. Figure 58a was fit to $A + BLog(R)$, where R is the cone size. The result found $A = 0.7880 \pm 0.0224$ and $B = 0.4923 \pm 0.0264$ for a confidence level of 16.9%, using statistical errors only.

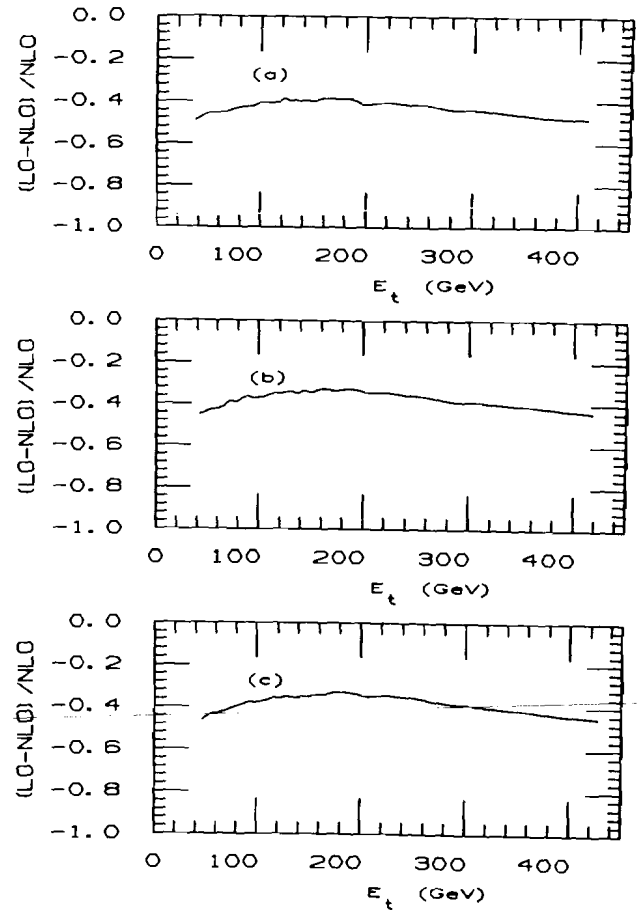

Figure 54. Comparison of next-to-leading order QCD and leading order QCD, using structure function MRS set B. Shown are comparisons for cone sizes of a) 0.4, b) 0.7 and c) 1.0. It should also be noted the curves were both normalized separately to the data before being compared.

Table XLI. Results of the comparison of next-to-leading order QCD calculations (using the structure function MRS B) of the inclusive jet cross section to the measured cross section. The χ^2's, number of bins and confidence levels calculated in each region for each cone size are listed.

	Cone Size 0.4			Cone Size 0.7			Cone Size 1.0		
Region	χ^2	NoB	C.L. (%)	χ^2	NoB	C.L. (%)	χ^2	NoB	C.L. (%)
Lower	6.95	10	73.1	11.59	7	11.5	9.90	6	12.9
Fit	8.60	14	80.2	10.70	15	70.9	9.68	14	71.9
Upper	10.65	15	77.7	17.06	16	38.2	23.67	16	9.7

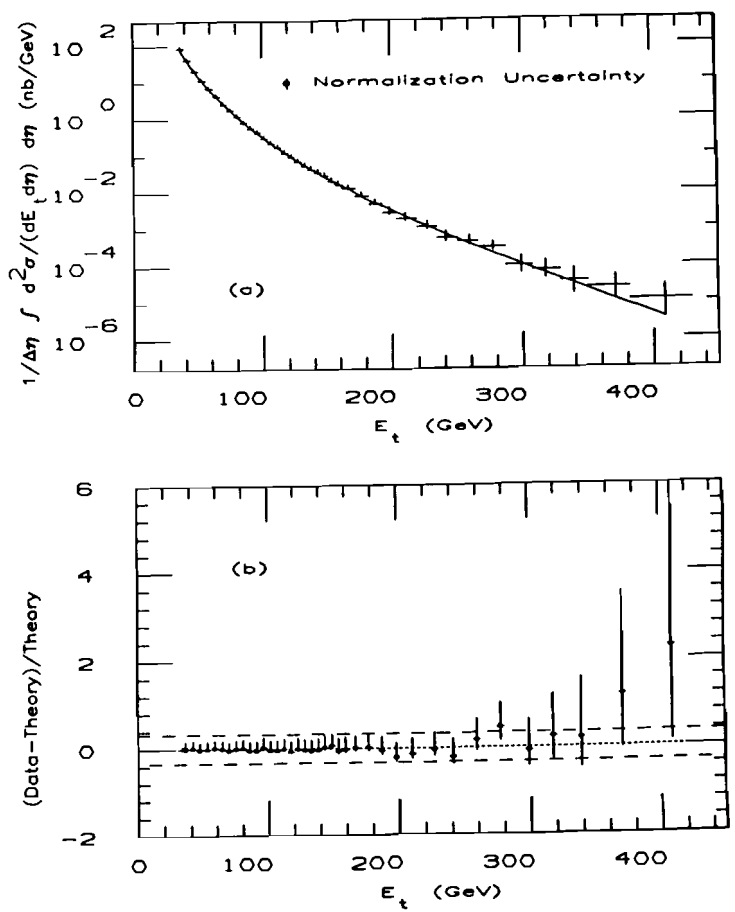

Figure 55. Next-to-leading order QCD calculation of the inclusive jet cross section compare to the measure cross section using the structure function MRS B for a cone size of 0.4. Shown is the a) cross section and b) fractional difference of data with theory.

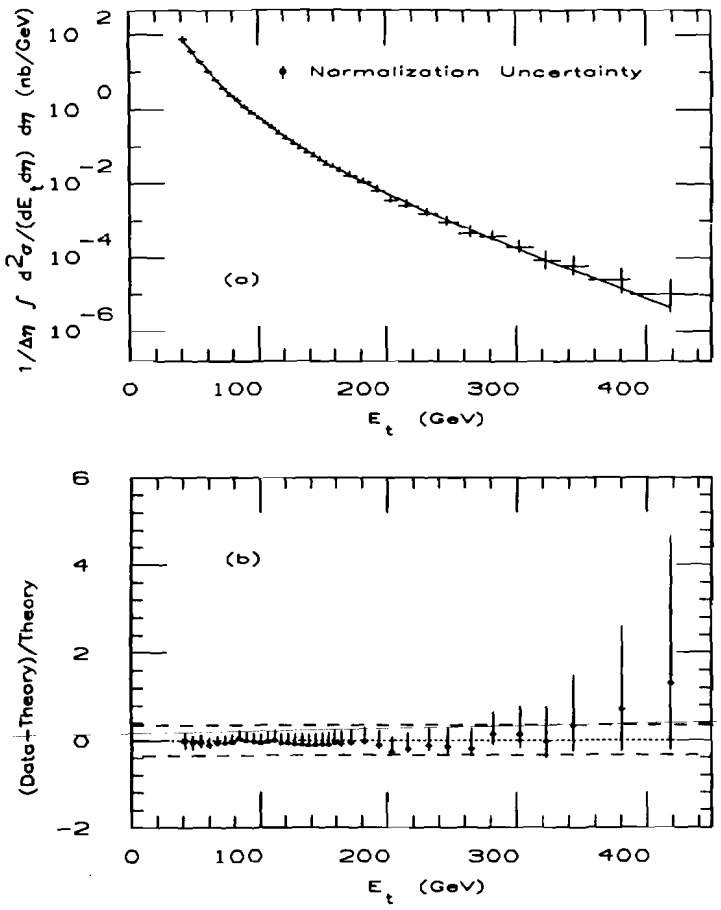

Figure 56. Next-to-leading order QCD calculation of the inclusive jet cross section compare to the measure cross section using the structure function MRS B for a cone size of 0.7. Shown is the a) cross section and b) fractional difference of data with theory.

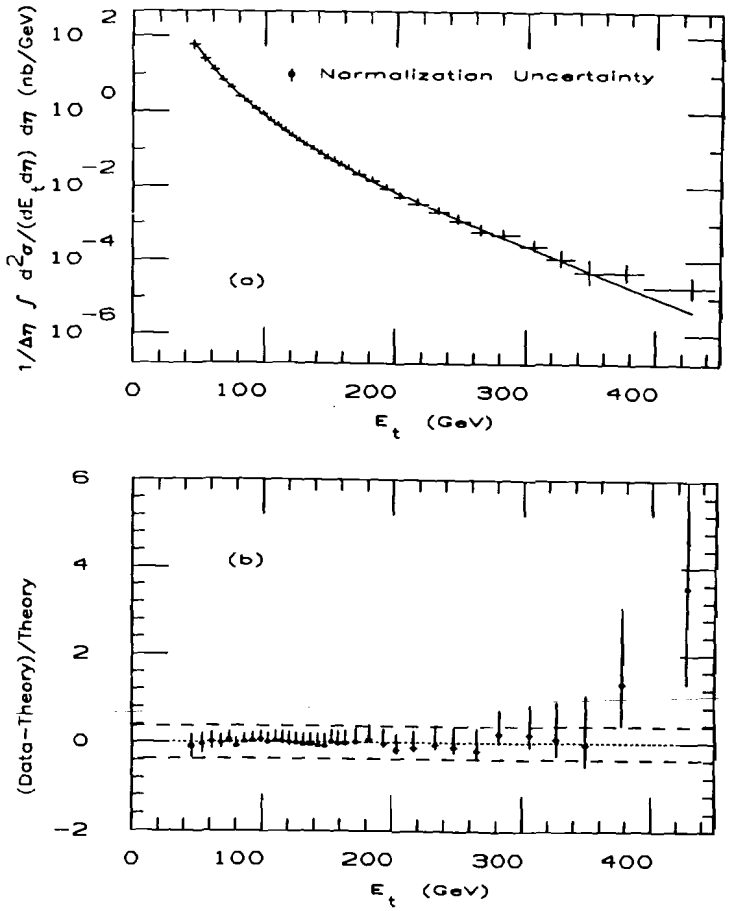

Figure 57. Next-to-leading order QCD calculation of the inclusive jet cross section compare to the measure cross section using the structure function MRS B for a cone size of 1.0. Shown is the a) cross section and b) fractional difference of data with theory.

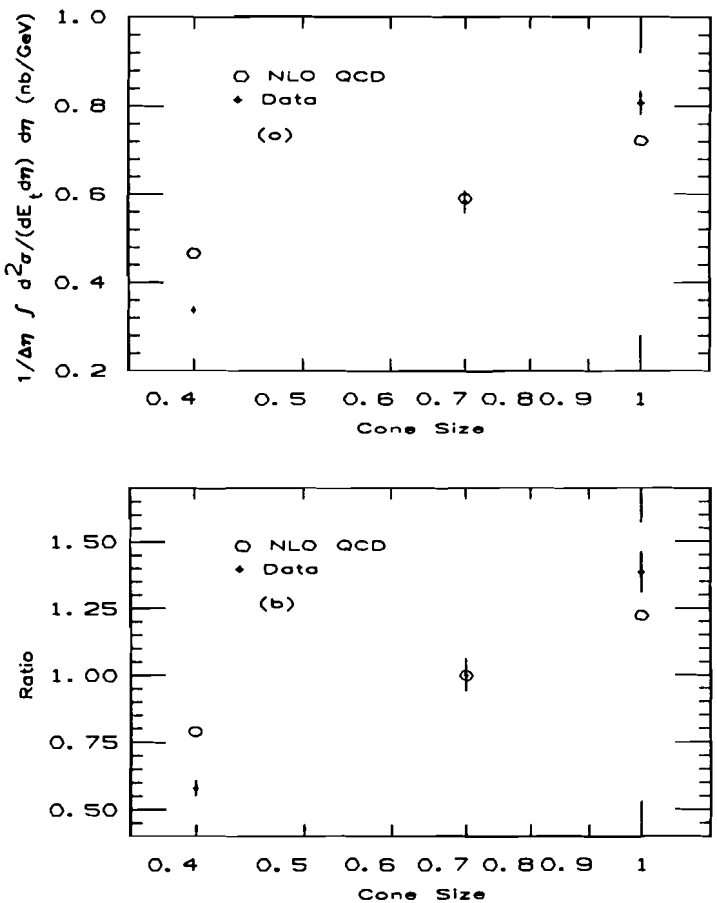

Figure 58. Next-to-leading order QCD calculation of the inclusive jet cross section compare to the measure cross section using the structure function MRS B for E_t = 100 GeV. Plotted as a function of jet cone size are the (statistical errors only are plotted) a) cross section and the b) ratio of the cross section for each cone size to the cross section for a cone size of 0.7.

CHAPTER VII

RESULTS AND CONCLUSIONS

The inclusive jet cross section has been measured using data collected by the CDF collaboration at $\sqrt{s} = 1.8$ TeV. This measurement was made using three cone sizes of 0.4, 0.7, and 1.0. The resulting cross section and both statistical and systematic uncertainties are listed in Tables XLII, XLIII, and XLIV for cone sizes of 0.4, 0.7, and 1.0 respectively. Figures 59, 60, and 61 are plots of the cross section together with the statistical and E_t dependent systematic uncertainties added in quadrature for cone sizes 0.4, 0.7, and 1.0 respectively. The normalization uncertainty plotted in these figures represents the size of the E_t independent systematic uncertainty.

The measured cross sections were compared to both leading order and next-to-leading order QCD and found to agree within the listed uncertainties. Although a slight excess of events above what is predicted by QCD was observed in the data, this excess was not statistically significant depending on the choice of structure function used. When comparing to next-to-leading order QCD, the dependence of the cross section as a function of cone size was also measured. The data were found to increase in cross section with larger cone size faster than next-to-leading order QCD predicted.

The cross section was also used to search for quark compositeness, and while no evidence for quark compositeness was found, a lower limit on the value of the compositeness scale parameter, Λ_c, was set at 1100 GeV at the 95% confidence level. This can be compared to the previous CDF result of $\Lambda_c > 700$ GeV.[26] A comparison can also be made to a limit of $\Lambda_c > 860$ GeV set in muon g-2 experiments which

assume that quarks and muons are composed of the same composite particles and that Λ_c is the same for all quarks and leptons.[89] The limit set in this dissertation greatly improves the existing limits from CDF and g-2 experiments. It should also be noted that the CDF ($p\bar{p}$) limits are less model dependent than the limits set from g-2 experiments.

Table XLII. Corrected jet cross section for a jet clustering cone size of 0.4.

Mean E_t (GeV)	Cross Section	± Statistical	± Systematic (nb/GeV)
36.24	86.9	±1.13	$^{+41.9}_{-32.1}$
41.90	42.1	±0.767	$^{+20.2}_{-14.9}$
47.52	20.9	±0.539	$^{+10.6}_{-7.52}$
53.27	11.7	±0.403	$^{+5.88}_{-4.01}$
59.01	6.96	±0.0950	$^{+3.43}_{-2.27}$
64.53	4.27	±0.0744	$^{+2.12}_{-1.38}$
69.85	2.63	±0.0585	$^{+1.38}_{-0.895}$
75.30	1.79	±0.0482	$^{+0.913}_{-0.591}$
80.62	1.22	±0.0398	$^{+0.624}_{-0.404}$
85.78	0.810	±0.0326	$^{+0.439}_{-0.284}$
91.12	0.571	±0.0275	$^{+0.312}_{-0.201}$
96.33	0.437	±0.0239	$^{+0.226}_{-0.145}$
101.64	0.294	±0.00370	$^{+0.165}_{-0.106}$
106.88	0.217	±0.00318	$^{+0.123}_{-0.0782}$
112.08	0.167	±0.00279	$^{+0.0925}_{-0.0586}$
117.30	0.117	±0.00234	$^{+0.0702}_{-0.0443}$
122.74	0.0915	±0.00207	$^{+0.0532}_{-0.0335}$
127.94	0.0691	±0.00180	$^{+0.0411}_{-0.0258}$
133.12	0.0526	±0.00157	$^{+0.0321}_{-0.0200}$
138.30	0.0420	±0.00141	$^{+0.0252}_{-0.0157}$
143.46	0.0348	±0.00128	$^{+0.0199}_{-0.0124}$
148.83	0.0285	±0.00116	$^{+0.0157}_{-0.00971}$
153.88	0.0200	±0.000974	$^{+0.0126}_{-0.00778}$

Table XLII. Continued

Mean E_t (GeV)	Cross Section	± Statistical	± Systematic (nb/GeV)
159.07	0.0161	±0.000875	$^{+0.0101}_{-0.00623}$
166.90	0.0129	±0.000555	$^{+0.00734}_{-0.00450}$
177.03	0.00803	±0.000439	$^{+0.00491}_{-0.00299}$
187.49	0.00485	±0.000342	$^{+0.00330}_{-0.00200}$
198.23	0.00277	±0.000258	$^{+0.00223}_{-0.00134}$
210.38	0.00190	±0.000175	$^{+0.00145}_{-0.000870}$
227.23	0.00114	±0.000136	$^{+0.000824}_{-0.000490}$
241.41	0.000570	±0.0000963	$^{+0.000523}_{-0.000309}$
259.30	0.000456	±0.0000862	$^{+0.000302}_{-0.000178}$
277.46	0.000320	±0.0000628	$^{+0.000178}_{-0.000104}$
299.20	0.0000985	$^{+0.0000487}_{-0.0000341}$	$^{+0.0000975}_{-0.0000564}$
317.64	0.0000737	$^{+0.0000442}_{-0.0000293}$	$^{+0.0000600}_{-0.0000345}$
338.92	0.0000368	$^{+0.0000359}_{-0.0000200}$	$^{+0.0000352}_{-0.0000201}$
371.08	0.0000247	$^{+0.0000241}_{-0.0000135}$	$^{+0.0000166}_{-0.00000938}$
409.19	0.0000111	$^{+0.0000147}_{-0.00000717}$	$^{+0.00000731}_{-0.00000409}$

Table XLIII. Corrected jet cross section for a jet clustering cone size of 0.7.

Mean E_t (GeV)	Cross Section	± Statistical	± Systematic (nb/GeV)
41.63	77.4	±1.08	$^{+40.6}_{-41.9}$
47.61	37.1	±0.715	$^{+19.9}_{-19.2}$
53.54	20.1	±0.520	$^{+10.6}_{-9.47}$
59.93	10.5	±0.373	$^{+5.73}_{-4.72}$
66.23	6.27	±0.286	$^{+3.30}_{-2.51}$
72.29	3.77	±0.0679	$^{+2.03}_{-1.43}$
78.15	2.49	±0.0550	$^{+1.32}_{-0.876}$
83.81	1.79	±0.0467	$^{+0.893}_{-0.578}$
89.30	1.17	±0.0378	$^{+0.624}_{-0.401}$
94.82	0.818	±0.0318	$^{+0.442}_{-0.283}$
100.19	0.574	±0.0267	$^{+0.321}_{-0.204}$
105.59	0.427	±0.0231	$^{+0.236}_{-0.149}$
111.04	0.321	±0.0200	$^{+0.175}_{-0.110}$
116.43	0.219	±0.00312	$^{+0.131}_{-0.0819}$
121.76	0.166	±0.00272	$^{+0.0996}_{-0.0620}$
127.12	0.122	±0.00233	$^{+0.0763}_{-0.0472}$
132.49	0.0926	±0.00204	$^{+0.0589}_{-0.0363}$
137.77	0.0712	±0.00179	$^{+0.0459}_{-0.0282}$
143.05	0.0552	±0.00158	$^{+0.0361}_{-0.0220}$
148.48	0.0440	±0.00141	$^{+0.0283}_{-0.0172}$
153.71	0.0344	±0.00125	$^{+0.0226}_{-0.0136}$
158.92	0.0283	±0.00114	$^{+0.0181}_{-0.0109}$
164.24	0.0219	±0.00100	$^{+0.0145}_{-0.00869}$

Table XLIII. Continued

Mean E_t (GeV)	Cross Section	± Statistical	± Systematic (nb/GeV)
171.89	0.0165	±0.000618	$^{+0.0106}_{-0.00634}$
182.20	0.0111	±0.000508	$^{+0.00711}_{-0.00421}$
193.03	0.00656	±0.000392	$^{+0.00473}_{-0.00278}$
203.47	0.00368	±0.000294	$^{+0.00324}_{-0.00189}$
215.73	0.00256	±0.000202	$^{+0.00211}_{-0.00122}$
231.87	0.00157	±0.000159	$^{+0.00123}_{-0.000703}$
246.86	0.000903	±0.000121	$^{+0.000759}_{-0.000431}$
264.86	0.000470	±0.0000872	$^{+0.000436}_{-0.000245}$
281.96	0.000381	±0.0000685	$^{+0.000264}_{-0.000147}$
302.21	0.000198	$^{+0.0000629}_{-0.0000490}$	$^{+0.000149}_{-0.0000821}$
322.87	0.0000867	$^{+0.0000468}_{-0.0000321}$	$^{+0.0000855}_{-0.0000467}$
343.87	0.0000621	$^{+0.0000422}_{-0.0000269}$	$^{+0.0000498}_{-0.0000270}$
380.71	0.0000252	$^{+0.0000246}_{-0.0000137}$	$^{+0.0000205}_{-0.0000109}$
418.54	0.0000104	$^{+0.0000137}_{-0.00000671}$	$^{+0.00000881}_{-0.00000464}$

Table XLIV. Corrected jet cross section for a jet clustering cone size of 1.0.

Mean E_t (GeV)	Cross Section	± Statistical	± Systematic (nb/GeV)
45.78	55.8	±1.14	$^{+38.8}_{-37.0}$
53.75	25.0	±0.687	$^{+15.9}_{-14.7}$
61.29	13.0	±0.462	$^{+7.49}_{-6.67}$
68.10	7.09	±0.323	$^{+4.06}_{-3.45}$
71.55	4.59	±0.253	$^{+2.39}_{-1.93}$
80.41	2.54	±0.0577	$^{+1.53}_{-1.17}$
86.48	1.82	±0.0487	$^{+1.00}_{-0.722}$
92.77	1.23	±0.0399	$^{+0.675}_{-0.452}$
98.70	0.872	±0.0335	$^{+0.473}_{-0.304}$
104.29	0.594	±0.0275	$^{+0.343}_{-0.218}$
109.90	0.443	±0.0237	$^{+0.252}_{-0.159}$
115.45	0.320	±0.0203	$^{+0.187}_{-0.117}$
120.89	0.234	±0.0173	$^{+0.142}_{-0.0879}$
126.24	0.174	±0.00281	$^{+0.108}_{-0.0668}$
131.64	0.128	±0.00242	$^{+0.0835}_{-0.0511}$
137.04	0.0995	±0.00213	$^{+0.0648}_{-0.0393}$
142.37	0.0747	±0.00185	$^{+0.0507}_{-0.0306}$
147.79	0.0576	±0.00163	$^{+0.0398}_{-0.0239}$
153.12	0.0496	±0.00151	$^{+0.0316}_{-0.0188}$
158.53	0.0373	±0.00131	$^{+0.0251}_{-0.0148}$
163.91	0.0299	±0.00118	$^{+0.0201}_{-0.0118}$
171.74	0.0218	±0.000714	$^{+0.0146}_{-0.00851}$
182.16	0.0149	±0.000592	$^{+0.00974}_{-0.00560}$

Table XLIV. Continued

Mean E_t (GeV)	Cross Section	± Statistical	± Systematic (nb/GeV)
193.07	0.00888	±0.000458	$^{+0.00646}_{-0.00367}$
203.44	0.00518	±0.000350	$^{+0.00444}_{-0.00250}$
216.42	0.00338	±0.000232	$^{+0.00283}_{-0.00157}$
233.06	0.00201	±0.000179	$^{+0.00163}_{-0.000887}$
247.46	0.00115	±0.000136	$^{+0.00103}_{-0.000555}$
264.64	0.000593	±0.0000975	$^{+0.000612}_{-0.000325}$
282.03	0.000496	±0.0000775	$^{+0.000370}_{-0.000194}$
305.43	0.000230	$^{+0.0000659}_{-0.0000523}$	$^{+0.000195}_{-0.000100}$
326.53	0.000108	$^{+0.0000497}_{-0.0000355}$	$^{+0.000113}_{-0.0000574}$
348.63	0.0000479	$^{+0.0000381}_{-0.0000230}$	$^{+0.0000663}_{-0.0000330}$
377.44	0.0000480	$^{+0.0000288}_{-0.0000191}$	$^{+0.0000345}_{-0.0000169}$
427.84	0.0000193	$^{+0.0000153}_{-0.00000925}$	$^{+0.0000125}_{-0.00000593}$

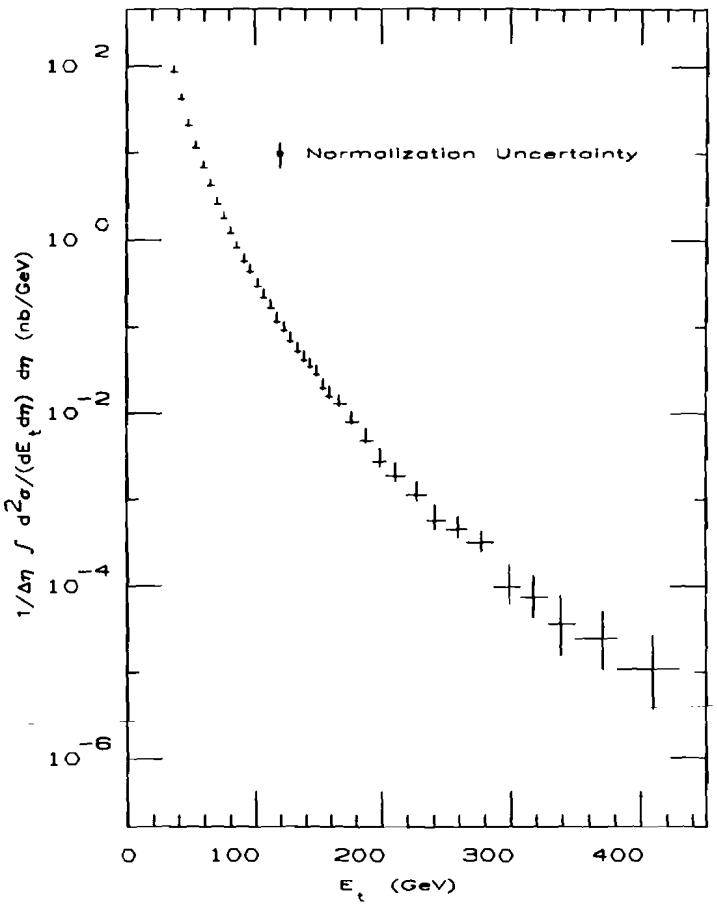

Figure 59. Inclusive jet cross section for a cone size of 0.4, normalization uncertainty is the E_t independent systematic uncertainty and the error bars represent the statistical uncertainty added in quadrature with the E_t dependent part of the systematic uncertainty.

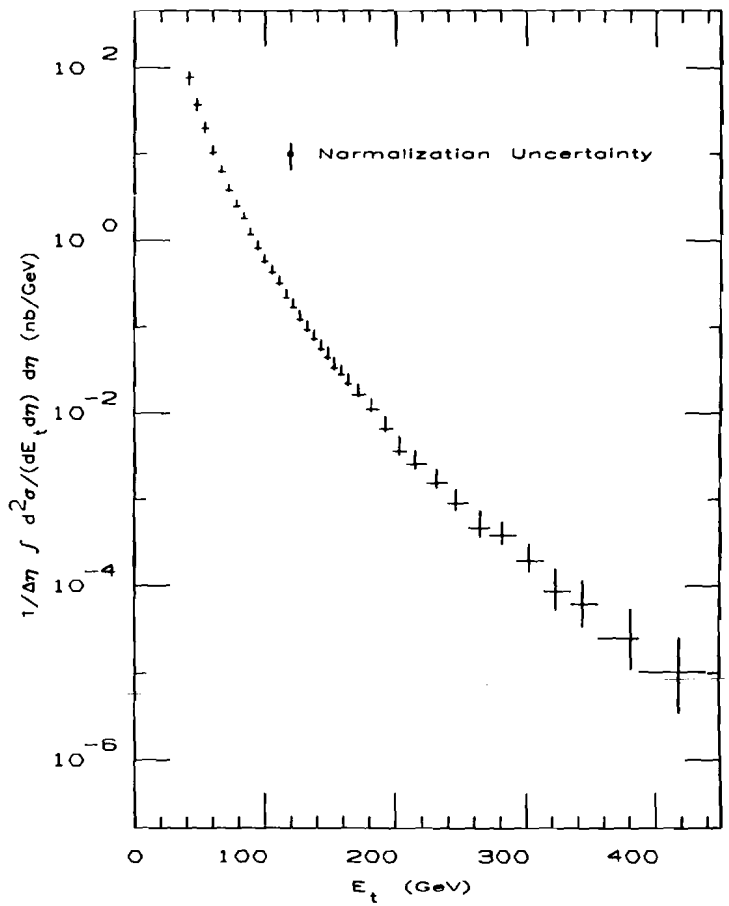

Figure 60. Inclusive jet cross section for a cone size of 0.7, normalization uncertainty is the E_t independent systematic uncertainty and the error bars represent the statistical uncertainty added in quadrature with the E_t dependent part of the systematic uncertainty.

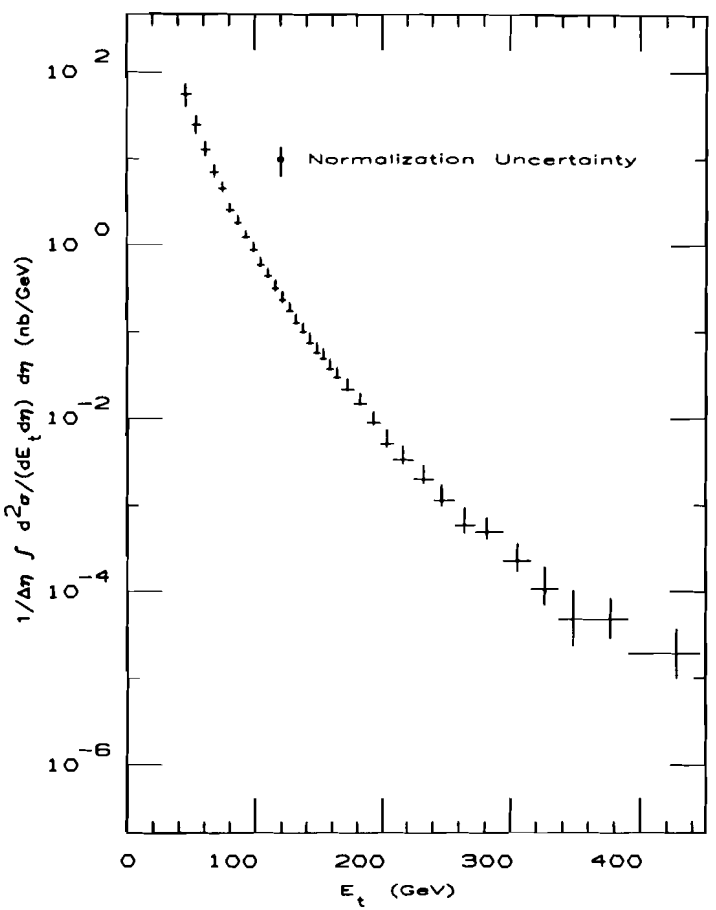

Figure 61. Inclusive jet cross section for a cone size of 1.0, normalization uncertainty is the E_t independent systematic uncertainty and the error bars represent the statistical uncertainty added in quadrature with the E_t dependent part of the systematic uncertainty.

REFERENCES

1 C. Sutton. *The Particle Connection*. Simon & Schuster, New York, 1984.

2 F. Close, M. Martin and C. Sutton. *The Particle Explosion*. Oxford University Press, New York, 1987.

3 Particle Data Group. Review of Particle Properties. Physics Letters, **204B**, April 1988.

4 V. Barger and R. Phillips. *Collider Physics*. Volume71 of *Frontiers in Physics*, Addison-Wesley Publishing Company, New York, 1987.

5 E. Eichten, I. Hinchliffe, K. Lane and C. Quigg. Supercollider Physics. Reviews of Modern Physics, **56**(4):579-707, October 1984.

6 F. Abe *et al.* (CDF Collaboration) Measurement of the Mass and Width of the Z^0 Boson at the Fermilab Tevatron. Physical Review Letters, **63**(7):720-723, August 1989.

7 G. S. Abrams *et al.* (Mark II Collaboration). Initial Measurements of Z-Boson Resonance Parameters in e^+e^- Annihilation, Physical Review Letters, **63**(7):724-727, August 1989.

8 B. Adeva *et al.* (L3 Collaboration). Determination of the Properties of the Neutral Intermediate Vector Boson Z^0. Physics Letters, **231B**:509, 1989.

9 D. Decamp *et al.* (ALEPH Collaboration). Determination of the Number of Light Neutrino Species. Physics Letters, **231B**:519, 1989.

10 M. Akrawy *et al.* (OPAL Collaboration). Measurement of the Z^0 Mass and Width with the OPAL Detector at LEP. Physics Letters, **231B**:530, 1989.

11 P. Aarnio *et al.* (DELPHI Collaboration). The Mass and Width of the Z^0-Particle from Multihadronic Final States Produced in e^+e^- Annihilations. Physics Letters, **231B**:539, 1989.

12 F. Abe *et al.* (CDF Collaboration). A Search for the Top Quark in the Reaction $\bar{p}p \rightarrow$ Electron + Jets at $\sqrt{s} = 1.8$ TeV. Physical Review Letters, **64**(2):142, January 1990.

13 F. Abe *et al.* (CDF Collaboration). Search for New Heavy Quarks in Electron-Muon Events at the Fermilab Tevatron Collider. Physical Review Letters, **64**(2):147 January 1990.

14 F. Abe *et al.* (CDF Collaboration). Search for the Top Quark at CDF. To be published in the proceedings of the PANIC XII, International Conference on Particles and Nuclei, Massachusetts Institute of Technology, Cambridge, Massachusetts, June 1990.

15 I. Aitchison and A. Hey. *Gauge Theories in Particle Physics. Graduate Student Series in Physics*, Adam Hilger, Philadelphia, 2nd edition, 1989.

16 D. Perkins. *Introduction to High Energy Physics*. Addison-Wesley Publishing Company Inc., Reading Massachusetts, 3rd edition, 1987.

17 F. Halzen and A. Martin. *Quarks & Leptons: An Introductory Course in Modern Particle Physics*. John Wiley & Sons, New York, 1984.

18 T. Bowcock *et al.* (CLEO Collaboration). Search for Fractionally Charged Particles in e^+e^- Annihilations at $\sqrt{s} = 10.5$ GeV. Physical Review, **D40**:263, 1989.

19 E. Eichten, K. Lane and M. Peskin. New Tests for Quark and Lepton Substructure. Physical Review Letters, **50**(11):811-814, March 1983.

20 S. Ellis, Z. Kunszt and D. Soper. One-Jet Inclusive Cross Section at Order α^3: Gluons Only. Physical Review Letters, **62**(7):726-729, February 1989.

21 S. Ellis, Z. Kunszt and D. Soper. One-Jet Inclusive Cross Section at Order α_s^3: Quarks and Gluons. Physical Review Letters, **64**(18):2121, April 1990.

22 F. Aversa, M. Greco, P. Chiappetta and J. Ph. Guillet. LNF-90/012 PT (1990), Submitted to Physical Review Letters.

23 T. Åkesson *et al.* (Axial Field Spectrometer Collaboration). The Jet Cross Section in pp Interactions at $\sqrt{s} = 45$ GeV and It's $\sqrt{s}$ Dependence. Physical Letters, **123B**(1,2):133-138, March 1983.

24 G. Arnison *et al.* (UA1 collaboration). Measurement of the Inclusive Jet Cross Section at the CERN $p\bar{p}$ Collider. Physical Letters, **172B**(3,4):461, 1986.

25 P. Bagnaia *et al.* (UA2 Collaboration). Measurement of Very Large Transverse Momentum Jet Production at the CERN $\bar{p}p$ Collider. Physical Letters, **138B**(5,6):430-440, April 1984.

26 F. Abe *et al.* (CDF collaboration). Measurement of the Inclusive Jet Cross Section in $\bar{p}p$ Collisions at $\sqrt{s} = 1.8$ TeV. Physical Review Letters, **62**(6):613-616, February 1989.

27 E. Eichten, I. Hinchliffe, K. Lane and C. Quigg. Supercollider Physics. Reviews of Modern Physics, **56**(4):579, October 1984.

28 R. Ellis and J. Sexton. QCD Radiative Corrections to Parton-Parton Scattering. Nuclear Physics, **B269**:445–484, 1986.

29 F. Abe *et al.* (CDF collaboration). The CDF Detector: An Overview. Nuclear Instruments and Methods in Physics Research, **A271**:387–403, 1988.

30 F. Snider *et al.*. The CDF Vertex Time Projection Chamber System. Nuclear Instruments and Methods in Physics Research, **A268**:75–91, 1988.

31 F. Bedeschi *et al.*. Design and Construction of the CDF Central Tracking Chamber. Nuclear Instruments and Methods in Physics Research, **A268**:50–74, 1988.

32 S. Bhadra *et al.*. The Design and Construction of the CDF Central Drift Tube Array. Nuclear Instruments and Methods in Physics Research, **A268**:92–104, 1988.

33 M. Atac *et al.*. Radial Wire Drift Chambers for the CDF Forward Tracking. Nuclear Instruments and Methods in Physics Research, **A269**:40–50, 1988.

34 L. Balka *et al.*. The CDF Central Electromagnetic Calorimeter. Nuclear Instruments and Methods in Physics Research, **A267**:272–279, 1988.

35 S. Bertolucci *et al.*. The CDF Central and Endwall Hadron Calorimeter. Nuclear Instruments and Methods in Physics Research, **A267**:301–314, 1988.

36 Y. Fukui *et al.*. CDF End Plug Electromagnetic Calorimeter Using Conductive Plastic Proportional Tubes. Nuclear Instruments and Methods in Physics Research, **A267**:280–300, 1988.

37 W. C. Carithers *et al.*. *Performance and Calibration Studies of the CDF Endplug Calorimeter.* In the proceedings of the Gas Sampling Calorimeter Workshop II, Fermilab, 1985.

38 G. Bradenburg *et al.*. An Electromagnetic Calorimeter for the Small Angle Regions of the Collider Detector at Fermilab. Nuclear Instruments and Methods in Physics Research, **A267**:257–271, 1988.

39 S. Cihangir *et al.*. The CDF Forward/Backward Hadron Calorimeter. Nuclear Instruments and Methods in Physics Research, **A267**:249–256, 1988.

40 G. Ascoli *et al.*. CDF Central Muon Detector. Nuclear Instruments and Methods in Physics Research, **A268**:33–40, 1988.

41 K. Byrum *et al.*. The CDF Forward Muon System. Nuclear Instruments and Methods in Physics Research, **A268**:46–49, 1988.

42 G. Drake *et al.*. CDF Front End Electronics: The RABBIT System. Nuclear Instruments and Methods in Physics Research, **A269**:68–81, 1988.

43 E. Barsotti *et al.*. FASTBUS Data Acquisition for CDF. Nuclear Instruments and Methods in Physics Research, **A269**:82–92, 1988.

44 D. Amidei *et al.*. A Two Level FASTBUS Based Trigger System for CDF. Nuclear Instruments and Methods in Physics Research, **A269**:51–62, 1988.

45 D. Amidei *et al.*. A Two Level FASTBUS Based Trigger System for CDF. Nuclear Instruments and Methods in Physics Research, **A269**:51–62, 1988.

46 J. A. Appel *et al.* (UA2 Collaboration). Measurement of the $\sqrt{s}$ Dependence of Jet Production at the CERN $\bar{p}p$ Collider. Physical Letters, **160B**:349, October 1990.

47 D. Brown *et al.*. *Clustering Algorithms and Their Performance.* CDF Note 605, Collider Detector at Fermilab, Batavia, Illinois, February 1988.

48 J. Hauser. *Guide to the Triggers Used in the 1988-1989 CDF Data Run.* CDF Note 966, Collider Detector at Fermilab, Batavia, Illinois, June 1989.

49 T. Carroll *et al.*. *The CDF LEVEL3 Trigger.* Talk presented at Workshop on Triggering and Data Acquisition for Experiments at the Superconducting Super Collider in Toronto Canada. CDF Note 895, Collider Detector at Fermilab, Batavia, Illinois, January 1989.

50 S. Cihangir *et al.*. *Neutron Induced Pulses in CDF Forward Hadron Calorimeter.* Submitted to IEEE Symposium in Orlando, Florida November 9–11, 1988. CDF Note 810, Collider Detector at Fermilab, Batavia, Illinois, November 1988.

51 W. Trischuk and L. Nodulman. *1988-89 Missing E_t Centering and Resolution.* CDF Note 948, Collider Detector at Fermilab, Batavia, Illinois, June 1989.

52 W. Trischuk, L. Nodulman and P. Hu. *The Tail of the MET Spin.* CDF Note 962, Collider Detector at Fermilab, Batavia, Illinois, June 1989.

53 D. Brown and M. Franklin. *FILTGAS*. CDF Note 811, Collider Detector at Fermilab, Batavia, Illinois, November 1988.

54 P. Hurst and M. Franklin. *Cable Noise Filter Description: PHA*. CDF Note 847, Collider Detector at Fermilab, Batavia, Illinois, December 1988.

55 P. Hurst, M. Franklin and T. Kamon. *Cable Noise Filter Description: FHA*. CDF Note 848, Collider Detector at Fermilab, Batavia, Illinois, December 1988.

56 T. Kamon, P. Hurst, M. Franklin and Y. Funayama. *Description of FHANCABLE*. CDF Note 900, Collider Detector at Fermilab, Batavia, Illinois, March 1989.

57 G. Redlinger and Y. D. Tsai. *The Hadron TDC Filter for Main Ring and Cosmic Ray Events*. CDF Note 521, Collider Detector at Fermilab, Batavia, Illinois, June 1987.

58 S. Kuhlmann and J. Yoh. *Filtering Jet Backgrounds in the CDF Central Detector*. CDF Note 548, Collider Detector at Fermilab, Batavia, Illinois, August 1987.

59 T. Hessing. *Filtering Central Jet Backgrounds in the 1988-1989 Data*. CDF Note 957, Collider Detector at Fermilab, Batavia, Illinois, June 1989.

60 T. Kamon. *Cosmic Ray Muon Background to Missing E_t Physics at the CDF - Rate Estimate for 1988-89 Data -*. CDF Note 979, Collider Detector at Fermilab, Batavia, Illinois, July 1989.

61 S. Kuhlmann. *Acceptance Issues for the Inclusive Jet Cross Section*. CDF Note 711, Collider Detector at Fermilab, Batavia, Illinois, July 1988.

62 S. Kuhlmann. *Inclusive Central Jet Production at $\sqrt{s}$ = 1.8 TeV*. Ph.D. Thesis, Purdue University, August 1988.

63 S. Kuhlmann. *Steps in Deriving the Inclusive Jet Cross Section*. CDF Note 709, Collider Detector at Fermilab, Batavia, Illinois, July 1988.

64 J. Huth and S. Behrends. *Statistical Issues for the Inclusive Jet E_t Paper*. CDF Note 747, Collider Detector at Fermilab, Batavia, Illinois, September 1988.

65 S. Behrends, M. D. Shapiro, and E. Pare. *Single Pion Response in the Central Calorimeter*. CDF Note 1066, Collider Detector at Fermilab, Batavia, Illinois, November 1989.

66 D. Brown, S. Kannappan, and M. D. Shapiro. *Single Pion Response in the Central Calorimeter*. CDF Note 753, Collider Detector at Fermilab, Batavia, Illinois, October 1988.

67 T. Hessing, S. Behrends, P. Tipton, and B. Winer. *Monte Carlo Fragmentation Tuning for Jet Energy and Resolution Analysis*. CDF Note 1131, Collider Detector at Fermilab, Batavia, Illinois, February 1990.

68 R. P. Feynman and R. D. Field. A Parameterization of the Properties of Quark Jets. Nuclear Physics, **B136**:1, 1978.

69 D. Brown and S. Kannappan. *SETPRT, a Single Parton Fragmentation Module*. CDF Note 873, Collider Detector at Fermilab, Batavia, Illinois, February 1989.

70 T. Hessing and S. Behrends. *Inclusive Jet E_t Spectrum: Energy Corrections and Resolution Unsmearing*. CDF Note 1132, Collider Detector at Fermilab, Batavia, Illinois, March 1990.

71 R. St. Denis. *Implications for the Top in Low Energy Jets from Gamma-Jet Events*. CDF Note 894, Collider Detector at Fermilab, Batavia, Illinois, March 1989.

72 S. Kuhlmann *et al.*. *Central Jet Energy/Momentum Corrections*. CDF Note 686, Collider Detector at Fermilab, Batavia, Illinois, July 1988.

73 P. Bagnaia *et al.* (UA2 collaboration). Measurement of Jet Production Properties at the CERN $p\bar{p}$ Collider. Physical Letters, **144B**:283, 1984.

74 P. Bagnaia *et al.* (UA2 collaboration). Measurement of Production and Properties of Jets at the CERN $p\bar{p}$ Collider. *Zeitschrift für Physik*, **C20**:117, 1983.

75 R. St. Denis. *Dijet Angular Distributions in Proton-Antiproton Collisions at the Fermilab Tevatron*. Ph.D. Thesis, Harvard University, December 1988.

76 R. Harris. *Two Jet Differential Cross Section and Structure Functions in $\bar{p}p$ Collisions at $\sqrt{s}$ = 1.8 TeV*. Ph.D. Thesis, University of California at Berkeley, August 1989.

77 R. M. Harris. *Unsmearing the Single Jet Inclusive Distribution*. CDF Note 606, Collider Detector at Fermilab, Batavia, Illinois, June 1988.

78 S. Behrends, and S. Kuhlmann. *Checks of the CDFSIM Central Calorimeter Simulation.* CDF Note 684, Collider Detector at Fermilab, Batavia, Illinois, May 1988.

79 B. Flaugher and S. Kuhlmann. *Underlying Event Energy in Clusters.* CDF Note 685, Collider Detector at Fermilab, Batavia, Illinois, May 1988.

80 R. Ansourge *et al.* (UA5 Collaboration). Diffraction Dissociation at the CERN Pulsed $p\bar{p}$ Collider at c.m. Energies of 900 and 200 GeV. *Zeitschrift für Physik*, **C33**:175, 1986.

81 G. Alner *et al.* (UA5 Collaboration). Antiproton-Proton Cross Sections at 200 and 900 GeV c.m. Energy. *Zeitschrift für Physik*, **C32**:153, 1986.

82 M. Bozzo *et al.* (UA4 Collaboration). Measurements of the Proton-Antiproton Total and Elastic Cross Sections at the CERN SPS Collider. Physics Letters, **147B**:392, 1984.

83 Carla Grosso-Pilcher and S. White. *CDF Luminosity Calibration.* CDF Note 1202, Collider Detector at Fermilab, Batavia, Illinois, August 1990.

84 Data exists from several deep inelastic electron, muon, and neutrino experiments the list includes: SLAC-MIT Collaboration electron scattering measurements, European Muon Collaboration (EMC) muon measurements, Big European Bubble Chamber (BEBC) Collaboration, CERN-Dortmund-Heidelberg-Sacaly (CDHA) Collaboration and, CHARM Collaboration neutrino measurements, as well as data from the BCDMS Collaboration, the CCFRR Collaboration.

85 D. Duke and J. Owens. Q^2-dependent Parameterizations of Parton Distribution Functions. Physical Review, **D30**(1):49, July 1984.

86 M. Diemoz, F. Ferroni, E. Longo and G. Martinelli. Parton Densities from Deep Inelastic Scattering to Hadronic Process at Super Collider Energies. *Zeitschrift für Physik*, **C39**:21-37, 1988.

87 A. Martin, R. Roberts, and W. Stirling. Structure-function Analysis and ψ, Jet, W, and Z Production: Determining the Gluon Distribution. Physical Review, **D37**:1161, 1988.

88 W. Tung, *et al.*. Fermilab Preprint. Fermilab-Pub-90/24, 1990.

89 M. Abolins *et al.*. *Testing the Compositeness of Quarks and Leptons.* In the proceedings of the 1982 DPF Summer Study on Elementary Particle Physics and Future Facilities, 1982.

APPENDIX A

DIJET BALANCING

Dijet balancing is a technique first introduced by the UA2 collaboration[73, 74] and has been used extensively in jet measurements at CDF.[75, 76] A dijet event is defined by the observation in the detector of two jets which originate from the scattering partons in the $p\bar{p}$ collision. Dijet $\vec{k_t}$ is defined as the vector sum of the transverse momentum of these jets. In the absence of initial state radiation, conservation of momentum requires the total transverse momentum (P_T) of the scattered jets in the event to be conserved. In dijet events, this implies that $\vec{k_t}$ is expected to be zero. Detector resolution and QCD bremsstrahlung produce a momentum imbalance in the event and the $\vec{k_t}$ is not zero.

A. Dijet $\vec{k_t}$

The coordinate system for dijet $\vec{k_t}$ is defined so that the perpendicular ($\hat{\perp}$) direction is the direction that bisects the azimuthal angle between the two jets, and the parallel ($\hat{\parallel}$) direction is the orthogonal direction such that $\hat{\parallel} \times \hat{\perp} = \hat{z}$, where $\hat{z}$ is defined to be the positive z-axis in the detector coordinate system. Figure 62 shows an example of $\vec{k_t}$ for a two jet event.

Defining the coordinate system in this ways implies,

$$k_{t_\perp} = (P_{t_1} + P_{t_2}) \cos \frac{\phi_{12}}{2}, \tag{48}$$

$$k_{t_\parallel} = (P_{t_1} - P_{t_2}) \sin \frac{\phi_{12}}{2}, \tag{49}$$

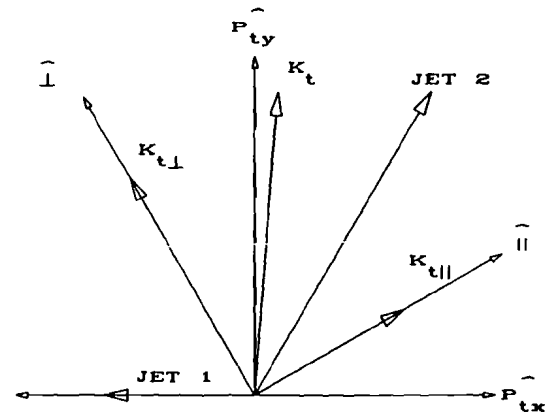

Figure 62. Illustration of dijet $\vec{k_t}$ coordinate system.

where ϕ_{12} is the azimuthal angle separating the two jets and P_{t_i} is the magnitude of the P_t for jet i (i = 1 or 2). E_t is related to P_t by

$$E_t^2 = P_t^2 + m^2, \tag{50}$$

where m is the mass of the jet. The sum or difference in E_t for two jets therefore is

$$\begin{aligned} E_{t_1} \pm E_{t_2} &= \sqrt{P_{t_1}^2 + m_1^2} \pm \sqrt{P_{t_2}^2 + m_2^2}, \\ &= P_{t_1}\sqrt{1 + \frac{m_1^2}{P_{t_1}^2}} \pm P_{t_2}\sqrt{1 + \frac{m_2^2}{P_{t_2}^2}}, \\ &\simeq P_{t_1}(1 + \frac{m_1^2}{2P_{t_1}^2}) \pm P_{t_2}(1 + \frac{m_2^2}{2P_{t_2}^2}) + O(\frac{m^4}{P_t^4}), \\ &= P_{t_1} \pm P_{t_2} + (\frac{m_1^2}{2P_{t_1}^2} \pm \frac{m_2^2}{2P_{t_2}^2}) + O(\frac{m^4}{P_t^4}). \end{aligned} \tag{51}$$

The ratio of jet mass to jet P_t is small,[75] therefore from Equation 51,

$$E_{t_1} \pm E_{t_2} \simeq P_{t_1} \pm P_{t_2}. \tag{52}$$

Hence,

$$k_{t_\perp} = (E_{t_1} + E_{t_2}) \cos \frac{\phi_{12}}{2}, \tag{53}$$

and

$$k_{t_\parallel} = (E_{t_1} - E_{t_2}) \sin \frac{\phi_{12}}{2}. \tag{54}$$

Angular deviations in the measurements of these two jets can be observed in the perpendicular component of dijet $\vec{k_t}$ ($k_{t_\perp}$). E_t imbalance in the dijet system is observed in the measurement of the parallel component of dijet $\vec{k_t}$ ($k_{t_\parallel}$).

B. Jet Resolution

The jet energy resolution in the calorimeter can be parameterized [3] as,

$$\frac{\sigma(E)}{E} = \frac{A}{\sqrt{(E)}}. \tag{55}$$

$E_t = E \sin \theta$, where θ is the angle of the jet with respect to the proton beam direction ($\hat{z}$ or the polar angle). In the central region of the CDF detector $\sin \theta \sim 1$, therefore $E_t \simeq E$ and the jet E_t resolution can be written as

$$\frac{\sigma(E_t)}{E_t} = \frac{A}{\sqrt{E_t}}, \tag{56}$$

or

$$\sigma(E_t) = A\sqrt{E_t}. \tag{57}$$

Assuming independent errors on the resolution for the two jets, then

$$\sigma(E_{t_1} - E_{t_2}) = \sqrt{\sigma^2(E_{t_1}) + \sigma^2(E_{t_2})}. \tag{58}$$

The value of A in Equation 57 should be the same for both jets if they are in the central calorimeter and $E_{t_1} \sim E_{t_2} \equiv E_t$, therefore

$$\sigma(E_{t_1} - E_{t_2}) = A\sqrt{2E_t}, \tag{59}$$

$$\frac{\sigma(E_{t_1} - E_{t_2})}{\sqrt{2}} = \sigma(E_t). \tag{60}$$

The effects of QCD radiation and angular mismeasurement are present in both $k_{t_\perp}$ and $k_{t_\parallel}$; however, as can be seen in Figure 63, the distribution of $k_{t_\perp}$ is flat (constant in E_t) while there is an E_t dependence to $k_{t_\parallel}$ due to the jet E_t resolution. Therefore, by subtracting $\sigma(k_{t_\perp})$ in quadrature from $\sigma(k_{t_\parallel})$, the jet E_t resolution can be isolated from these effects.[75] Defining,

$$\sigma'(k_t) = \sqrt{\sigma^2(k_{t_\parallel}) - \sigma^2(k_{t_\perp})},$$

and since $\sigma(k_{t_\parallel})$ is equivalent to $\sigma(E_{t_1} - E_{t_2})$, then

$$\sigma(E_{t_1} - E_{t_2}) \approx \sigma'(k_t), \tag{61}$$

or

$$\sigma(E_t) \approx \frac{\sigma'(k_t)}{\sqrt{2}}. \tag{62}$$

Thus, by using dijet $\vec{k_t}$ balancing techniques, single jet E_t resolution can be extracted from the data.

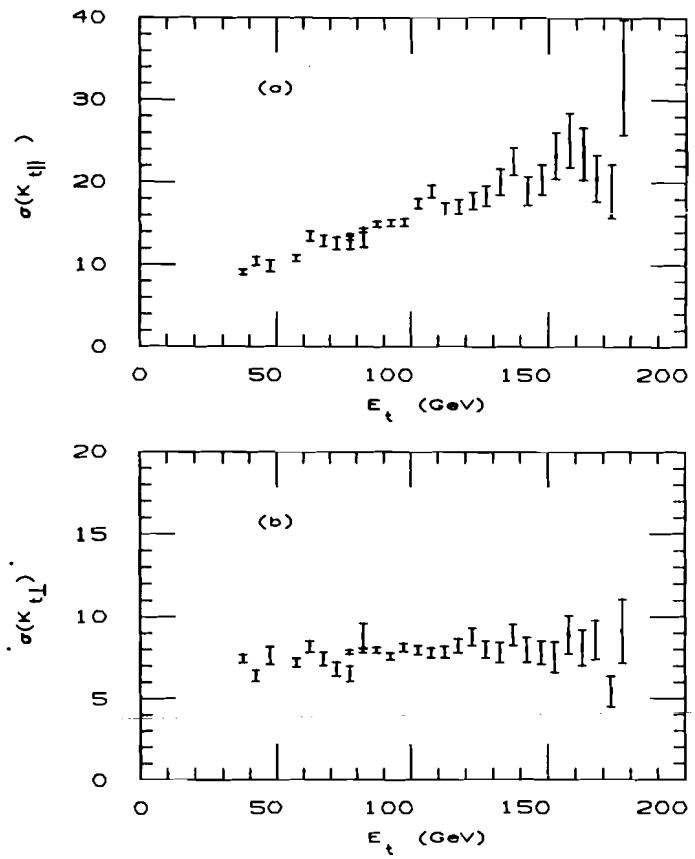

Figure 63. Dijet $\vec{k_t}$ distributions. a) $k_{t_\perp}$ and b) $k_{t_\parallel}$.

APPENDIX B

THE CDF COLLABORATION

F. Abe,[8] D. Amidei,[4] G. Apollinari,[11] M. Atac,[4] P. Auchincloss,[14]
A. R. Baden,[6] A. Bamberger,[19] A. Barbaro-Galtieri,[9] V. E. Barnes,[12]
F. Bedeschi,[11] S. Behrends,[2] S. Belforte,[11] G. Bellettini,[11] J. Bellinger,[18]
J. Bensinger,[2] A. Beretvas,[4] J. P. Berge,[4] S. Bertolucci,[5] S. Bhadra,[7]
M. Binkley,[4] R. Blair,[1] C. Blocker,[2] A. W. Booth,[4] T. Bowcock,[15]
G. Brandenburg,[6] D. Brown,[6] E. Buckley,[14] A. Byon,[12] K. L. Byrum,[18]
C. Campagnari,[3] M. Campbell,[3] R. Carey,[6] W. Carithers,[9] D. Carlsmith,[18]
J. T. Carroll,[4] R. Cashmore,[19] F. Cervelli,[11] K. Chadwick,[4] G. Chiarelli,[5]
W. Chinowsky,[9] S. Cihangir,[4] A. G. Clark,[4] D. Connor,[10] M. Contreras,[2]
J. Cooper,[4] M. Cordelli,[5] D. Crane,[4] M. Curatolo,[5] C. Day,[4] S. Dell'Agnello,[11]
M. Dell'Orso,[11] L. Demortier,[2] P. F. Derwent,[3] T. Devlin,[14] D. DiBitonto,[15]
R. B. Drucker,[9] J. E. Elias,[4] R. Ely,[9] S. Errede,[7] B. Esposito,[5]
B. Flaugher,[14] G. W. Foster,[4] M. Franklin,[6] J. Freeman,[4] H. Frisch,[3]
Y. Fukui,[8] Y. Funayama,[16] A. F. Garfinkel,[12] A. Gauthier,[7] S. Geer,[6]
P. Giannetti,[11] N. Giokaris,[13] P. Giromini,[5] L. Gladney,[10] M. Gold,[9]
K. Goulianos,[13] H. Grassmann,[11] C. Grosso-Pilcher,[3] C. Haber,[9] S. R. Hahn,[4]
R. Handler,[18] K. Hara,[16] R. M. Harris,[9] J. Hauser,[3] C. Hawk,[14] T. Hessing,[15]
R. Hollebeek,[10] L. Holloway,[7] P. Hu,[14] B. Hubbard,[9] B. T. Huffman,[12]
R. Hughes,[10] P. Hurst,[7] J. Huth,[4] M. Incagli,[11] T. Ino,[16] H. Iso,[16]
H. Jensen,[4] C. P. Jessop,[6] R. P. Johnson,[4] U. Joshi,[4] R. W. Kadel,[4]

T. Kamon,[15] S. Kanda,[16] D. A. Kardelis,[7] I. Karliner,[7] E. Kearns,[6]
R. Kephart,[4] P. Kesten,[2] R. M. Keup,[7] H. Keutelian,[7] S. Kim,[16]
L. Kirsch,[2] K. Kondo,[16] S. E. Kuhlmann,[1] E. Kuns,[14] A. T. Laasanen,[12]
J. I. Lamoureux,[18] W. Li,[1] T. M. Liss,[7] N. Lockyer,[10] C. B. Luchini,[7]
P. Maas,[4] M. Mangano[11] J. P. Marriner,[4] R. Markeloff,[18] L. A. Markosky,[18]
R. Mattingly,[2] P. McIntyre,[15] A. Menzione,[11] T. Meyer,[15] S. Mikamo,[8]
M. Miller,[3] T. Mimashi,[16] S. Miscetti,[5] M. Mishina,[8] S. Miyashita,[16]
Y. Morita,[16] S. Moulding,[2] A. Mukherjee,[4] L. F. Nakae,[2] I. Nakano,[16]
C. Nelson,[4] C. Newman-Holmes,[4] J. S. T. Ng,[6] M. Ninomiya,[16] L. Nodulman,[1]
S. Ogawa,[16] R. Paoletti,[11] A. Para,[4] E. Pare,[6] J. Patrick,[4] T. J. Phillips,[6]
R. Plunkett,[4] L. Pondrom,[18] J. Proudfoot,[1] G. Punzi,[11] D. Quarrie,[4]
K. Ragan,[10] G. Redlinger,[3] J. Rhoades,[18] M. Roach,[17] F. Rimondi,[19]
L. Ristori,[11] T. Rohaly,[10] A. Roodman,[3] A. Sansoni,[5] R. D. Sard,[7] A. Savoy-Navarro,[4] V. Scarpine,[7] P. Schlabach,[7] E. E. Schmidt,[4] M. H. Schub,[12]
R. Schwitters,[6] A. Scribano,[11] S. Segler,[4] Y. Seiya,[16] M. Sekiguchi,[16]
P. Sestini,[11] M. Shapiro,[6] M. Sheaff,[18] M. Shochet,[3] J. Siegrist,[9] P. Sinervo,[10]
J. Skarha,[18] K. Sliwa,[17] D. A. Smith,[11] F. D. Snider,[3] R. St. Denis,[6]
A. Stefanini,[11] R. L. Swartz, Jr.,[7] M. Takano,[16] K. Takikawa,[16] S. Tarem,[2]
D. Theriot,[4] M. Timko,[15] P. Tipton,[9] S. Tkaczyk,[4] A. Tollestrup,[4]
G. Tonelli,[11] J. Tonnison,[12] W. Trischuk,[6] Y. Tsay,[3] F. Ukegawa,[16]
D. Underwood,[1] R. Vidal,[4] R. G. Wagner,[1] R. L. Wagner,[4] J. Walsh,[10]
T. Watts,[14] R. Webb,[15] C. Wendt,[18] W. C. Wester, III,[9] T. Westhusing,[11]

S. N. White,[13] A. B. Wicklund,[1] H. H. Williams,[10] B. L. Winer,[9] A. Yagil,[4]
A. Yamashita,[16] K. Yasuoka,[16] G. P. Yeh,[4] J. Yoh,[4] M. Yokoyama,[16]
J. C. Yun,[4] F. Zetti[11]

[1] *Argonne National Laboratory, Argonne, Illinois 60439*

[2] *Brandeis University, Waltham, Massachusetts 02254*

[3] *University of Chicago, Chicago, Illinois 60637*

[4] *Fermi National Accelerator Laboratory, Batavia, Illinois 60510*

[5] *Laboratori Nazionali di Frascati,*
Istituto Nazionale di Fisica Nucleare, Frascati, Italy

[6] *Harvard University, Cambridge, Massachusetts 02138*

[7] *University of Illinois, Urbana, Illinois 61801*

[8] *National Laboratory for High Energy Physics (KEK), Tsukuba, Ibaraki 305, Japan*

[9] *Lawrence Berkeley Laboratory, Berkeley, California 94720*

[10] *University of Pennsylvania, Philadelphia, Pennsylvania 19104*

[11] *Istituto Nazionale di Fisica Nucleare,*
University and Scuola Normale Superiore of Pisa, I-56100 Pisa, Italy

[12] *Purdue University, West Lafayette, Indiana 47907*

[13] *Rockefeller University, New York, New York 10021*

[14] *Rutgers University, Piscataway, New Jersey 08854*

[15] *Texas A&M University, College Station, Texas 77843*

[16] *University of Tsukuba, Tsukuba, Ibaraki 305, Japan*

[17] *Tufts University, Medford, Massachusetts 02155*

[18] *University of Wisconsin, Madison, Wisconsin 53706*

[19] *Visitor*

VITA

Timothy Lee Hessing was born on September 30, 1963 in Clinton, Iowa. His parents are Leon Louis and Mary Ann Hessing. He graduated from Glenbard North High School in Carol Stream, Illinois in 1981 where he was recognized as an Illinois State Scholar and a member of the National Honor Society. He then attended Augustana College in Rock Island, Illinois, where he earned seven varsity letters while participating in football and wrestling. During this time he was a member of eight College Conference of Illinois and Wisconsin (CCIW) championship teams, including two NCAA Division III National Championship football teams. In his senior year, he earned All-American Honors in wrestling at heavyweight. At Augustana College he majored in Physics and Math/Computer Science, was inducted into both $\Sigma\Pi\Sigma$, the Physics honor society, and ΠME, the Math honor society. He graduated *cum laude* with an A.B. degree from Augustana College in 1985. His permanent mailing address is: 2N 562 Prairie Avenue, Glen Ellyn Countryside, Illinois 60137.